Search for Unparticles in Z and Missing Transverse Energy with the CMS Detector

MASTERARBEIT IN PHYSIK

von
KLAAS PADEKEN

im September 2012

vorgelegt der
Fakultät für Mathematik, Informatik und Naturwissenschaften
der Rheinisch-Westfälischen Technischen Hochschule Aachen

angefertigt im
III. Physikalischen Institut A
Prof. Dr. Thomas Hebbeker
Zweitgutachter
Prof. Dr. Christopher Wiebusch

Abstract

Many extensions of the Standard Model suggest a hidden valley at high energies. The model of Unparticles, which was proposed 2007 by H. Georgi [1], is one of them. The basic idea is a scale invariant sector, which at high energies couples directly to the Standard Model particles. The nature of this coupling must not be defined in detail, but one of the consequences of this scale invariant field would be particles with a continuous mass spectrum. Since normal particles have a defined mass pole this "stuff" would not be particles in the narrow sense of the word, therefore the name Unparticles was coined.
One of the advantages of the Unparticle model is that it is a formalism to describe all scale invariant high energy fields in a low energy limit. The result is always one new (Un)particle. The low energy limit in this context means energies accessible at the LHC. The most important parameters of this theory are the scaling dimension d_U and the effective energy cutoff parameter Λ_U. The requirement of scale invariance does not fix the spin of the Unparticle. Therefore scalar, bosonic and fermionic Unparticles are possible.
At the LHC with 7 TeV centre of mass energy Unparticles could be produced in association with Z bosons. The neutral Unparticle is assumed to be stable and would leave the detector. Therefore one of the observable signatures would be Z + $E_{\mathrm{T}}^{\mathrm{miss}}$.
The focus of this analysis is on scalar Unparticles in associated production with the Z. For this analysis only the muon decay channel of the Z is considered. To increase the signal an events with in the Z mass region are selected and the back-to-back kinematic for Unparticle and Z is used. The discriminating variable between the Drell-Yan and associated Unparticle production is $E_{\mathrm{T}}^{\mathrm{miss}}$. From the renaming Standard Model backgrounds the $t\bar{t}$ process is the the largest. This can be reduced by jet specific requirements by a factor of two.
In 5 fb^{-1} of the proton-proton data recorded by the CMS experiment in 2011 no sign of Unparticles could be detected. Therefore the excluded parameter region for scalar Unparticles was expanded. Unparticles are excluded for the scaling dimension of $d_U = 1$ to 1.95 for an effective energy scale of $\Lambda_U = 1$ TeV.

Zusammenfassung

Es gibt viele Erweiterungen des Standardmodells, die ein Hidden Valley bei hohen Energien vorhersagen. Ein Beispiel hierfür ist das von H. Georgi im Jahr 2007 [1] vorgeschlagene Modell des Unparticles. Die Idee hinter diesem Modell ist ein skaleninvarianter (conformaler) Sektor, in dem bei hohen Energien ein skaleninvariantes Feld mit dem Standardmodell wechselwirkt. Konsequenzen einer solchen Skaleninvarianz wären entweder massenlose Teilchen oder Teilchen, die eine kontinuierliche Massenverteilung haben. Da diese keine Teilchen im klassischen Sinne sind, wurde der Name Unparticle(s) geprägt.
Eine der bestechenden Eigenschaften des Unparticle Modells ist, dass nicht wie bei vielen anderen Erweiterungen des Standardmodells eine Vielzahl neuer Teilchen vorhergesagt wird. Statt dessen wird nur ein einziges Teilchen postuliert, dessen Eigenschaften zum größten Teil aus der Annahme der Skaleninvarianz hergeleitet werden können. Die Wechselwirkung zwischen diesem "Unparticle Stuff" und dem Standardmodell bei den am LHC zugänglichen Energien kann durch eine effektive Theorie beschrieben werden. Die wichtigsten Parameter dieser effektiven Beschreibung sind die Dimension der Skaleninvarianz d_U und die Energieskala Λ_U der effektiven Wechselwirkung. Da die Forderung nach Skaleninvarianz keine Einschränkung an die Spin-Konfiguration eines solchen Teilchens macht, sind bosonische und fermionische Unparticles denkbar.
Das am LHC bei 7 TeV Schwerpunktsenergie erzeugte Unparticle wird als sowohl stabil, als auch neutral angenommen und würde somit undetektiert bleiben. Einer der goldenen Kanäle um fehlende transversale Energie im Detektor nachzuweisen ist Z + $E_{\mathrm{T}}^{\mathrm{miss}}$.
Diese Analyse konzentriert sich auf die Suche nach einem skalaren Unparticle, welches zusammen mit einem Z-Boson erzeugt wird. Dabei konzentriert sich die Untersuchung auf den myonischen Zerfallskanal des Z-Bosons. Um ein klares Signal im Detektor zu erhalten und dieses von möglichen Untergrundereignissen abgrenzen zu können, werden Ereignisse mit zwei gut rekonstruierten Myonen selektiert, die eine invariante Masse in der Nähe der Z-Boson Resonanz haben. Die größere $E_{\mathrm{T}}^{\mathrm{miss}}$ wird als Diskriminator verwendet, damit das Signal von dem Z-Boson unterschieden werden kann. Der größte verbleibende Untergrund ist $t\bar{t}$, welches sich durch zusätzliche Jets und andere Kinematik vom Signal abhebt. Durch Schnitte auf diese Variablen kann das Verhältnis zwischen Signal und Untergrund deutlich angehoben werden.
Durch den Vergleich der Daten mit dem vorhergesagten Modell ist es möglich eine Aussage über die Signalparameter zu treffen. Es konnten keine Hinweise auf ein Unparticle in den 2011 von CMS aufgezeichneten 5 fb^{-1} Daten gefunden werden, daher können Ausschlussgrenzen angegeben werden. Für ein scalares Unparticle mit Λ_U = 1 TeV kann können Dimensionen von $d_U = 1$ bis 1.95 in einem 95% Confidence-Intervall ausgeschlossen werden.

Contents

1. Introduction

The Standard Model of particle physics has been tested and confirmed over the last decades. A intuitive question from people, who are not in the scientific community is: "Why do you keep searching, if you can describe nature so well?" This is a valid and good question. The need for a better and more precise model for particle physics is purely driven by the urge of humans to understand their environment. The goal of particle physics is the full description of the world at the smallest scale, which was achieved to high precision, but collapses if the small scale is transferred to large scales, such as the solar system or the universe, where general relativity is more accurate. The cosmological observations tell us that we can describe about 4% of the known matter in the universe with the Standard Model and there is no conclusive description that unifies gravity with the Standard Model of particle physics.
There have been various attempts to expand the particle physics understanding to physics beyond the Standard Model. These expansions all have in common that they predict new phenomena, solve some kind of problem or simplify an assumption within the Standard Model. While all these models have interesting and fundamental consequences to our perception of the world, the question is: Which one is right?
This question in essence comes back to "What are the fundamental principles in our world?" and is the corner stone of modern particle physics. To answer this the Large Hadron Collider (LHC) was built, which is the largest machine mankind has ever constructed. With energies up to seven times larger than the previous collider experiments physics beyond the Standard Model can be tested. The challenge for the experiments at the LHC is not to miss the one model that can perhaps explain the world. This boils the models down to the signature that they leave in the detector. All the fundamental answers that these models entail are irrelevant for the search.
One of these models is based on the idea of scale invariance and was proposed in 2007 by H. Georgi [1]. This model has several features that make it worth looking into. Scale invariance for example results in fractional scaling dimensions. The simple requirement of scale invariance fixes the phenomena at the LHC in much detail. There are several models that can include such a scale invariance, such as sting theory or super-symmetry. One of the features such a model would have, is that the field would have a continuous mass spectrum. This leads to the name for this scale invariant fields, which are called Unparticles.
Searching for Unparticles at the LHC helps to shape our understanding of the world. Or in the words of Antoine de Saint-Exupéry:
" 'What makes the desert beautiful,' said the little prince, 'is that somewhere it hides a well...' "

2. Theoretical Foundations

In the following the theoretical foundations for the Unparticle search are discussed. First a review of the Standard Model of particle physics is given, then the Unparticle model and related phenomena is discussed . Finally the used Unparticle model is specified.

2.1. The Standard Model of Particle Physics

The Standard Model of particle physics (SM) is a gauge theory, describing three out of four known forces in nature. It predicts the interactions of the electromagnetic, weak and strong forces to a high precision and it has withstood numerous experimental tests. The SM consists of fermion fields, interpreted as matter, and bosonic fields, interpreted as forces. The following summary is based on [2, 3] . The SM is based on the symmetry group $SU(3)_C \otimes SU(2)_L \otimes U(1)_Y$, which gives rise to several gauge fields. The groups can be associated to the observed forces. The strong interaction ($SU(3)_C$) has a colour charge and 8 massless spin 1 gluons. The electromagnetic force is mediated by the massless γ boson, while the weak interaction ($SU(2)_L$) can be associated to the massive uncharged Z^0 boson and the massive charged $W^{\pm}$ boson. The fermions can be divided into two groups, leptons and quarks, with tree generations each:

$$\begin{bmatrix} e & \mu & \tau \\ \nu_e & \nu_\mu & \nu_\tau \end{bmatrix} \qquad \begin{bmatrix} u & c & t \\ d & s & b \end{bmatrix}. \tag{2.1}$$

While quarks carry one of three colour charges and have an electric charge, electrons, muons and taus have an electric charge and neutrinos are electrically neutral. The three generations have different masses. Each fermion has a corresponding antiparticle. As will be explained in section 2.1.4 the weak interaction distinguishes between left- and right-handed fermion fields, where the handedness refers to the chiralities of the particle.

2.1.1. Lagrange-Formalism and Field Equation

A fundamental principle in physics is the Lagrange-Formalism, from which one can calculate all field properties. The Euler-Lagrange-Equation for fields is:

$$\partial_\mu \left(\frac{\partial \mathcal{L}}{\partial(\partial_\mu \phi)} \right) - \frac{\partial \mathcal{L}}{\partial \phi} = 0, \tag{2.2}$$

where $\mathcal{L}$ denotes the Lagrangian a ϕ is a scalar field. This leads to the Klein-Gordon equation for free massive spinless particles and the Dirac equation for spinors:

$$(m^2 + \partial_\mu \partial^\mu)\phi = 0, \quad (i\gamma_\mu \partial^\mu - m)\psi = 0. \tag{2.3}$$

The γ_μ is needed for the fermionic nature of the field and is constructed from the Dirac matrices, ψ denotes a spinor field. Both equations are generalisations of the Schrödinger equation.

Construction of QFTs

From the construction of the Lagrangian in equation 2.2 one can set various rules to construct a Lagrangian [4]:

- choose the fields the theory should contain
- ensure the invariance under symmetry transformations
- the Lagrangian has to contain ∂_μ terms (kinetic terms)
- the Lagrangian has to be renormalisable (the mass dimension has to be smaller than 4)
- all contributing terms have to be accounted for

2.1.2. Quantum Electrodynamics

To show that a theory without the previous constraints is not complete, one can look at the Lagrangian of a free Dirac fermion:

$$\mathcal{L}_0 = i\bar{\psi}(x)\gamma_\mu\partial^\mu\psi(x) - m\bar{\psi}(x)\psi(x). \tag{2.4}$$

This equation is not invariant under the $U(1)$ transformation $(e^{iQ\theta})$[1] and therefore can not be a complete description of the quantum electrodynamic (QED):

$$\psi(x) \xrightarrow{U(1)} \psi(x)' = e^{iQ\theta}\psi(x). \tag{2.5}$$

The kinetic terms show that if the phase θ is dependent on space-time $\theta = \theta(x)$, it transforms like:

$$\partial_\mu\psi(x) \xrightarrow{U(1)} e^{iQ\theta}(\partial_\mu + iQ\partial_\mu\theta)\psi(x). \tag{2.6}$$

The determination of the phase $\theta(x_0)$ at one point, would constrain $\theta(x)$ in all points. To avoid this one has to introduce a new spin-1 (photon) field $A_\mu(x)$, that transforms like:

$$A_\mu(x) \xrightarrow{U(1)} A'_\mu(x) = A_\mu(x) + \frac{1}{e}\partial_\mu\theta \tag{2.7}$$

and define a covariant derivative:

$$D_\mu\psi(x) = [\partial_\mu - ieQA_\mu(x)]\psi(x). \tag{2.8}$$

Therefore the full QED Lagrangian has to be:

$$\mathcal{L}_{QED} = i\bar{\psi}(x)\gamma^\mu D_\mu\psi(x) - m\bar{\psi}(x)\psi(x) - \frac{1}{4}F_{\mu\nu}(x)F^{\mu\nu}(x). \tag{2.9}$$

This Lagrangian is invariant under $U(1)$ transformations. The desired invariance introduced the necessity for a photon field A_μ. $F_{\mu\nu}$ is the field strength of the electromagnetic field, defined as $F_{\mu\nu} = \partial_\mu A_\nu - \partial_\nu A_\mu$. In principle one also has to add a mass term for $A_\mu(x)$, but as we know the photon mass is zero. The mass term for fermions is in principle not invariant under a local gauge transformation, this can be corrected by the spontaneous symmetry breaking, see section 2.1.5.

[1] $Q\theta(x)$ is a arbitrary factor which can be interpreted as charge and phase

2.1.3. Quantum Chromo Dynamics

For the strong interaction a similar approach as for QED can be used. First the Lagrangian for free particles must be constructed:

$$\mathcal{L}_0 = \sum_f \bar{q}_f^\alpha (i\gamma^\mu \partial_\mu - m_f) q_f^\alpha, \tag{2.10}$$

where q_f^α is a quark field with colour α and flavour f. The $SU(3)_C$ transforms in general like

$$q_f^\alpha \longrightarrow q'^\alpha_f = U^\alpha_\beta q_f^\beta, \quad UU^\dagger = U^\dagger U = 1. \tag{2.11}$$

The matrix U can be written in the general form

$$U = e^{i\frac{\lambda^a}{2}\theta_a}. \tag{2.12}$$

One of the main differences with respect to QED is that the $SU(3)_C$ generators do not commute. The generators $\frac{1}{2}\lambda^a$ are traceless and satisfy the commutation relation[2]

$$\left[\frac{\lambda^a}{2}, \frac{\lambda^b}{2}\right] = i f^{abc} \frac{\lambda^c}{2}. \tag{2.13}$$

In analogy to QED the covariant derivative can be constructed with a gauge field $G_a^\mu(x)$ as

$$D^\mu q_f = \left[\partial^\mu - i g_s \frac{\lambda^a}{2} G_a^\mu(x)\right] q_f. \tag{2.14}$$

This covariant derivative also determines the transformation properties of the gauge fields.

$$G^\mu \longrightarrow G'^\mu = U G^\mu U^\dagger - \frac{i}{g_s}(\partial^\mu U) U^\dagger. \tag{2.15}$$

This can be expanded under infinitesimal $SU(3)_C$ transformations from equation 2.12,

$$G_a^\mu \longrightarrow G_a'^\mu = G_a^\mu + \frac{1}{g_s}\partial^\mu(\delta\theta_a) - f^{abc}\delta\theta_b G_c^\mu, \tag{2.16}$$

$$q_f^\alpha \longrightarrow q'^\alpha_f = q_f^\alpha + i(\frac{\lambda^a}{2})_{\alpha\beta}\, \delta\theta_a q_f^\beta. \tag{2.17}$$

The corresponding gauge-invariant kinetic term needs to contain the derivatives of the gauge-fields. From the commutation relations the ansatz

$$G^{\mu\nu}(x) = \frac{\lambda^a}{2} G_a^{\mu\nu}(x) = \frac{i}{g_s}[D^\mu, D^\nu] = \partial^\mu G^\nu - \partial^\nu G^\mu - i g_s [G^\mu, G^\nu], \tag{2.18}$$

satisfies all required criteria. Therefore the full QCD Lagrangian can be written as

$$\mathcal{L}_{QCD} = -\frac{1}{4} G_a^{\mu\nu} G^a_{\mu\nu} + \sum_f \bar{q}_f (i\gamma^\mu D_\mu - m_f) q_f. \tag{2.19}$$

[2] The latin indices $a, b, c..$ denote different colour charges

2.1.4. Electroweak Unification

The weak interaction was first observed in β-decay, showing that left-handed (right-handed) fermion (antifermion) chiralities interact with the massive charged W boson. This was the beginning of the weak theory, which properties can be separated into the charged and the neutral currents. The weak theory can be unified with the QED, therefore four bosons have to be considered W^+, W^-, Z and γ.

Charged Currents

- coupling to left-handed fermions and right-handed anti-fermions
- $W^\pm$ decays into fermion doublets with a charge difference of $1e$
- the coupling strength is the same for all fermion doublets
- the flavour eigenstates of the d', c' and b' are mixtures of the mass eigenstates:

$$\begin{pmatrix} d' \\ c' \\ b' \end{pmatrix} = V_{CKM} \begin{pmatrix} d \\ c \\ b \end{pmatrix} \tag{2.20}$$

The matrix V_{CKM} denotes the flavour mixing, for details on this topic, see [5].
The neutral currents are mediated by Z and γ bosons

Neutral Currents

- Z and γ couplings are flavour conserving
- the coupling to fermions with the same electric charge has a universal strength. The Z boson couples to neutrinos, while γ does not
- the γ does not distinguish between left- and right-handed fermions, but Z couples differently to right- and left-handed fermions

The weak- and electromagnetic interactions can be unified into one interaction, which predicts the experimental facts mentioned above. The underlying group is $G = SU(2)_L \otimes U(1)_Y$. The spinors can be written as

$$\psi_1(x) = \begin{pmatrix} u \\ d \end{pmatrix}_L, \quad \psi_2(x) = u_R, \quad \psi_3(x) = d_R, \tag{2.21}$$

for the example of the first quark flavour. The free Lagrangian is then

$$\mathcal{L}_0 = i\bar{u}(x)\gamma^\mu \partial_\mu u(x) + i\bar{d}(x)\gamma^\mu \partial_\mu d(x) = \sum_{j=1}^{3} i\bar{\psi}_j(x)\gamma^\mu \partial_\mu \psi_j(x). \tag{2.22}$$

Different spinor parts then transform under G like

$$\psi_1(x) \longrightarrow \psi_1'(x) = e^{iy_1\beta} U_L \psi_1(x), \tag{2.23}$$
$$\psi_2(x) \longrightarrow \psi_2'(x) = e^{iy_2\beta} \psi_2(x), \tag{2.24}$$
$$\psi_3(x) \longrightarrow \psi_3'(x) = e^{iy_3\beta} \psi_3(x), \tag{2.25}$$

with $U_L = e^{i\frac{\sigma^i}{2}\alpha^i}$ and $Y = (y_1, y_2, y_3)$ is the electroweak hypercharge. As in QED the rules to construct a QFT require the covariant derivatives to be:

$$D_\mu \psi_1(x) = \left[\partial_\mu - ig\frac{\sigma_i}{2}W_\mu^i(x) - ig' y_1 B_\mu(x)\right]\psi_1(x), \tag{2.26}$$

$$D_\mu \psi_2(x) = \left[\partial_\mu - ig' y_2 B_\mu(x)\right]\psi_2(x), \tag{2.27}$$

$$D_\mu \psi_3(x) = \left[\partial_\mu - ig' y_3 B_\mu(x)\right]\psi_3(x). \tag{2.28}$$

The introduced fields B_μ and W_μ correspond to the correct number of gauge-bosons, have the coupling constants g and g' and would transform

$$B_\mu(x) \longrightarrow B'_\mu(x) = B_\mu(x) + \frac{1}{g'}\partial_\mu \beta(x), \tag{2.29}$$

$$\frac{\sigma_i}{2}W_\mu^i = \widetilde{W}_\mu \longrightarrow \widetilde{W}'_\mu(x) = U_L(x)\widetilde{W}_\mu U_L^\dagger(x) - \frac{i}{g}\partial_\mu U_L(x) U_L^\dagger(x) \tag{2.30}$$

The kinetic term of the Lagrangian therefore can be written as

$$\mathcal{L}_{kin} = -\frac{1}{4}B_{\mu\nu}B^{\mu\nu} - \frac{1}{4}W^i_{\mu\nu}W_i^{\mu\nu}, \tag{2.31}$$

with the definitions:

$$B_{\mu\nu} = \partial_\mu B_\nu - \partial_\nu B_\mu, \quad W^i_{\mu\nu} = \partial_\mu W^i_\nu - \partial_\nu W^i_\mu - ig[W_\mu, W_\nu]. \tag{2.32}$$

The interaction term of the Lagrangian is:

$$\mathcal{L}_{int} = g\bar{\psi}_1\gamma^\mu \widetilde{W}_\mu \psi_1 + g' B_\mu \sum_{j=1}^{3} y_j \bar{\psi}_j \gamma^\mu \psi. \tag{2.33}$$

In this Lagrangian one can separate the charged and neutral current interactions. While the charged current only interacts with a left-handed doublet ψ_1 the neutral current interacts with left- and right-handed spinors. The $\widetilde{W}_\mu$ can be written as:

$$\widetilde{W}_\mu = \frac{\sigma^i}{2}W^i_\mu = \frac{1}{\sqrt{2}}\begin{pmatrix} \sqrt{2}W^3_\mu & W^\dagger_\mu \\ W_\mu & -\sqrt{2}W^3_\mu \end{pmatrix} \tag{2.34}$$

The charged current is then mediated by $W_\mu = (W^1_\mu + iW^2_\mu)/\sqrt{2}$ and its complex-conjungate. The Fields W_μ and $W^\dagger_\mu$ therefore can be identified as W^- and W^+.
The neutral current contains the gauge fields W^3_μ and B_μ. Because of the chiral structure, these fields can mix with one another to the observable fields Z and γ. The fields A_μ and Z_μ are in general written as a rotation of these fields:

$$\begin{pmatrix} W^3_\mu \\ B_\mu \end{pmatrix} = \begin{pmatrix} \cos\theta_W & \sin\theta_W \\ -\sin\theta_W & \cos\theta_W \end{pmatrix}\begin{pmatrix} Z_\mu \\ A_\mu \end{pmatrix} \tag{2.35}$$

These relations restrain the complete electroweak theory, except the masses of the fermions and bosons. In principle mass terms could be added to the Lagrangian, but these terms would not be gauge-invariant, and therefore the theory would break down. This aspect can be addressed by the mechanism of the spontaneous symmetry breaking, see section 2.1.5.

2.1.5. Spontaneous Symmetry Breaking

Spontaneous symmetry breaking is a construct to introduce masses in the Lagrangian. The need for masses in the Standard Model is obvious for bosons such as $W^{\pm}$ or Z. One has to keep in mind that fermions are also massive. It is however not clear from the theoretical point of view that the same mechanism provides masses for bosons and fermions. The idea is that a scalar field with a symmetric potential can have a minimum which is not symmetric. Hence the symmetry is broken spontaneously.

The Goldstone Theorem

To show some of the properties of such a scalar field $\phi = 1/\sqrt{2}(\phi_1 + i\phi_2)$ with a potential $V(\phi) = \mu^2\phi^*\phi + \lambda(\phi^*\phi)^2$ is considered. The Lagrangian is:

$$\mathcal{L} = (\partial_\mu\phi)^*(\partial^\mu\phi) - \mu^2\phi^+\phi - \lambda(\phi^*\phi)^2 \tag{2.36}$$

and is invariant under a global $U(1)$ transformation. To show that this field can produce a massive boson the solution for the ground state can be chosen to be $\phi_1 = v$ and $\phi_2 = 0$. This can be transformed into any other solution with the $U(1)$ translation transformation. Small changes to the ground state can be written as:

$$\phi(x) = \frac{1}{\sqrt{2}}(v + \eta(x) + i\xi(x)), \tag{2.37}$$

which results in two particles if put into the Lagrangian:

- η with the mass $m_\eta = \sqrt{-2\mu^2}$
- ξ which is massless (Goldstone boson)

This is a general result and is known as the Goldstone theorem. In order to get the complete mechanism the local gauge invariance for $U(1)$ from equation 2.5 has to be used. This leads to the Lagrangian

$$\mathcal{L} = \frac{1}{2}(\partial_\mu\xi)^2 + \frac{1}{2}(\partial_\mu\eta)^2 - v^2\lambda\eta^2 - \frac{1}{2}e^2v^2A_\mu A_\mu - evA_\mu\partial^\mu\xi - \frac{1}{2}F_{\mu\nu}F^{\mu\nu} + \mathcal{L}_{int} \tag{2.38}$$

The ξ component of the potential can be removed by choosing the gauge to be $exp(i\frac{\xi}{v})$. This removes the massless Goldstone boson form the equation and the Lagrangian is:

$$\mathcal{L} = \frac{1}{2}(\partial_\mu\eta)^2 - v^2\lambda\eta^2 - \frac{1}{2}e^2v^2A_\mu A_\mu - \lambda v\eta^3 - \frac{1}{4}\lambda\eta + \frac{1}{2}e^2A_\mu A^\mu\eta^2 + \frac{1}{2}ve^2A_\mu A^\mu\eta - \frac{1}{2}F_{\mu\nu}F^{\mu\nu} \tag{2.39}$$

The only remaining mass terms are a massive gauge boson with $m_A = ev$ and a massive scalar boson, which can be interpreted as Higgs boson with $m_h = \sqrt{2\lambda v}$. To generate masses for three of four bosons in a $SU(2)_L \otimes U(1)_Y$ group the mechanism has to be modified.

The Higgs–Kibble Mechanism

For the $SU(2)$ the scalar field must have four degrees of freedom. The Lagrangian for such a field would consist of a kinematic term and a potential:

$$\mathcal{L} = (\partial_\mu \phi)^\dagger (\partial^\mu \phi) - \mu^2 \phi^\dagger \phi - \lambda (\phi^\dagger \phi)^2, \tag{2.40}$$

with the $SU(2)$-doublet constructed from scalar fields:

$$\phi = \frac{1}{\sqrt{2}} \begin{pmatrix} \phi_1 + i\phi_2 \\ \phi_3 + i\phi_4 \end{pmatrix}. \tag{2.41}$$

The Lagrangian must be invariant under the transformation 2.26 and the potential would have a solution for $\mu^2 < 0$ and $\lambda > 0$. The minimum is at:

$$\phi^\dagger \phi = \frac{1}{2}(\phi_1^2 + \phi_2^2 + \phi_3^2 + \phi_4^2) = \frac{\mu^2}{2\lambda}. \tag{2.42}$$

The additional part of the local gauge invariant Lagrangian is:

$$\mathcal{L} = |(i\partial_\mu - g\frac{\sigma_i}{2} W_\mu^i - g'\frac{Y}{2} B_\mu)\phi|^2 - V(\phi). \tag{2.43}$$

Therefore the ground state can be chosen to be:

$$\phi_1 = \phi_2 = \phi_4 = 0, \quad \phi_3 = \nu \quad \rightarrow \quad \phi_0 = \frac{1}{\sqrt{2}} \begin{pmatrix} 0 \\ \nu \end{pmatrix}. \tag{2.44}$$

The solution of the relevant term is therefore:

$$|(i\partial_\mu - g\frac{\sigma_i}{2} W_\mu^i - g'\frac{Y}{2} B_\mu)\phi|^2 = \frac{1}{8}\nu^2 g^2 [(W_\mu^1)^2 + (W_\mu^2)^2] + \frac{1}{8}\nu^2 (W_\mu^3, B\mu) \begin{pmatrix} g^2 & -gg' \\ -gg' & g'^2 \end{pmatrix} \begin{pmatrix} W^3\mu \\ B^\mu \end{pmatrix}. \tag{2.45}$$

As before $W^\pm$ can be identified as $W_\mu = (W_\mu^1 + iW_\mu^2)$ and the complex conjugated. Hence the mass of the W boson is $m_W = \frac{1}{2}\nu g$. For the masses of the neutral bosons the remaining part gives the solution $A_\mu = g' W_\mu^3 + g B_\mu$ for a massless photon and $Z_\mu = g' W_\mu^3 - g B_\mu$ for a Z boson with the mass $m_Z = \frac{1}{2}\nu\sqrt{g^2 + g'^2}$. From this mechanism the important prediction of the mass ratio can be made with the requirement of equation 2.34 and 2.35:

$$\sin^2 \theta_W = 1 - \frac{m_W^2}{m_Z^2} = 0.222. \tag{2.46}$$

The Higgs mass is a free parameter of the Standard Model and is still unknown, although recently an observation of a Higgs like particle with a mass near 125 GeV from ATLAS and CMS [6, 7] was made. The observation does not include a spin measurement, hence one can only confirm a new particle, with cross sections that are consistent with the Standard Model Higgs.
The coupling between fermions and a Higgs boson can be described with another mechanism. Recent results [8] suggest that a Higgs boson not coupling to fermions[3] is excluded with 99% confidence level in the mass range 110–134 GeV.

[3] A Higgs boson only coupling to bosons is often referred to as fermiophobic Higgs.

2.2. Conformal Fields

Conformal fields are quantum fields invariant under the conformal transformation. A conformal transformation conserves angles between curves and the shapes of infinitesimally small coordinates. A scale invariant QFT need not necessary be conformal invariant, but non conformal Unparticles would lead to different phenomena as discussed in [9]. Most of the scale invariant models however are conformal invariant and have been studied in various examples [10]. Therefore Conformal Field Theory (CFT) provides an ideal environment to study scale invariant theories. The conformal group [11] is a subgroup of coordinate transformations that leave the metric invariant up to a scale transformation:

$$g_{\mu\nu}(x) \to g'_{\mu\nu}(x') \equiv \Omega(x) g_{\mu\nu}(x). \tag{2.47}$$

It may be noted here, that the Poincaré group is a subgroup of the conformal group ($g_{\mu\nu} = g'_{\mu\nu}$). One can express the coordinate transformation as an infinitesimal coordinate shift $x^\mu \to x^\mu + \epsilon^\mu(x)$. The shift $\epsilon^\mu(x)$ is fixed by a differential equation that is a consequence from equation 2.47:

$$\frac{2}{d}(1-d)\partial^2\partial_\rho\epsilon^\rho = 0 \tag{2.48}$$

For the full calculation see appendix A.1. This differential equation has several solutions. First of all the Poincaré group is reproduced ($\Omega = 1$):

$$x \to x' = x + a, \tag{2.49}$$

$$x \to x' = \Lambda x \qquad \text{with } (\Lambda^\mu_\nu \in SO_d) \tag{2.50}$$

and the scale invariant transformations:

$$x \to x' = sx \qquad (\Omega = s^{-2}), \tag{2.51}$$

$$x \to x' = \frac{x + bx^2}{1 + 2b\cdot x + b^2x^2} \quad (\Omega(x) = (1 + 2b\cdot x + b^2x^2)^2). \tag{2.52}$$

Hence the main feature of Unparticles is the scale invariance, equation 2.51 is central. A scale invariant field of the dimension d would transform under a transformation $x \to x' = sx$ as

$$O_U(x) \to O'_U(x') = s^{-d} O_U(x). \tag{2.53}$$

2.3. Hidden Sector and Effective Theory: Constructing Unparticles

The idea of Unparticles [1, 12, 13, 14] (for illustration, see Figure 2.1) is that in a hidden sector at high energies a scale invariant field, here called Banks-Zaks fields (BZ), interacts with the Standard Model through the exchange of particles with a large mass M_U. Below the energy of M_U the interaction is suppressed by powers of M_U and can be described by field operators

$$\mathcal{L} = \mathcal{L}_{SM} + \mathcal{L}_{BZ} + \mathcal{L}_{int} \tag{2.54}$$

$$\mathcal{L}^{eff}_{int} = \frac{1}{{M_U}^{d_{SM}+d_{BZ}-4}} O_{SM} O_{BZ}, \tag{2.55}$$

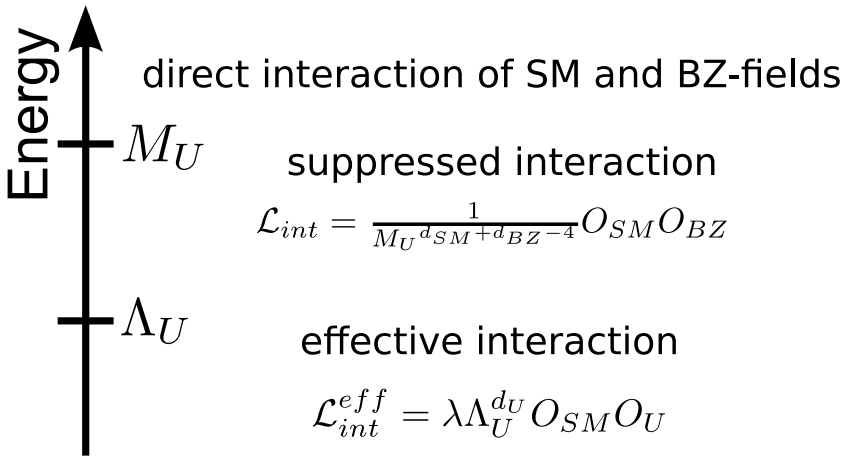

Figure 2.1.: The energy scheme as proposed by H. Georgi [1].

where d_{BZ} is the scaling dimension of the Banks-Zaks field. At an energy scale of Λ_U the renormalisation coupling to the scale invariant field induces dimensional transmutation and the interaction can be described as an effective Lagrangian:

$$\mathcal{L}_{int}^{U} = \frac{C_U \Lambda_U^{d_{BZ}-d_U}}{M_U^{d_{SM}+d_{BZ}-4}} O_{SM} O_U \tag{2.56}$$

where C_U is a normalisation constant. The Banks-Zaks field operator can be rewritten as Unparticle operator with the scaling dimension d_U. One can see that $\lambda = \frac{C_U \Lambda^{BZ}}{M_U^{d_{SM}+d_{BZ}-4}}$ is a measure for the coupling between Unparticles and the Standard Model. One of the consequences of the scale invariance is a continuous mass spectrum of the Unparticles. From this the name is inspired, since a particle has usual a fixed mass peak. The broadness of the mass distribution changes with different values of d_U.

2.3.1. Unparticle Spin

The spin of Unparticles is a priori not defined. All known configurations of scalar, fermion, vector or tensor Unparticles are thinkable. From the general construction of CFTs each spin has a lower bound on the scaling dimension d_U from unitarity [15]. The bound on d_U can be found in Table 2.1.

A dimension of $d_U > 2$ is in principle ultraviolet sensitive. This constraint links the energy scale Λ_U to the dimension above 2, but in general an ultraviolet sensitive effective theory is not problematic, because it is only valid up to an energy Λ_U. In order to avoid a unmotivated finetuning only $d_U < 2$ is considered in this analysis.

In the following we will concentrate on a scalar Unparticle, because for a scalar the dimensional constraint is the weakest and therefore the largest Unparticle parameter space is accessible. For spin 1 Unparticles the cross sections for $d_U > 3$ are too small to be detectable with a 7 TeV hadron collider. For an example value of $\Lambda_U = 1\,\text{TeV}$ different cross section values are plotted in Figure 2.3. The cross section excludable with the LHC and $5\,\text{fb}^{-1}$ for Unparticles is about 50 fb. Unparticles with spin 2 are have an even smaller cross section. A

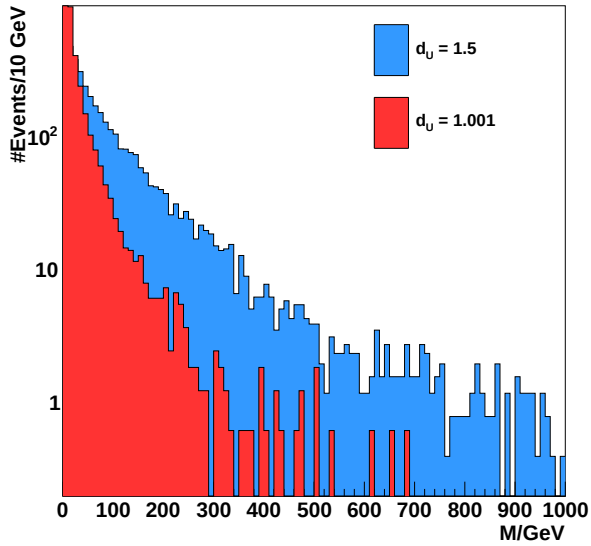

Figure 2.2.: The scalar Unparticle mass distribution for $\Lambda_U = 1\,\text{TeV}$. In contrast to Standard Model particles, Unparticles have a continuous mass spectrum.

spin	min d_U	max σ ($\Lambda = 1\,\text{TeV}$) [pb]
0	1	96.9
1/2	3/2	1.8
1	3	$9.2{\cdot}10^{-4}$
2	4	$6.7{\cdot}10^{-9}$

Table 2.1.: *Minimal values of d_U as a result of the conformal invariance. And the maximal cross section for $\Lambda_U = 1\,\text{TeV}$*

fermionic Unparticle would only have a bound of $d_U > 3/2$ and has the most potential for future analysis in the search channel presented here.

2.3.2. Feynman Rules for Unparticles

In order to derivative a matrix element and calculate cross sections some properties of the Unparticle model have to be derived. The scale invariant nature leads to some results deviating from the usual field theory. A more detailed calculation can be found in [16].

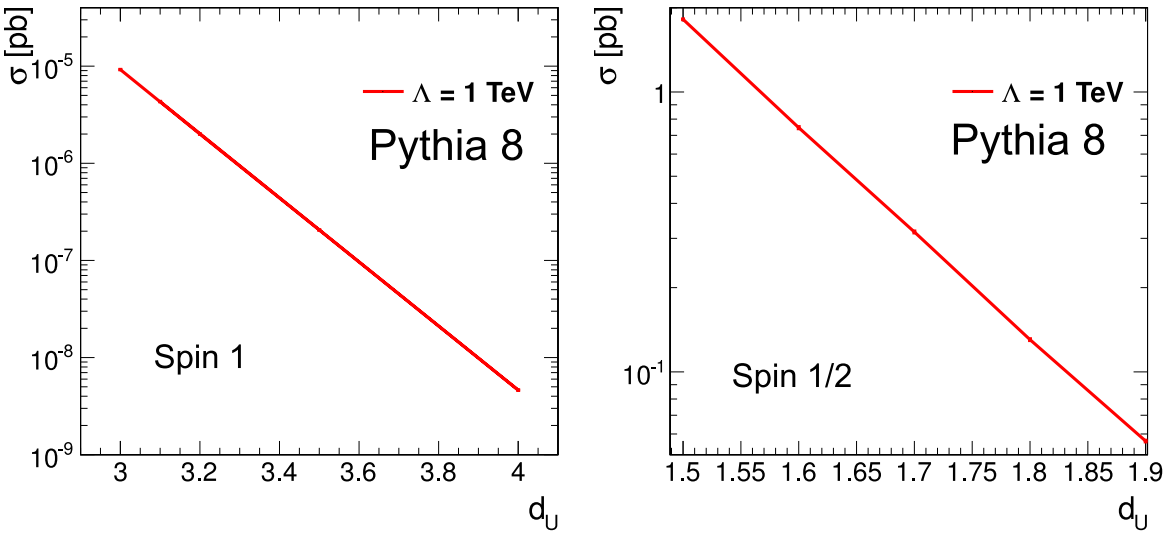

Figure 2.3.: The cross section for a $\Lambda_U = 1\,\text{TeV}$ spin 1 Unparticle is about four orders of magnitude smaller than the accessible cross section at a 7 TeV LHC in this channel. The spin $\frac{1}{2}$ Unparticles would have discovery potential at the LHC.

Phase Space

For a scalar Unparticle one can calculate the phase space normalisation from the two point function of the operator O_U [16]:

$$\begin{aligned} <0|O_U(x)O_U^\dagger(0)|0> &= <0|e^{iP_U\cdot x}O_U(0)e^{-iP_U\cdot x}O_U^\dagger(0)|0> \\ &= \int d\lambda \int d\lambda' <0|O_U(0)|\lambda'><\lambda'|e^{-iP_U\cdot x}|\lambda><\lambda|O_U^\dagger(0)|0> \\ &= \int \frac{d^4P_U}{(2\pi)^4}e^{ip\cdot x}\rho_U(P_U^2); \qquad (2.57) \\ \rho_U(P_U^2) &= A_{d_U}\theta(P_U^0)\theta(P_U^2)(P_U^2)^{d_U-2}. \qquad (2.58) \end{aligned}$$

where $\rho_U(P_U^2)$ is the spectral density, P_U^2 is the invariant mass squared of the Unparticle, A_{d_U} is the normalisation in d_U dimensions and $\theta(P_U^0), \theta(P_U^2)$ ensure a positive energy and Unparticle mass[4]. A_{d_U} is given by convention as the limit of $n = d_U$ massless particles:

$$A_{d_U} = \frac{16\pi^{5/2}}{(2\pi)^{2d_U}}\frac{\Gamma(d_U+\frac{1}{2})}{\Gamma(d_U-1)\Gamma(2d_U)}. \qquad (2.59)$$

Here one can see that an Unparticle would look like the d_U massless particles, but because d_U denotes the scaling dimension it is not constrained to an integer value. Something like fractional particles can be described by the Unparticle model. The production of an Unparticle

[4] $\theta(x)$ here denotes the Heaviside-function defined as $\theta(x) = 1$ for $x \geq 0$ and $\theta(x) = 0$ for $x < 0$.

plus n massless particles can therefore generally be written as:

$$d\sigma(p_1, p_2 \to P_U, k_1, k_2, ..., k_n) = \frac{1}{2s}|\overline{M}|^2 d\Phi \tag{2.60}$$

$$\text{where} \qquad d\Phi = (2\pi)^4 \delta^{(4)}(p_1 + p_2 - P_U - k_1 - k2 - ...) \prod_i \left[2\pi\theta(k_i^0)\delta(k_i^2) \frac{d^4 k_i}{(2\pi)^4} \right]$$

$$\cdot A_{d_U} \theta(P_U^0)\theta(P_U^2)(P_U^2)^{d_U - 2} \frac{d^4 {P_U}^4}{(2\pi)} \tag{2.61}$$

and $|\overline{M}|^2$ is the colour- and spin-averaged matrix element squared.

Unparticle Propagator

To define an Unparticle Feynman propagator $\Delta(P_U^2)$ one uses the general formalism as can be found for example in [4]

$$\Delta(P_U^2) = \frac{1}{2\pi} \int_0^\infty \frac{\rho_U(M^2) dM^2}{P_U^2 - M^2 + i\epsilon}. \tag{2.62}$$

The function $\rho_U(M^2)$ as defined in equation 2.58 ensures the normalisation in d_U dimensions. Because of the scale invariance the propagator can be written as

$$\Delta(P_U^2) = Z_{d_U}(-P_U^2)^{d_u - 2}. \tag{2.63}$$

The factor Z_{d_U} can be obtained comparing the imaginary part of equation 2.62 with equation 2.63 to be $Z_{d_U} = A_{d_U}/(2\sin(d_U\pi))$ and therefore is

$$\Delta(P_U^2) = \frac{A_{d_U}}{2\sin(d_U\pi)}(-P_U^2)^{d_U - 2} \tag{2.64}$$

For non-scalar Unparticles additional spin structures have to be considered, for details see [16].

Unparticle Vertices

From equation 2.56 one can construct different vertices for the interaction between Unparticles and the Standard Model. Four diagrams are allowed in general to couple fermions to scalar Unparticles:

$$\lambda \frac{1}{\Lambda_U^{d_U - 1}} \bar{f} f O_U, \quad \lambda \frac{1}{\Lambda_U^{d_U - 1}} \bar{f} i\gamma^5 f O_U, \quad \lambda \frac{1}{\Lambda_U^{d_U - 1}} \bar{f} \gamma^\mu f (\partial_\mu O_U), \quad \lambda \frac{1}{\Lambda_U^{d_U - 1}} \bar{f} \gamma^\mu \gamma_5 f (\partial_\mu O_U). \tag{2.65}$$

A vertex for a Unparticle - gauge interaction would look like

$$\lambda \frac{1}{\Lambda_U^{d_U - 1}} G_{\alpha\beta} G^{\alpha\beta} O_U, \tag{2.66}$$

where $G_{\alpha\beta}$ denotes a general gauge field. Note that λ can have different values for all processes. It is possible to allow flavour changing or lepton number violating vertices.

2.4. Model Assumptions

There are several constrains on the model from theoretical assumptions. For a more detailed overview, see Section 2.5. It is possible to construct various interesting Unparticle processes that can be accessed by the LHC. For this analysis scalar Unparticles have the biggest discovery potential. As the Feynman diagrams in Figure 2.4 for the considered channel show, the Unparticle can couple to different Standard Model particles. The coupling strength is in principle a free parameter and could be different for every Standard Model particle. In order to keep the model simple with a high predictive power, several assumptions have to be made. Firstly a universal coupling strength λ is assumed, meaning that all SM fields couple equally to the Unparticle. Because of the hard experimental constraints on flavour changing or lepton number violating vertices such processes are not considered. As motivated in Section 2.3.1 the scale dimension is constrained to $1 < d_U < 2$ in order to avoid non valid model parameters. The Unparticle is assumed to leave the detector undetected. This can either be due to the fact that the Unparticle is stable or long-lived, or the Unparticle itself decays to a hidden sector. Another constraint would arise for the massless limit of the Unparticle model ($d_U \to 1$). A high coupling constant with massless particles could mean the exchange of Unparticles within the atomic nuclei or a fourth type of radioactive decay [17], both of which are not observed in nature. This could be prevented by either a mass gap, a small coupling constant λ or a larger scaling dimension d_U.

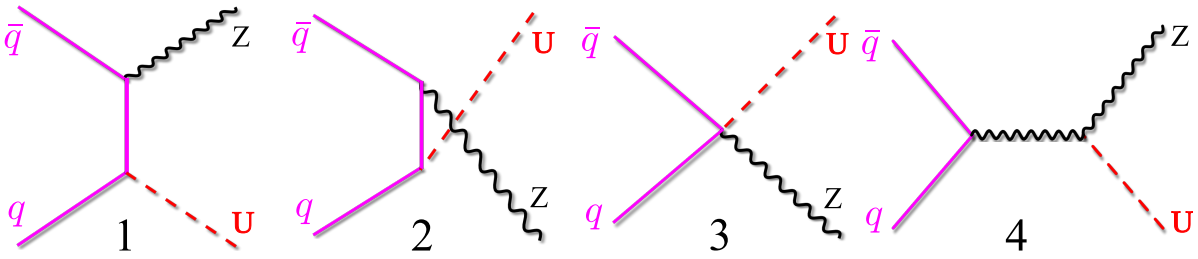

Figure 2.4.: The Feynman diagrams for the $Z + U$ final state in leading order.

2.4.1. Matrix Element

As experimental search channel the associated Z+U production is chosen with the Z decaying to muons. The contributing Feynman diagrams can be seen in Figure 2.4. The cross section has been calculated. The general differential cross section for an Unparticle is [18]:

$$\frac{d^2\sigma}{dP_U^2 dt} = \frac{|\bar{M}|^2}{16\pi s^2} \frac{A_{d_U}|\lambda|^2}{2\pi\Lambda_U^2} \left(\frac{P_U^2}{\Lambda_U^2}\right)^{d_U-2}, \tag{2.67}$$

The usual definitions for the Mandelstam variables s, t and u are used. The process specific part is in the Matrix element:

$$|\bar{M}|^2 = \frac{1}{4N_C} \left(\frac{e^2}{\sin^2\theta_W \cos^2\theta_W}\right) (g_{L,q}^2 + g_{R,q}^2)|A|^2, \tag{2.68}$$

with the electroweak specific factors $g^2_{L,q}$ and $g^2_{R,q}$ due to the Z coupling. The kinematic variables are collected in $|A|^2$

$$\begin{aligned}|A|^2 =& 4[-\frac{s}{t} - (1-\frac{m_Z^2}{t})(1-\frac{P_U^2}{t}) \\ & - \frac{s}{u} - (1-\frac{m^2}{u})(1-\frac{P_U^2}{u}) + 2(1-\frac{P_U^2}{t})(1-\frac{P_U^2}{u})].\end{aligned} \tag{2.69}$$

The invariant mass of the Unparticle P_U^2 must be constrained to

$$0 \leq P_U^2 \leq (\sqrt{s} - m_Z)^2. \tag{2.70}$$

2.5. Comments on the Unparticle Model

There have been several comments on and extensions of the Unparticle model. One of the most common extension is the existence of a mass gap [19][20]. Various studies were performed investigating Unparticle self interactions [14] and flavour changing neutral currents with Unparticle couplings[21]. The cosmological consequences of Unparticles are investigated in [22], but there are some problems within the cosmological model which were discussed in [23]. The possibility of Unparticles coupling to the Higgs boson or Unparticles as Higgs boson were also discussed in [24] and [25]. Some more exotic extensions were also studied, e.g. scale invariant fields which are not in the conformal group [9] or coloured Unparticles [26] [27].
This summary is intended to give a short overview of possible Unparticle phenomena.

2.5.1. Unparticle Mass Gap

A mass gap of the order of GeV, requiring a minimal mass of the Unparticle, would have considerable impact on the cosmological interpretation of the Unparticle model and the low energy behaviour. A mass gap would break the conformal symmetry at low energies and therefore new phenomena would only be accessible at higher energies. For the cosmological interpretation the most obvious consequence would be the disappearance of long range forces. At the LHC however a small mass gap has no considerable impact. This is studied in some more detail in chapter 6.3. The introduction of a mass gap can have several causes, e.g. a coupling of the Unparticle to the Higgs. The introduction of a mass gap also allows interesting phenomena with Unparticle decays[20]. If the mass gap is at higher energies one can also consider Unparticle resonances [28].

2.5.2. Unparticle Self-Interactions

Interesting phenomena would arise, if the Unparticle would have a self-interaction, so that final states with multiple particles in the final state are enhanced [29]. The processes would involve the three point function $U \rightarrow UU$ and require the Unparticle to decay. But as was pointed out in [30], from the conformal field structure upper bounds on the cross section can be obtained, which show that the processes with multiple final particles have a small cross section and it would be unlikely to find these at the LHC.

2.5.3. Unparticle Higgs interaction

An interesting coupling for Unparticles is the Unparticle-Higgs coupling. The Higgs boson is still an unknown quantity in the Standard Model, though there are strong indications, see section 2.1.5. A strong coupling between Unparticle and Higgs could change the properties of the Higgs such as mass and width [31]. There still would be an observable Higgs mass resonance, but with non Standard Model properties.
Other models proposed the Unparticle as Higgs boson or Unhiggs [24]. The idea is that a scalar Unparticle could fulfil all indirect indications pointing to the existence of a Higgs boson. Recent interpretations of the 2011 data from CMS and ATLAS [25] have shown that the Unhiggs hypothesis is not constrained very much for $m_h > 200\,\text{GeV}$, but no conclusive statement for $m_h < 200\,\text{GeV}$ could be made.

2.5.4. Neutral Currents with Unparticles

Unparticles that couple to fermions can induce flavour changing neutral currents [21]. In fact it is argued in [30] that there is no theoretical argument for the Unparticle not to be flavour blind. From previous measurements we know that such FCNC have not been observed in nature. The usual way to avoid these FCNC is, to require that the coupling strength is very small, but there are at least two other possible solutions. Firstly Unparticles could only couple to bosons and therefore have no FCNC, or secondly with the assumption of a mass gap the results from low energy experiments can be blind to FCNC at higher energies. A detailed study of FCNC with Unparticles can be found in e.g. [32]. In thins analysis no flavour violation is assumed.

2.6. Bounds on Unparticle Models

There have been several studies of Unparticles in the recent years. The influence of spin 1 Unparticles on the electric and magnetic dipole moments [33] give hard constraints. There also have been studies of Kaon mixing [34] with Unparticles. Direct searches include monojets at CMS [35][5]. The limits are summarized in Table 2.2. Older reinterpretations of extra dimension searches at CDF used the same channel, but had lower bounds on Λ_U , with lower limits between $\Lambda_U = 18.9\,\text{TeV}$ for $d_U = 1.35$ and $\Lambda_U = 1\,\text{TeV}$ for $d_U = 1.7$ [30]. There were also reinterpretations of LEP measurements [36]. Unparticles could be excluded in ranges from $\Lambda_U = 69.5\,\text{TeV}$ for $d_U = 1$ and $\Lambda_U = 0.5\,\text{TeV}$ for $d_U = 2$ by assuming a Z-U coupling. If assuming a $\gamma - U$ coupling the excluded parameter range is from $\Lambda_U = 25\,\text{TeV}$ for $d_U = 1$ to $\Lambda_U = 0.2\,\text{TeV}$ for $d_U = 2$.

[5]The monojet Unparticle production is in the channel $gg/q\bar{q} \to q/g + U$.

d_U	Λ_U exp. [TeV]	Λ_U obs. [TeV]
1.35	13.4	18.9
1.40	6.43	8.07
1.45	3.75	4.57
1.50	2.38	2.90
1.60	1.46	1.62
1.70	1.00	1.07

Table 2.2.: *Lower bounds from mono-jet searches at CMS [35] with 95$CL*

d_U	1.	1.01	1.05	1.1	1.2	1.3	1.4	1.5	1.6	1.7	1.8	1.9	2.00
Λ_U(Z) [TeV]	69.5	59.0	40.7	26.6	12.7	6.8	4.0	2.5	1.6	1.1	0.80	0.60	0.46
$\Lambda_U(\gamma)$ [TeV]	25.2	23.0	13.2	8.0	3.6	2.0	1.2	0.79	0.57	0.41	0.30	0.24	0.19

Table 2.3.: *Lower bounds from reinterpretations of LEP bounds on electroweak bosons plus* $E_{\mathrm{T}}^{\mathrm{miss}}$ *searches [36] with 95% CL.*

3. Experimental Setup

This chapter gives an overview of the experiment used to collect the analysed data. First there will be a short overview of the relevant physics principles involved in collider physics and the LHC, then a description of the CMS detector follows.

3.1. Collider Physics

The majority of new discoveries in particle physics require a high centre-of-mass energy $\sqrt{s}$ to produce new physics directly. In the last decades many machines were built to achieve this goal. So far most of the steps towards higher energy have brought new discoveries. The idea is that most physics processes have a mass resonance and therefore a cross section enhancement at an energy $\sqrt{s} \approx M$ and they would not be produced at an energy $\sqrt{s} \ll M$ with high rates. Using particle colliders instead of fixed target experiments is a consequence of the relativistic kinematics with $v \approx c$. The main argument for a circular collider are the acceleration possibilities.
Every collider accelerates particles in $\vec{E}$-fields (cavity resonators). In a linear accelerator every acceleration point is passed only once by every particle. A circular structure, where the particles are bent in a ring by $\vec{B}$-fields, allows the same particle to be accelerated multiple times by the same clystron. Fundamental pointlike particles, e.g. electrons would be desirable particles for such a collider, because of the clean experimental environment of the resulting events. Unfortunately the energy loss due to synchrotron radiation is proportional to $E^4/(m^4 R)$ and has set so far the technical limitations to the centre of mas energy of electron accelerators at about 200 GeV. This is the maximum $\sqrt{s}$ the LEP collider achieved.
A possible solution for this problem is the use of heavier particles, however the muon as natural choice has a too short lifetime and possible muon production mechanisms can not achieve a sufficient rate for a high luminosity collider. Because of this non fundamental particles like protons are used in the Tevatron ($\sqrt{s} = 1.96\,\text{TeV}$ for $p\bar{p}$ in Run II) and LHC. The disadvantage is that the initial state of the interaction is not known event by event. Every parton p carries only a fraction x of the proton energy. The resulting centre-of-mass energy can therefore be written as

$$\sqrt{s'} = \sqrt{s x_1 x_2}. \tag{3.1}$$

The kinematic distribution within the parton can be described by the parton density functions (PDF) and is an important input for the understanding of hadron collider physics [37]. The cross section of every process P can be factorised with the PDF

$$\sigma(pp \to X_P) \propto \sum_i \sum_J C_{ij}^P(x_1, x_2, \alpha_s(Q^2)) \otimes f_i(x_1, Q^2) \otimes f_j(x_2, Q^2), \tag{3.2}$$

where $C_{ij}^P(x_1, x_2, \alpha_s(Q^2))$ describes the hard process for the parton types i and j at an energy Q with the coupling constant $\alpha_s(Q^2)$. This is for the most processes calculable in power series

of $\alpha_s(Q^2)$. But the PDF $f_i(x, Q^2)$ is only experiential accessible. As a consequence of PDF the number of events with a high $\sqrt{s'}$ is reduced. The centre of mass energy of the interaction $\sqrt{s'}$ is always below the centre of mass energy of the proton proton system. Therefore a high luminosity machine is needed to produce enough events with high $\sqrt{s'}$.

3.2. The Large Hadron Collider

The LHC [38] is designed to deliver an instantaneous luminosity of $\mathcal{L} = 10^{34}\,\mathrm{cm}^2 s$ at a $\sqrt{s}$ of 14 TeV in a 27 km long ring, which is needed to produce a sufficient number of new physics events. The number of events per second is described by equation 3.3

$$N = \mathcal{L} \times \sigma. \tag{3.3}$$

The machine luminosity per interaction depends only on the beam parameters which can be written as:

$$\mathcal{L} = \frac{N_b^2 n_b f_{rev} \gamma_r}{4\pi \varepsilon_n \beta^*} F. \tag{3.4}$$

The main parameters are the number of particles per bunch n_b, the number of bunches N_b, the revolution frequency f_{rev}, the relativistic gamma factor γ_r, ε_n the normalised transverse beam emittance and β^* the beta function at the collision point. $F = (1 + (\frac{\theta_c \sigma_Z}{2\sigma^*})^2)^{-1/2}$ is the geometric luminosity reduction factor due to the small crossing angle θ_c at the interaction point with the transverse RMS σ^*.
There are several ways to gain high luminosity within the given parameters, which have different consequences for the experiments. Five of the seven parameters can be tuned within the machine boundaries, but most are highly correlated and are under constant optimisation. The β^* is a measure for the longitudinal focus of the beams. The number of bunches per beam is among other things limited by nonlinear beam-beam interactions. The number of events per bunch is limited by the Coulomb repulsion between the protons and therefore the mechanical aperture of the focusing magnets. Other limitations are the heat deposited in the cryogenic system and the maximum dipole field in the superconducting magnets. Where the nominal design is 2808 bunches per beam with 25 ns bunch spacing, a $\beta^* = 0.55m$, a normalised transverse emittance $\varepsilon_n = 3.75\mu m$ and 1.15×10^{11} protons per bunch, the operation in 2010 and 2011 was at a lower $\sqrt{s} = 7$ TeV and a higher bunch spacing of 50 ns. The lowest β^* was 1 m with $\varepsilon_n = 2.4\,\mu$m, a maximum of $1.43 \cdot 10^{11}$ protons per bunch and bunches per beam [39].
There are four big experiments at the LHC: ALICE, ATLAS, CMS and LHCb. The multi purpose experiments ATLAS and CMS are designed to record all interesting Standard Model processes and potential new physics. The b-physics experiment LHCb is focused on flavour physics and the heavy ion experiment ALICE is specialised in the lead-lead runs of the LHC at a $\sqrt{s_{NN}} = 2.76$ TeV. The high luminosity experiments ATLAS and CMS both recorded about 6 fb^{-1} in 2011. For analysis purposes 5 fb^{-1} were certified.

3.3. The CMS Detector

The Compact Muon Solenoid (CMS) detector [40] is located 100 m underground at the interaction point (IP) 5 on the French side of the LHC. The detector as seen in Figure 3.1 is 16 m

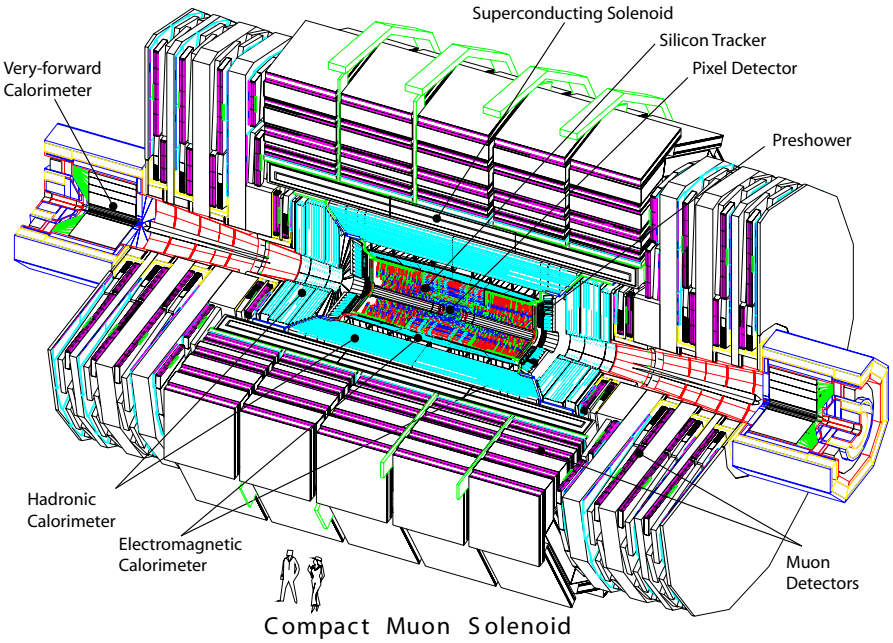

Figure 3.1.: The CMS Detector [40]

long and has a 14.6 m diameter. As a general purpose detector a 4π coverage has been tried to achieve. The aims of the CMS design was a detector that can find and measure potential new physics and measure the Standard Model at high energies. Four areas requirements can be singled out:

- muon p_T resolution up to high energies
- charged particle resolution and particle identification
- photon resolution and isolation
- $E_{\mathrm{T}}^{\mathrm{miss}}$ and dijet resolution

On top of this the LHC design parameters [41] plan 25 ns bunch spacing and a mean of up to 20-30 non elastic interactions per bunch crossing [1]. Therefore the detector response and readout are very time sensitive and the reconstruction has to be able to separate the potential interesting interactions form the pile up interactions, see Section 6.7.
One of the key components for a good charged particle resolution is a powerful magnet. The CMS magnet is a 4 T solenoid[2] that encloses the entire silicon-tracker, the electromagnetic calorimeter (ECAL) and the inner hadron calorimeter in the barrel region. Outside the solenoid are the outer hadron calorimeter and the muon systems embedded into an ion yoke to return the magnetic field. In the forward region a higher activity especially from hadronic objects is observed. Therefore the instrumentation is different from the barrel region.

[1] For a 50 ns scenario the number of protons per bunch can be much higher, resulting in a mean of 40-80 non elastic interactions per bunch crossing.
[2] In practice the field strength is 3.8 T.

3.3.1. Coordinate System and Detector Quantities

The CMS coordinate system is oriented along the LHC beam axis. The nominal interaction point is set to be the origin of the coordinate system. The the z-axis points along the beam towards the Jura mountains from IP5 or in the mathematical positive direction with respect to the LHC ring viewed from the surface. The x-axis points to the centre of the LHC ring and the y-axis points vertically upwards. For the reconstruction of particles in the detector often a modified spherical coordinate system is used. Where r measures the distance from the origin and ϕ is the angle in the $x-y$-plane the angle θ in the $y-z$-plane is substituted by the pseudo rapidity η, which can be transformed into θ by:

$$\eta = -\ln[\tan\frac{\theta}{2}]. \tag{3.5}$$

The pseudo rapidity has the advantage that in the ultra-relativistic limit (masses are negligible) the difference between two particles is invariant under a Lorentz boost in the z-direction. This is an important feature because of the unknown longitudinal z-momentum of the initial partons. Therefore the whole process can be boosted along the z-axis.
It is important to define a measure of distance between two particles, that is Lorentz invariant in the z-direction. For isolation and particle distances the ΔR variable is commonly used, which is defined as

$$\Delta R = \sqrt{(\Delta\eta)^2 + (\Delta\phi)^2}. \tag{3.6}$$

In contrast to the initial longitudinal momentum components the initial transverse momentum is known, due to the negligible transverse momentum of the initial partons. Therefore at a hadron collider the parameters of interest are the transverse quantities like p_T, E_T and $E_{\mathrm{T}}^{\mathrm{miss}}$.

3.4. The Inner Tracker

Goal of the tracking system is a measurement of charged particles p_T down to 1 GeV in a range up to $|\eta| < 2.5$. The expected particle density is $1Hz/\,\mathrm{mm}^2$ in 4 cm distance. These requirements have two consequences for the inner tracking system. A fine granularity is needed, as well as radiation hard detectors. This stands in contrast to the need for a low material budget to avoid multiple scattering, Bremsstrahlung, photon conversion and nuclear interactions. The entire inner tracking system is based on silicon sensors, that provide about 200 m^2 of active area, which is the largest silicon tracker ever built. For an exact p_T measurement and vertex reconstruction, which is important for b-tagging and pile up suppression, the inner layers are the crucial parts of the detector. Therefore the tracker is divided into two parts, the inner pixel detector with a radius of 4.4 cm to 10.2 cm and the strip tracker that extends to a radius of 1.2 m. The radiation damage can be countered with a cooling system that exploits the strong dependence of the leakage current on temperature. The goal is a temperature of -10°C. This requires the C_6F_{16} cooling fluid with a temperature down to -30°C and imposes an additional stress factor on the used elements. Where the strip detector is designed to have a lifetime of about 10 years at the nominal design luminosity, the pixel detector is planned to be exchanged in 2016.

3.4.1. Pixel Detector

The pixel detector consists of three 53.3 cm long cylindrical layers at $r = 4.4$, 7.3 and 10.2 cm and two disk modules at each side at $|z| = 34.5$ and 46.5 cm, see Figure 3.2. These layers are consisting of modules supported by a carbon structure. The n-on-n silicon sensors are 285 μm thick and are connected by bump-bounds to the integrated readout chip (ROC). Each ROC serves an array of 52×80 pixels. The pixel cell size is $100 \times 150 \mu m^2$ and the analogue pulse height readout allows a similar resolution in $r - \phi$ and z directions of 15-20 μm [42]. During the data taking in 2010-2011 96.9% of the ROCs were active.

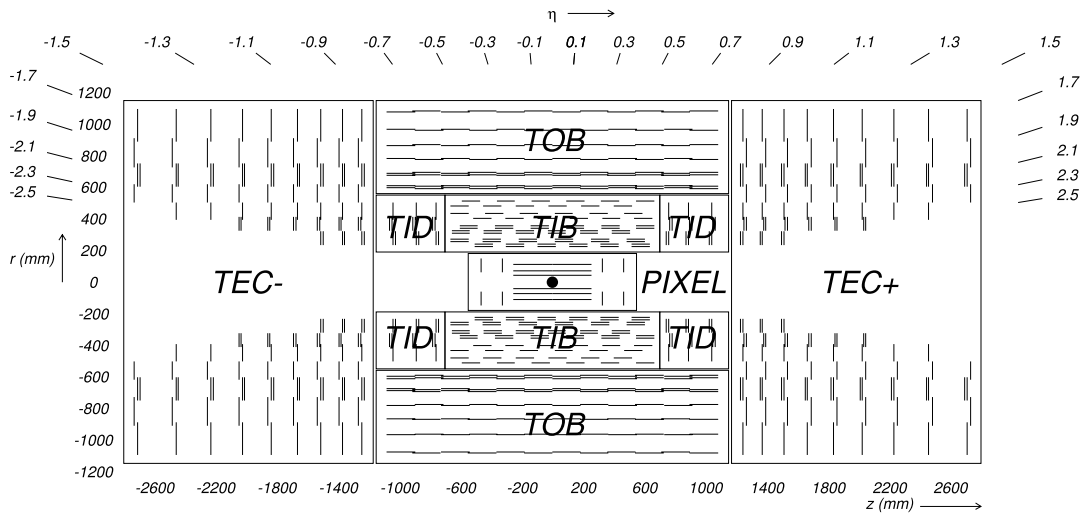

Figure 3.2.: The CMS inner tracking system. Each module is shown as a line [40].

3.4.2. Silicon Strip Tracker

The silicon strip tracker surrounds the pixel detector as shown in Figure 3.2) and is consisting of the inner barrel detector (TIB), the inner discs (TID), the outer barrel detector (TOB) and two endcaps (TEC). These parts add 10 layers of silicon strip detectors to the pixel detector (4 TIB, 6 TOB) in the barrel and 12 detector disks (3 TID, 9 TEC) on each side. There are 15 different sensor layouts used, but all are based on the same p-on-n silicon microchip idea. The strip design only allows for an accurate measurement in one direction[3], this is compensated by double modules (see Figure 3.2). They make a gap free coverage and - due to a stereo angle of 100*mrad* - a measurement in the z-direction is possible.

3.5. Calorimeters

To measure the energies of outgoing particles CMS uses a destructive measurement for electromagnetic and hadronic particles. The calorimeter is subdivided into two parts. The inner part is the electromagnetic calorimeter (ECAL) that is built to provide an accurate electron and photon measurement and encloses the detector for $|\eta| < 3$. The ECAL is a homogeneous crystal calorimeter with three parts, the barrel (EB), endcaps (EE) and the preshower between

[3]For the p_T measurement only the position in the $r - \phi$-plane is important (see Section 4.1).

the tracker and the EE. The hadron calorimeter (HCAL) is outside the ECAL and reaches up to $|\eta| < 5.2$. The high pseudo rapidity coverage is important for a good $E_{\mathrm{T}}^{\mathrm{miss}}$ resolution. Four parts build the HCAL: The three sampling calorimeters in the barrel (HB) between the ECAL and the solenoid, the endcaps (HE) behind the EE and hadron outer (HO) uses the solenoid as absorber. The hadron forward (HF) is a Cerenkov radiation based calorimeter that covers the high η ranges $3 < |\eta| < 5$.

3.5.1. Electromagnetic Calorimeter

One of the goals of the electromagnetic calorimetry is to distinguish a π^0 decaying into two photons from a Higgs in the same channel. The use of the homogeneous $PbWO_4$ crystal calorimeter has several advantages. The 75848 crystals are highly dense ($8.28 g/\,\mathrm{cm}^3$) and have a short radiation length ($X_0 = 0.89\,\mathrm{cm}$) and a small Molière radius of 2.2 cm. This allows a fine granularity of the optically clear crystals and compact geometry which results in a fast response needed with the 25 ns bunch crossing [4] and a good spatial resolution. The crystals in the EB have 360-fold granularity in ϕ and 2×85-fold in η. For the geometrical arrangement see Figure 3.3

The 230 mm long EB crystals have a tapered shape varying with the position in η with a front

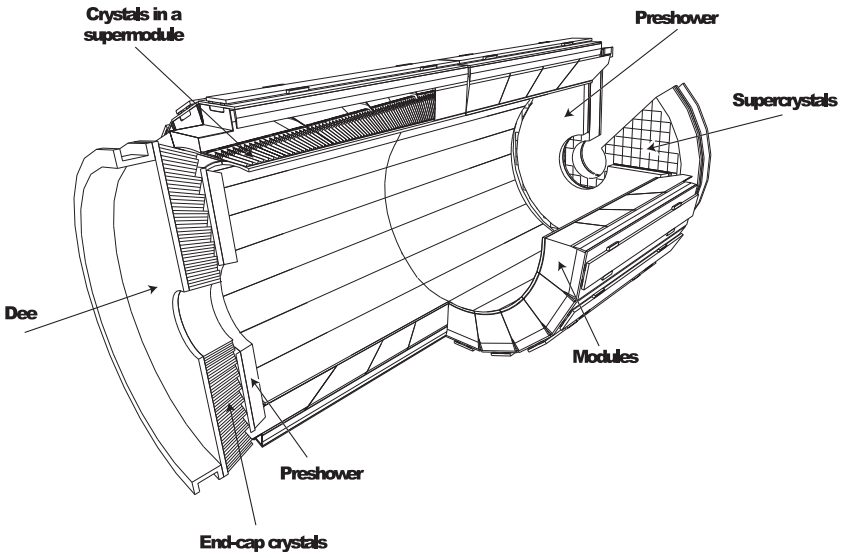

Figure 3.3.: The CMS electro magnetic calorimeter [40].

face cross section of about $22 \times 22\,\mathrm{mm}^2$ and a rear face of about $26 \times 26\,\mathrm{mm}^2$. The EE crystals are organised in two half cycles and have a front face cross section of $28.62 \times 28.62\,\mathrm{mm}^2$ and at the rear $30 \times 30\,\mathrm{mm}^2$ with a length of 220 mm[5].

For the readout two different photo detectors are used. In the barrel region avalanche photodiodes (APD) and in the endcap vacuum photodiodes (VPT) are applied. In both about 4.5 photoelectrons are collected per MeV of the deposited energy. Because the light output of the crystals and the efficiency of the APD vary with the temperature the ECAL is held on a stable temperature of 18°C by a water cooling system, and thermally isolated from the tracker.

[4] 80% of the light with a wave length of 420-430 nm is emitted after 25 ns

[5] The length of the ECAL crystals is equivalent to $25.8 X_0$ in EB and $24.7 X_0$ in EE

The different design choices are due to influences of the 3.8 T magnetic field, operation voltage, radiation hardness and module geometrical dimensions. The difference in quantum efficiency (75% for APD and 22% for VPT) is compensated by the larger active area (280 mm^2 VPT, 25 mm^2 APD).
In the η region $1.65 < |\eta| < 2.6$ the spatial resolution of the ECAL is improved by the preshower detector. The preshower is a four layer sampling calorimeter with a $2X_0$ lead layer in front of a silicon strip detector, followed by a further $1X_0$ lead layer and a silicon strip detector with an orthogonal orientation with respect to the first silicon strip layer. This allows a fine spatial resolution of photon and electron events in the ECAL and therefore is able to resolve a $\pi^0 \to \gamma\gamma$ decay.
The energy resolution of the ECAL can be separated into three parts:

$$\left(\frac{\sigma}{E}\right)^2 = \left(\frac{S}{\sqrt{E}/\,\mathrm{GeV}}\right)^2 + \left(\frac{N}{E/\,\mathrm{GeV}}\right)^2 + C^2. \tag{3.7}$$

S is the stochastic term due to the fluctuations in the shower process, N is the noise term due to digitisation, electronics and pile up and the constant term due to imperfect calibration. In test beams the ECAL calibration has been determined to be:

$$\left(\frac{\sigma}{E}\right)^2 = \left(\frac{2.8\%}{\sqrt{E}/\,\mathrm{GeV}}\right)^2 + \left(\frac{12\%}{E/\,\mathrm{GeV}}\right)^2 + (0.3\%)^2. \tag{3.8}$$

3.5.2. Hadron Calorimeter

One of the main challenges of the CMS detector is the accurate jet-p_T measurement. Because of the hadronic nature of the colliding beams and the high pile up the measurement of the hadronic activity is crucial for every observed physics process. All hadron calorimeters in CMS, except HF, are sampling calorimeters.
The HB is located between the ECAL and the solenoid up to $|\eta| < 1.3$ and is built out of 36 identical wedges that are separated in two η parts. Each wedge has one steel plate on the front and back and 14 brass planes between the plastic scintillator layers. The scintillators are quartered in ϕ and divided into 16 η sectors. The HB material has an interaction length of $\lambda_I = 16.42$ cm, which adds $10.6\lambda_I$ at $\eta = 1.3$ to the $1.1\lambda_I$ of the ECAL. The scintillator light is collected by a wavelength-shifting fibre, whose light is readout by a hybrid photodiode.
The HE covers the pseudo rapidity ranges of $1.3 < |\eta| < 3$. On average this region is exposed to 34% of the final state particles. Therefore the HE is built to be radiation hard and gap-less. The hole HE is attached to the muon endcap and is self-supporting. The absorber-scintillator design is similar to the HB with 17 scintillator layers and slight variation in the materials. The resolution is $\Delta\eta \times \Delta\phi \approx 0.0.87 \times 0.087$ for $|\eta| < 1.6$ and $\Delta\eta \times \Delta\phi \approx 0.17 \times 0.17$ for $|\eta| > 1.6$. The HE is about $10\lambda_I$ thick.
Because the HB and EB have not enough stopping power to contain all hadronic showers in the barrel the HO is added behind the solenoid. The HO scintillator plates are placed directly behind the solenoid on the muon chamber rings. The central ring has an additional layer behind the first iron-yoke to compensate for the minimal absorber depth. This guarantees a minimal absorber depth of $11.8\lambda_I$ in nearly the hole CMS. The HO is segmented in η and ϕ to roughly match the spatial segmentation of the HB.
The HF is 11.2 m from the IP and is a cylindrical structure with a radius of $12.5 < r < 130$ cm. The forward region has the harshest radiation conditions in the detector. On average 760 GeV

energy is deposited per proton collision in the HF, while only 100 GeV are deposited in the rest of the detector. The HF is a Cerenkov detector with quartz fibres embedded between grooved steel plates. This design allows to measure mainly the energy of the electromagnetic showers. The fibres start different distance from the IP to differentiate between electrons and pions. While the light pulses of the scintillators in HB, HE and HO are only to 68% in a 25 ns interval the HF has only 10 ns long shape pulses. The HF therefore is not effected by out of time pile up, which will be described in Section 6.7. The energy resolution of the HCAL alone has been determined to be:

$$\left(\frac{\sigma}{E}\right)^2 = \left(\frac{120\%}{\sqrt{E}/\,\mathrm{GeV}}\right)^2 + (6.8\%)^2. \tag{3.9}$$

This can be improved by a combination of the HCAL with the ECAL and tracker, see Section 4.3.

3.6. Solenoid

The CMS solenoid is an integral part of the detector and allows a p_T measurement of all charged tracks in the detector. It is designed to reach a homogeneous field of 4 T and is operated at 3.8 T. It has a diameter of 6 m and is 12.5 m long. The 220 t of cold mass can store an energy of 2.6 GJ at full current. This energy and the ratio between stored energy and cold mass is beyond any previous solenoid. To absorb the magnetic pressure the four *NiTi* Rutherford-type cable layers are reinforced by an aluminium alloy. The magnetic field is returned outside the solenoid by the 10 000 t iron yoke in which the muon system is embedded. For cooling liquid helium is used at a temperature of 4.5 K.

3.7. The Muon System

The muon is the only particle from the hard interaction that penetrates all detector components. For a precise measurement of muons with p_T up to $\sim$ TeV a large muon system is important. The muon system in CMS is used for identification, measurement and triggering. About 25 000 m^2 are covered with 3 different gaseous detectors.The barrel is surrounded by 4 stations of drift tube chambers (DT) in $|\eta| < 1.2$. The endcap regions are instrumented by cathode strip chambers (CSC) between $0.9 < |\eta| < 2.4$ in 4 stations. To trigger muons independently from the tracking system the barrel and parts of the endcaps ($|\eta| < 1.6$) are instrumented with resistive plate chambers (RPC), which provide a fast, independent, highly segmented trigger with a good time and p_T-resolution.

3.7.1. Drift Tube System

The DT-system is placed between the iron-yokes around the barrel, see Figure 3.4. One wedge (30° in ϕ) consists of 4 stations. The first 3 stations have 3 so called super layers (SL) each made of 4 layers of drift cells (60 in one row) staggered with respect to the next one. The two outer SL are oriented orthogonal to the $r-\phi$ plane to measure the track bending. The innermost SL is oriented orthogonal to the others to measure the z-component of the track. The fourth station has only 2 SL with 70 tubes in one row measuring the ϕ component of the track. One drift cell, as seen in Figure 3.5, is $13 \times 42\,\mathrm{mm}^2$ and consists of a 50 μm/ ns gold-plated

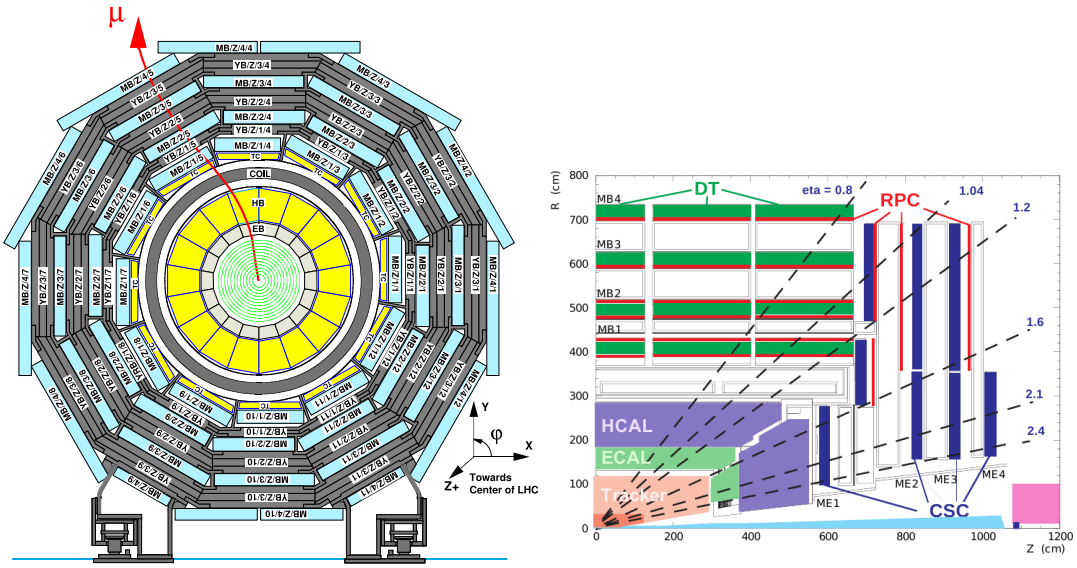

Figure 3.4.: The muon system is the outer tracker of the CMS detector. While the drift tubes in the barrel are arranged between the iron yoke, in the endcap a combination of RPCs and CSCs is used [43].

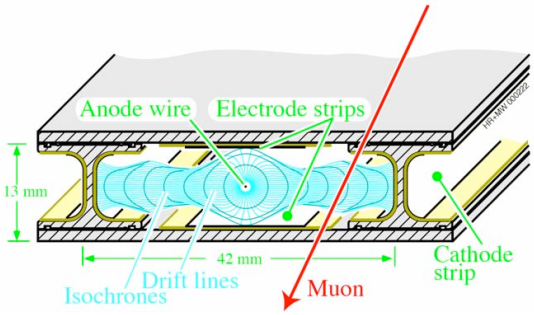

Figure 3.5.: Sketch of a drift tube cell showing drift lines and isochrones [40].

stainless-steel wire (3.6 kV and 2.4 m long), two electrodes to shape the field (1.8 kV) and two cathodes on the narrow side of the rectangular (-1.2 kV). This configuration is flooded with an Ar/CO_2 mixture (85%/15%) that guaranties an almost linear relation between space and drift-time. With velocities of about 55 μm a single wire has a spatial resolution of about 250 μm, with 8 track points of this quality a $r-\phi$ resolution of 100 μm is possible.

3.7.2. Cathode Strip Chambers

The CSC are organised in 4 stations in each endcap, see Figure 3.4. The system covers a region of $0.9 < \eta < 2.4$ of the detector and therefore has an overlap with the DT system. Each station is composed of several trapezoidal chambers with 7 plates which are staged with 6 gas filled gaps covering a $\Delta\phi$ region of 10°or 20°, see Figure 3.6. In the gaps anode wires are stretched azimuthally at a constant r. The cathodes are made of a fibreglass/epoxy material clad with copper. The strips are milled in the plates at a constant $\Delta\phi$. While the wire has a spacing of

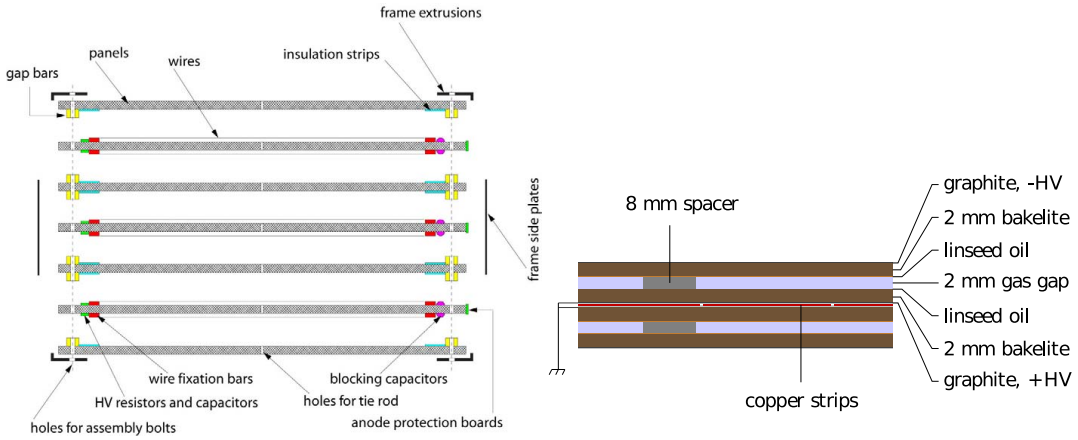

Figure 3.6.: The left Figure shows the CSC composition [44]. The right Figure shows the RPC composition [45].

3.2 mm[6] the cathodes vary their pitch from 8.4 mm to 16 mm with a gap of 0.5 mm to cover a constant $\Delta\phi$. This construction is not too sensitive to slight temperature or pressure variations and can therefore operate without constant monitoring of the $40\%Ar + 50\%CO_2 + 10\%CF_4$ gas mixture. The operating voltage is 3.6 kV. This allows a gas gain of the order of 7×10^4. From the combination of the radial and azimuthal information a spatial resolution of $\approx 75\,\mu$m is achieved for the innermost stations (ME1/1 and ME1/2 see Figure 3.4) and $\approx 150\,\mu$m for the others.

3.7.3. Resistive Plate Chambers

The RPCs [45] are used for triggering and timing. The modules are placed in the detector between the DTs and the CSCs, see Figure 3.4. Each RPC is made of four bakelite plates arranged symmetrically around copper strips in the centre between the innermost plates. The outer plates have a gap of 2 mm between each other and are coated with graphite on the outside, see Figure 3.6. The gap is filled with a gas mixture[7]. The RPC are operated in avalanche mode and allow a muon tagging in one bunch crossing (BX), as well as additional spatial information. The RPC copper-strips have a pitch of 5/16°in ϕ and different length in η[8]. In an upgrade for higher luminosity the RPC system will be extended to cover $|\eta| < 2.1$.

[6]The wires in the innermost station ME1/1 and ME1/2 have a smaller gas gap, finer wires and a spacing of 2.5 mm. Because they are operated near the Solenoid the wires are tilted by an angle of 29°and do not have a constant r-coordinate.

[7]95.2% $C_2H_2F_4$, 4.5% C_4H_10 (isobutane) and 0.3% SF_6 and 35% -40% humidity at 21°C

[8]57 cm to 125 cm in the barrel and 47 cm to 7 cm in the endcap

4. Object Reconstruction and Trigger

In order to identify and analyse the events recorded by the CMS detector, the various particles from the interaction have to be reconstructed. This analysis uses the Z+$E_{\mathrm{T}}^{\mathrm{miss}}$ channel with the Z decaying to muons. Therefore muons will be discussed in more detail in the following. As will be seen in Section 7.3 the influence from jets on the final state is one of the biggest. Therefore jet reconstruction and correction is an important part of this analysis. The $E_{\mathrm{T}}^{\mathrm{miss}}$ is one of the most complex objects reconstructed in the detector, therefore some studies have been performed to show various aspects of this quantity.

4.1. Muon Reconstruction

The ability to reconstruct and measure muons in a wide p_T range is one of the essential features of CMS. Many Standard Model and beyond the Standard Model studies rely on the often clean muon events. The muon is the only particle that can be detected in the muon system (as the name implies). The momentum is calculated from the bending in the 3.8 T magnetic field. The identification of the muon is very clean and highly efficient. The reconstruction however has certain difficulties that have to be addressed by the used algorithm. The muon as minimal ionising particle (MIP) can not be stopped easily in a calorimeter. However if a muon interacts with the detector material, the algorithm has to take the energy loss into account and the bending radius has to be corrected. In summary the muon reconstruction has to consider:

- varying detector resolution depending on the position in the detector
- (catastrophic) energy loss
- misalignment
- backgrounds from radiating muons and punch-through jets
- inhomogeneous $\vec{B}$-field

Since the CMS detector is compact and the muon system is embedded into the iron return yoke of the solenoid the biggest issue is energy loss from multiple scattering. The track algorithm in CMS is divided into four steps: *track finding*, *track building*, *track cleaning* and *track smoothening*.
The problem of track reconstruction is not limited to the muon. The following can be applied for every particle trajectory in CMS.

4.1.1. Seed Generation

To start a track building a start point is needed, to constrain the possibilities. In principle one can start a track from every two points in the detector. In praxis muons are either seeded in

the tracker or in the muon system [46].
In the tracker seeds are built from either two or three hits with a vertex constraint. To cover all possibilities an iterative approach is used, developed within the particle flow technique. First all tracks with a hard seed constraint are reconstructed and all associated hits removed and then the constraints are loosened until all tracks are reconstructed. The configurations are shown in Table 4.1. For tracks in the muon system the seeding is simpler since the activity is much smaller. Based on some geometrical constrains hits in two segments are combined to a rough track seed.

Iteration	Seeding Layers	p_T min cut [GeV]	d_0 cut [cm]	z_0 cut
Zero	pixel triplets	0.8	0.2	3.0σ
1	pixel pairs	0.6	0.05	0.2 cm
2	pixel triplets	0.075	0.2	3.3σ
3	Triplets: pixel, TIB1,2, TID/TEC ring 1,2	0.25-0.35	2.0	10σ
4	Pairs: TIB1,2 TID/TEC ring 1,2	0.5	2	12σ
5	Pairs: TOB1,2 TEC ring 5	0.6	6	30σ

Table 4.1.: The seed configuration for iterative tracking in CMS inner tracker [47]. The quantities d_0 and z_0 denote the transverse and longitudinal impact parameters with respect to the nominal interaction point.

4.1.2. Kalman Filter

There are multiple approaches to reconstruct a track from a seed. In CMS an iterative Kalman Filter (KF) is used to build tracks. A detailed description can be found in [48, 49]. The central equations of the KF are

$$x_k = F_{k-1}x_{k-1} + w_{k-1} \tag{4.1}$$
$$m_k = H_k x_k + \varepsilon_k \tag{4.2}$$

the state vector e.g. $x_k = (x, y, \frac{\partial x}{\partial z}, \frac{\partial y}{\partial z}, q/|\vec{p}|)$ is described by all previous state vectors x_{k-1} see Equation 4.1 that are propagated with a physics motivated propagator F_{k-1} and a random term w_{k-1} to the state k. The state vector is also constrained by the measurements[1] m_k, see Equation 4.2, with the Hesse-matrix H_k and a possible random term ε_k.
The KF has three important steps and functionalities:

- **Prediction** of the state-vector x_k is based on all previous measurements m_{k-1} and the resulting state-vectors x_{k-1}. The search area in the detector can be drastically reduced.
- **Filtering** the measurements m_k can be used to update the state-vector x_k.
- **Smoothening** each state-vector x_k can be checked, based on the measurements after the state k.

The following kinds of propagators are used in CMS [50]:

- analytic with material

[1] A measurement here means a tracker hit or vertex constraint.

- Runge-Kutta
- stepping-helix

By the use of these propagators the different physics conditions in the detector are taken into account. The first two are used within the silicon tracker with a homogeneous magnetic field (analytic with material) or in the forward region (Runge-Kutta). In the muon system the stepping helix propagator is used.
The iterative approach with the track seeding reduces the CPU time, because the hits matched to good seeds can be neglected by the tracking algorithm in the next iteration. In the fist iteration about 99.5% of isolated muons can be matched and more than 90% of the charged hadrons. By loosening the vertex criteria and widening the hit patterns to the endcaps a good reconstruction efficiency close to 100% is possible.

4.1.3. Standalone Muon

The tracks reconstructed in the muon spectrometer alone are called *Standalone muons*. The muon spectrometer is essential for high energy muons with $10\,\text{GeV} \leq p_T \leq 1\,\text{TeV}$. Muons below an energy of about 10 GeV often do not leave the inner part of the detector or have not enough hits in the muon system. All standalone muons are constrained to the vertex. The standalone muon p_T resolution is about 10%.

4.1.4. Tracker Muon

The tracker muon is reconstructed in the tracker alone and therefore uses pixel seeds. The track is then loosely matched to information from the calorimeters and the muon system. Low energy muons ($p_T < 30\,\text{GeV}$) have a p_T resolution in the order of 1%.

4.1.5. Global Muons

To get the best resolution for all muons the standalone muon tracks are matched with the tracker tracks. This improves the resolution for high energy muons drastically. The global muon is based on a standalone muon track, based on which a $\eta - \phi$ region in the tracker is chosen. Best matching tracks from this region are chosen and refitted with hits from the whole system, see Figure 4.1.

4.2. Trigger

At the expected design luminosity events with a rate of $10^9 Hz$ are expected in the CMS detector. It is not possible to reconstruct and store this high rate, therefore the rate has to be reduced to the order of $10^2 Hz$. CMS uses a two level trigger system.

- A (Level-1) (L1) trigger is built up from fast programmable electronics and reduces the event rate to about $30kHz$. The L1 trigger uses information from the calorimeters and the muon systems. The time from the bunch crossing to the trigger decision is in the order of 3 μs.

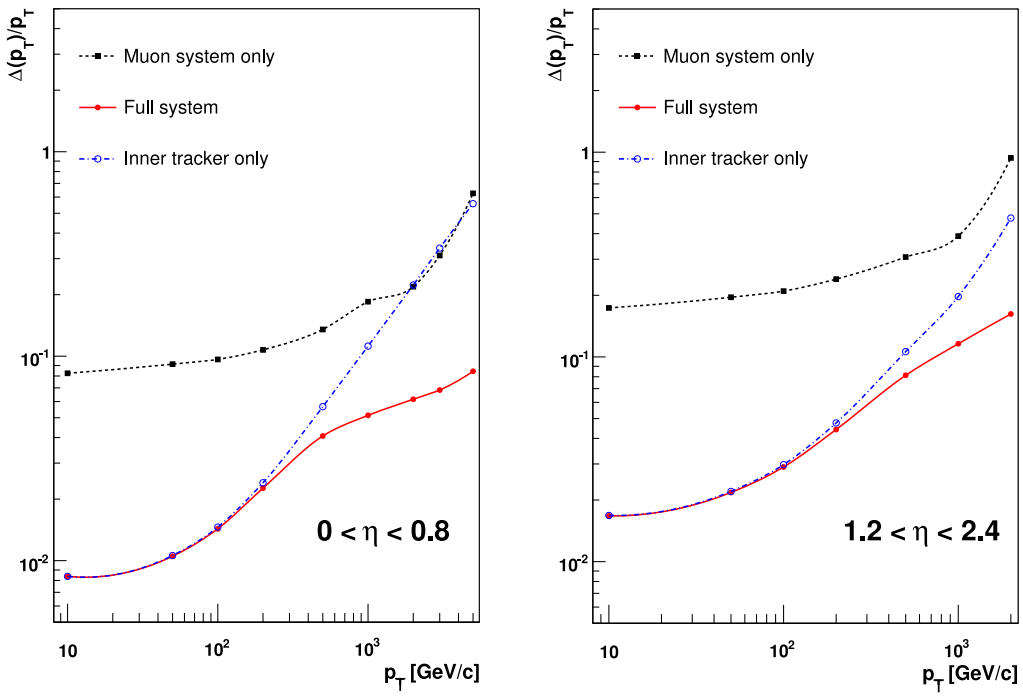

Figure 4.1.: The Figure shows the CMS muon resolution vs muon p_T for different η ranges [50].

- The high level trigger (HLT) is a software based filter running on a computing farm. The HLT uses the full detector information and a reconstruction similar to the offline reconstruction. The time per event is in the order of 1 s.

4.2.1. Muon Trigger

On the L1 trigger level the used muon systems are DT, CSC and RPC. In the DTs and RPCs a rough track momentum assignment and quality estimate is made. The muon with the highest quality is then forwarded to the Global Trigger, which combines information from calorimeter and muon system and decides if the event is passed to the HLT.
The HLT itself is divided into two steps called Level 2 (L2) and Level 3 (L3). The L2 reconstructs the muon track in the muon system using the same track builder method as in the offline reconstruction, an the L3 reconstructs the muon in the tracker, with the η, ϕ constraints from the L2 fit. The event rate can be reduced by requiring a minimal p_T or quality requirements, e.g. a isolation.

4.3. Particle Flow and Electron Reconstruction

The aim of the particle-flow technique is the reconstruction and identification of all particles in the detector by using all the available information of all CMS sub-detectors. The difference to the "classical" reconstruction becomes clear with a view on a quark or gluon jet with a p_T of 500 GeV. The jet consists of stable particles with an average p_T of 10 GeV. By reconstructing all stable particles one gains information on the origin of this jet and potential composition.

Classical jet reconstruction algorithms such as CaloJets only consider calorimeter measurements as input and therefore have only limited information of the jet evolution in the detector. The CMS detector with the large high resolution tracker and the high magnetic field is ideal for linking charged particle tracks with the information in the calorimeters. The particle-flow technique distinguishes between six types of stable particles in the detector: muons, electrons, charged hadrons, neutral hadrons, photons[2] and energy deposited in the hadron forward detector. This collection of linked information allows an integration of tags to the objects, such as b-jets, taus and pile up.

4.3.1. Electrons

Electrons in contrast to muons radiate Bremsstrahlung in the tracker, and the Kalman Filter is not the best track builder. Electrons therefore are reconstructed with the Gaussian-Sum-Filter (GSF) method, which allows to take the changing curvature into account. The standard electron reconstruction in CMS [51] uses ECAL seeds to trigger GSF-tracking. In particle-flow tracks that match ECAL entries are considered electrons and the GSF-track is tracker seeded.

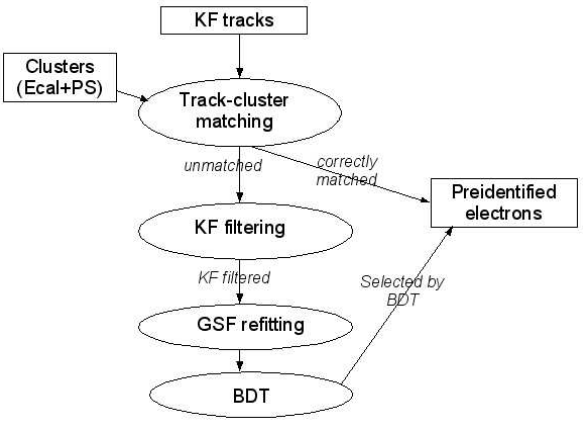

Figure 4.2.: Workflow of the particle-flow electron reconstruction [52]

4.3.2. ECAL Seeds and Clusters

The ECAL is constructed to contain 94% of the energy of an electron in 3×3 crystals (97% in 5×5) [53]. Electrons are charged and therefore bent in the 3.8 T magnetic field of CMS. The emitted Bremsstrahlung is spread in ϕ and a so called supercluster (SC) of clusters is formed. The clusters formed by an unconverted photon are mostly isolated in the ECAL and therefore easily identifiable. Converted photons however have the same cluster shape in the ECAL as electrons for obvious reasons. The conversion probability in the CMS tracker is 30-70% and very dependent on η. These converted photons can be separated from prompt electrons by requiring hits in the first pixel layers and the goodness of the supercluster-track matching.

[2]Electrons and photons are sometimes referred to as charged and neutral electro-magnetic signatures.

The clusters formed by the particle flow algorithm are formed differently, because they are used for photons, electrons, charged and neutral hadrons. The clusters are formed separately in each subdetector, e.g. ECAL barrel or HCAL endcap. A seed has to have one crystal with a higher threshold and is then grown to a topological cluster, by adding neighbour crystals above a certain threshold.

4.3.3. Particle Flow Candidates

The particle flow algorithm tries to categorise all measured hits in the detector. The assignment is done iteratively. First all tracks and possible calorimeter entries from global muons[3] are assigned and removed for the next iteration. In the next step all electrons are assigned and removed. The remaining tracks are then cleaned for fake tracks. The non fake tracks give rise to charged hadrons and charged electromagnetic candidates. The remaining clusters are categorised as neutral electromagnetic candidates, photons and neutral hadrons. The decision for the type is based on the goodness of the match between tracks and ECAL and HCAL clusters. If tracks can not be associated a relaxed search for muons and fake tracks is performed and then another associating charged hadrons and photons. The collection of all particles reconstructed by the particle-flow algorithm is called particle-flow candidates (PFCandiates).

4.3.4. Particle Flow Jets

Particles that decay hadronically are not measured as one particle in the detector. They form a hadronic cascade and build a pattern in the detector. To describe these objects so called jets are formed. There are different algorithms that are used to form the patterns to a jet. The most popular types are sequential recombination algorithms [54] (e.g. k_T, Cambridge/Aachen and anti-k_T) and cone jet algorithms (e.g. SISCone). These jet algorithms have to describe the physics event in the right way, therefore these algorithms have to be infrared-safe, collinear save and not seed dependent. The last one is not entirely possible in a detector, because of the electronic noise there will always be seeds, but in theory the SISCone algorithm should be seedless. The infrared-safety of a jet algorithm means that it should be save against soft-QCD effects like additional contributions from low energy radiation. A collinear save algorithm is insensitive to splitting partons.
In CMS the anti-k_T algorithm is mainly used, which has a similar algorithm structure to the k_T and Cambridge/Aachen. The used observables are the jet-p_T- which is called k_T as a convention in this section - and ΔR the difference of two objects in the detector. The key ingredient to the sequential recombination algorithms is that one defines a distance between two objects

$$d_{ij} = min(k_{Ti}^{2p}, k_{Tj}^{2p}) \frac{\Delta R_{ij}^2}{r}. \tag{4.3}$$

The algorithm starts at a seed, e.g. the highest k_T of the so called protojets[4], and then searches for the nearest protojet with the defined distance 4.3. If the distance is smaller than

[3] The muon has to satisfy certain quality criteria, such as the global muon fit has to be compatible with the tracker muon within 3σ of the track p_T.
[4] For particle-flow jets these are all PFCandiates without the well identified electrons and muons

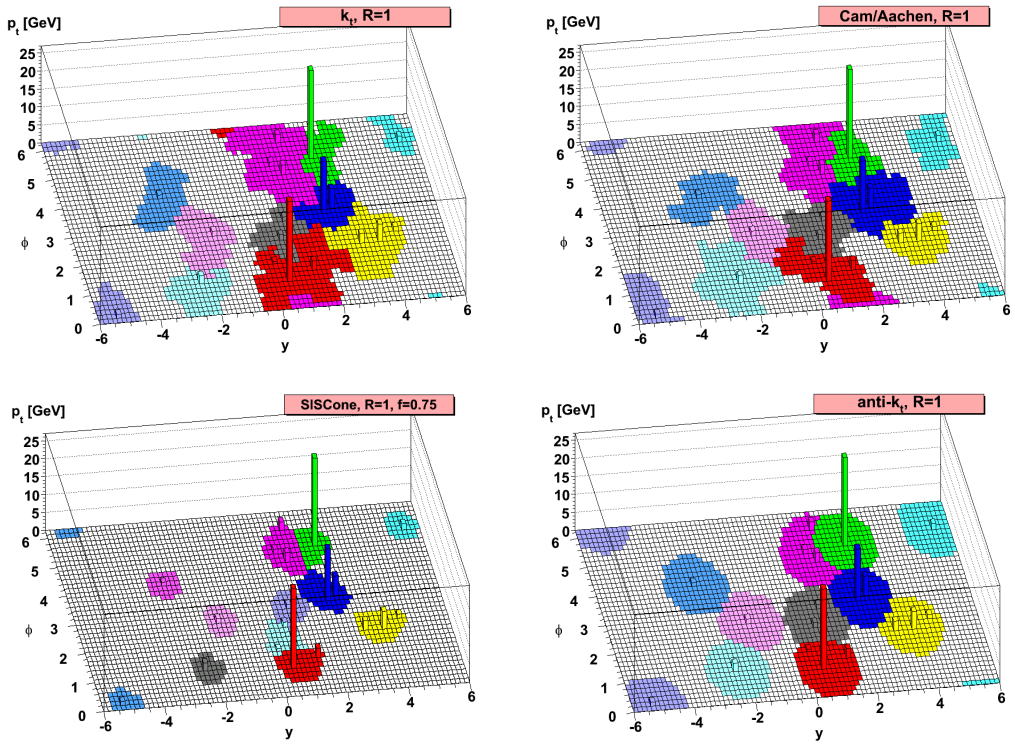

Figure 4.3.: The comparison of jet algorithms in the plane of ϕ and the rapidity y. Clear differences for the different algorithms can be observed [54].

a certain threshold the protojets are combined and the first step is repeated. If the distance is higher than the defined threshold the next highest k_T-protojet is calculated without the already associated measurements.
The anti-k_T algorithm means that p in equation 4.3 is set to -1 in contrast to the k_T-algorithm with $p = 1$ or the Cambridge/Aachen-algorithm with $p = 0$. The resulting jets of the anti-k_T-algorithm are conical in the $\phi - \eta$ plane, in contrast to other algorithms, see Figure 4.3.

4.3.5. Jet Energy Calibration

The energy measurement for jets is complex, for more details see [55]. To relate the measured jet energy to the energy of the corresponding true particle jet a correction is applied. A true particle jet is a jet resulting from the clustering of stable generator particles[5] with the same algorithm used in the reconstruction. Corrections from different sources can be applied. The scheme is illustrated in the equation below:

$$C = C_{offset}(p_T^{raw}) \cdot C_{MC}(p'_T, \eta) \cdot C_{rel}(\eta) \cdot C_{abs}(p''_T) \tag{4.4}$$

The first correction applied is the offset correction $C_{offset}(p_T^{raw})$ which removes additional energy due to noise or pile up. The MC calibration $C_{MC}(p'_T, \eta)$ is applied to calibrate the detector response and remove non-uniformity in η and non-linearity in p_T. Finally the residual

[5]Stable generator particles means the particles simulated by a simulation of a physics process after the hadronisation.

corrections $C_{rel}(\eta)$ and $C(p_T'')$ correct for small differences in data and simulation. Each step uses the output from the previous step as input.
For the offset correction the jet area method is used. As input the average p_T density ρ per unit area is calculated per event and the jet area is determined per jet, where the energy density ρ characterises the soft-QCD activity in an event. The jet area is determined with the k_T jet clustering algorithm and a distance parameter of 0.6. The correction can be summarised to

$$C_{area}(p_T^{raw}, A_j, \rho) = 1 - \frac{(\rho - < \rho_{UE} >) \cdot A_j}{p_T^{raw}}. \tag{4.5}$$

The quantity $< \rho_{UE} >$ denotes the event independent offset due to electronic noise and is determined from events with no pile up[6] to be 1.08 GeV.
The MC calibration is based on the simulation and relates the reconstructed jet to the MC-truth information. All jets are matched to true, simulated jets[7] and the response $R = \frac{p_T^{reco}}{p_T^{gen}}$ is calculated. The correction then is the p_T^{reco} and η dependent average inverse response

$$C_{MC}(p_T^{reco}, \eta) = \frac{1}{< R(p_T^{reco}, \eta) >}. \tag{4.6}$$

The relative and absolute corrections are only applied to data. The aim of these calibrations is to tune the detector response to the expected and understood results obtained from simulation.
The relative energy scale is determined using the dijet p_T-balancing method, by relating the jet response of a barrel jet with $|\eta| < 1.3$ to jets with an arbitrary η. This is achieved using the correction equation:

$$C_{rel}(\pm\eta) = \frac{k_{rad}(|\eta|) \cdot C_{sym}(|\eta|)}{1 \mp \mathcal{A}_R(|\eta|)}. \tag{4.7}$$

The components are defined in the appendix A.2. The input is taken from dijet events in data and simulation.
The absolute energy correction is obtained from γ/Z events. The assumption is that γ/Z events do not have $E_{\mathrm{T}}^{\mathrm{miss}}$ and a missing transverse energy projection fraction ratio R_{MPF} is defined as:

$$R_{MPF} = R_{\gamma,Z} + \frac{E_{\mathrm{T}}^{\mathrm{miss}} \cdot \vec{p}_T^{\,\gamma,Z}}{(p_T^{\gamma,Z})^2}, \tag{4.8}$$

where the γ/Z response $R_{\gamma,Z}$ is set to one. The corresponding correction is then defined as:

$$C_{abs} = \frac{< R_{MPF}^{MC} >_{p_T^{\gamma/Z}}}{< R_{MPF}^{data} >_{p_T^{\gamma/Z}}}. \tag{4.9}$$

The systematic uncertainties on the p_T and η corrections are determined from crosschecks with additional data driven methods. The resulting p_T resolution is better than 10% for $2 \leq \eta \leq 2.5$, see Figure 4.4, and the jet energy scale uncertainty is below 3% for jets with $\eta = 2$ and $p_T \geq 30$ GeV.

[6] No pile up in this context means events with one reconstructed vertex.
[7] The matching requirement is $\Delta R < 0.25$.

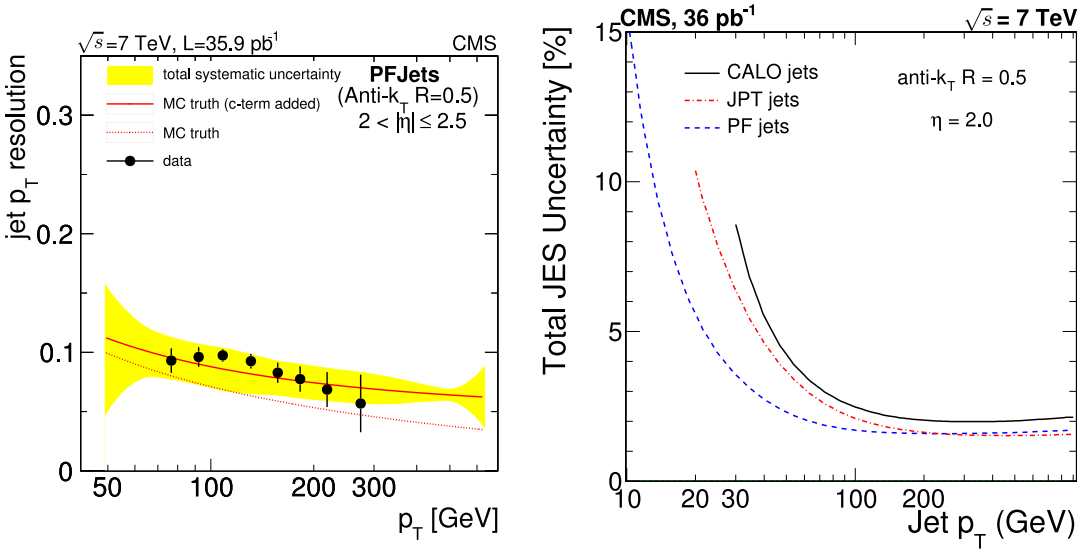

Figure 4.4.: The jet energy resolution (right) and jet energy scale uncertainty (left) are well measured with the particle flow method [55].

4.3.6. b-Tag

The b-quark is the only quark, which hadronises in an observable distance from the vertex. This allows flavour tagging for b-jets. The existing algorithms [56] used to tag b-jets can be categorised in four groups:

- impact-parameter based
- secondary vertex
- lepton based
- multi variable based

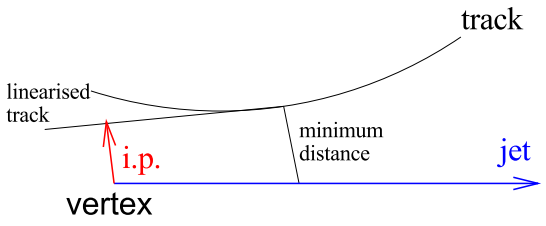

Figure 4.5.: The impact parameter for b-tagging [56].

The algorithm used in this analysis is impact-parameter based. Important for all algorithms is the reconstruction of tracks with a high resolution at the vertex. The particle flow approach therefore is ideal with the matching of track information to calorimeter entries and the dedicated track reconstruction. The impact parameter is shown in Figure 4.5 and can be measured in 3D with the CMS Tracker. To account for the different track accuracy depending e.g. on

the number of hits, an impact-parameter significance is constructed

$$S = \frac{IP}{\sigma_{IP}}. \tag{4.10}$$

The Track Counting (TC) algorithm uses this impact parameter and requires at least N tracks to have an impact-parameter significance larger than a given threshold. For a positive TC-tagger the threshold or discriminator is the impact-parameter significance of the Nth track, where the tracks are ordered with decreasing significance. TC algorithms with $N = 2$ are called "high efficiency" (TCHE) and with $N = 3$ "high purity" (TCHP). For the negative values of the discriminator the order is reversed. In the following the TCHE-tagger is used with a "medium" working point (TCHEM), that was optimised to have less than 1% contributions from light-flavour jets[8]. Light-flavour jets in this context are jets that originate from u,d or s quarks or gluons. In [57] the TCHEM was optimised using the first 8-15 pb^{-1} in 2010 to be 3.3.
In the 2011 dataset the tagging efficiency is 0.66 [58] with a data/MC scale factor of 0.96 ± 0.04 [57]. The mistag probability for light-flavour jets is 0.0286 ± 0.0003 (stat) with a data/MC scale factor of $1.20 \pm 0.01 \pm 0.14$.

4.4. Missing Transverse Energy

The missing transverse energy is an important quantity for new physics at a hadron collider. The missing energy can not be used as quantity, because the longitudinal momentum of the initial partons is unknown. But the initial transverse momentum can be neglected, the vector sum of the transverse momenta is conserved in an event and therefore can be used as a observable. Particles that are not measured in the detector like neutrinos or stable uncharged new physics objects like Unparticles therefore would show up in the missing transverse energy. There are different techniques to reconstruct $E_{\mathrm{T}}^{\mathrm{miss}}$.

4.4.1. Calorimeter Driven $E_{\mathrm{T}}^{\mathrm{miss}}$

The calorimeter driven $E_{\mathrm{T}}^{\mathrm{miss}}$ (Calo$E_{\mathrm{T}}^{\mathrm{miss}}$) is the classical approach to reconstruct $E_{\mathrm{T}}^{\mathrm{miss}}$, used at LEP ($\not{E}$) [59, 60, 61, 62] and the Tevatron [63, 64]. Calo$E_{\mathrm{T}}^{\mathrm{miss}}$ is defined as the energy sum of all calorimeter towers above a noise threshold, taking into account the position in the detector. The algorithm corrects for muons, since the energy measured in the calorimeter from muons is momentum independent. The calorimeter entries from muons are subtracted and the muon p_T is added:

$$Calo E_{\mathrm{T}}^{\mathrm{miss}} = -\sum_{\substack{\mathrm{Calo}\\ \mathrm{Towers}}} \vec{E}_T - \sum_{muons} \vec{p}_T + \sum_{muons} \vec{E}_T^{calo}. \tag{4.11}$$

4.4.2. Track Corrected $E_{\mathrm{T}}^{\mathrm{miss}}$

The track corrected $E_{\mathrm{T}}^{\mathrm{miss}}$ (TC$E_{\mathrm{T}}^{\mathrm{miss}}$) is based on the Calo$E_{\mathrm{T}}^{\mathrm{miss}}$, but corrects for the track p_T. Tracks that are not identified as muons or electrons are assumed to be charged pions. The calorimetric energy deposit is not used from the detector, but is estimated from simulation in

[8] This was done with the first data from 2010 with $\sqrt{s} = 7\,\mathrm{TeV}$ and low pile up conditions

different η and p_T bins. Tracks with a $p_T < 2\,\mathrm{GeV}$ are not expected to have a calorimeter entry and therefore taken as they are, whereas calorimeter entries from tracks with a $p_T > 100\,\mathrm{GeV}$ are not corrected.

$$TCE_{\mathrm{T}}^{\mathrm{miss}} = CaloE_{\mathrm{T}}^{\mathrm{miss}} - \sum_{p_T>3} \vec{p}_T^{\,tracks} + \sum_{charged\ \pi} E_T^{calo} - \sum_{charged\ \pi} E_T^{sim} \tag{4.12}$$

4.4.3. Particle Flow $E_{\mathrm{T}}^{\mathrm{miss}}$

The Particle Flow $E_{\mathrm{T}}^{\mathrm{miss}}$ is based on the Particle Flow Candidates and defined as

$$pfE_{\mathrm{T}}^{\mathrm{miss}} = -\sum_{PFCand} \vec{E}_T. \tag{4.13}$$

The particle flow technique gives access to the composition of $E_{\mathrm{T}}^{\mathrm{miss}}$ in an event as can be seen in Figure 4.6(right). This also allows corrections such as pile up (type 0) , JEC (type I) and event balancing (type II). The $E_{\mathrm{T}}^{\mathrm{miss}}$ composition in Figure 4.6 shows that for the Drell-Yan process muons are not the main fraction of the $E_{\mathrm{T}}^{\mathrm{miss}}$. There seems be a peak in the not pile up subtracted fractions at 50 GeV, which means the pile up contribution is maximal in this energy region.
The type 0 correction is based on the pile up identification from the Particle Flow Algorithm. The vertex with the highest $\sum p_T$ from the associated tracks is defined as the primary vertex of an event. Charged hadrons that originate from another vertex are flagged as pile up contribution and therefore are not taken into account in the PFnoPU$E_{\mathrm{T}}^{\mathrm{miss}}$.
The type I correction propagates the jet energy corrections to pf$E_{\mathrm{T}}^{\mathrm{miss}}$. For the correction all jets above a p_T threshold of p_T >10 GeV are taken into account. In the used reconstruction the jet resolution was underestimated in the simulation as can be seen in Section 4.5. This can be corrected by smearing the jets with an additional factor. This factor has to be derived from data and would therefore bias this analysis. Therefore the type I corrected pf$E_{\mathrm{T}}^{\mathrm{miss}}$ is not used in this analysis.
For the type II correction the simulation is tuned to fit the data in events with no real $E_{\mathrm{T}}^{\mathrm{miss}}$. In CMS this optimisation was done with $Z \to ee$ [65].
The difference between the $E_{\mathrm{T}}^{\mathrm{miss}}$ reconstruction algorithms becomes clear by comparing the reconstruction of Drell-Yan events in the muon channel in Figure 4.6 (left). The optimal reconstruction would mean a steeply falling $E_{\mathrm{T}}^{\mathrm{miss}}$ histogram. The Calo$E_{\mathrm{T}}^{\mathrm{miss}}$ therefore shows the worst resolution, followed by the TC$E_{\mathrm{T}}^{\mathrm{miss}}$, which is reasonable good in the low $E_{\mathrm{T}}^{\mathrm{miss}}$ region, in comparison to the particle flow based algorithms, but performs not as well in the high $E_{\mathrm{T}}^{\mathrm{miss}}$ region above 100 GeV. The difference between the particle flow based algorithms can not be concluded from this plot, but they seem to perform best in comparison.

4.5. $E_{\mathrm{T}}^{\mathrm{miss}}$ Reconstruction

To get a measure for the $E_{\mathrm{T}}^{\mathrm{miss}}$ response the $Z \to \mu\mu$ channel is investigated in more detail. The $Z \to \mu\mu$ channel has no intrinsic $E_{\mathrm{T}}^{\mathrm{miss}}$, but since all objects in the detector have a finite resolution such an event has $E_{\mathrm{T}}^{\mathrm{miss}}$. In a $Z \to \mu\mu$ event each muon has a momentum of about 50 GeV and therefore a resolution of about 1%. In a hadron collider the Z is produced in general with hadronic activity recoiling against the Z. Such hadronic activity manifests itself

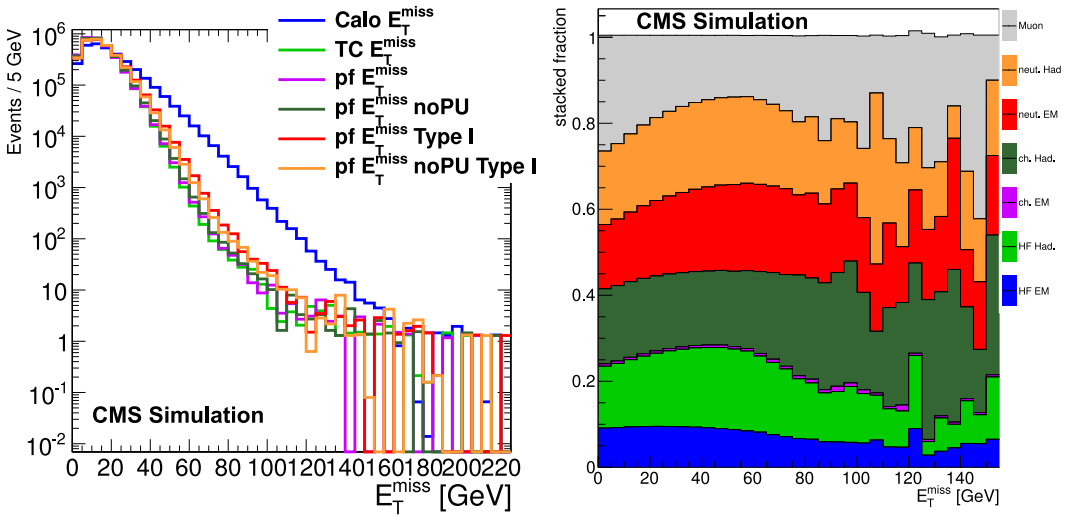

Figure 4.6.: The left Figure shows different reconstruction algorithms for $E_{\mathrm{T}}^{\mathrm{miss}}$. The different pf$E_{\mathrm{T}}^{\mathrm{miss}}$ algorithms have a similar description of the Drell-Yan $\mu-$events where Calo$E_{\mathrm{T}}^{\mathrm{miss}}$ and TC$E_{\mathrm{T}}^{\mathrm{miss}}$ have a slightly worse $E_{\mathrm{T}}^{\mathrm{miss}}$ resolution. The right Figure shows the pf$E_{\mathrm{T}}^{\mathrm{miss}}$ composition for Drell-Yan μ-events.

as one or more jets in the detector, and is due to the remaining part of the hadrons which has to be balanced against the Z. The events should be balanced in the transverse plane:

$$\vec{p}_T^{\,Z} + \vec{u}_T + \vec{E}_{\mathrm{T}}^{\mathrm{miss}} = 0 \tag{4.14}$$

In this context $\vec{u}_T$ denotes the recoil. $\vec{u}_T$ can be expressed on an event by event basis, with respect to the vector boson. The vector boson defines the basis and $\vec{u}_T$ can be parametrised in the transverse $u_\perp$and the parallel component $u_{||}$. A graphical representation is shown in Figure 4.7. With equation 4.14 the definition of $u_\perp$and $u_{||}$is as follows:

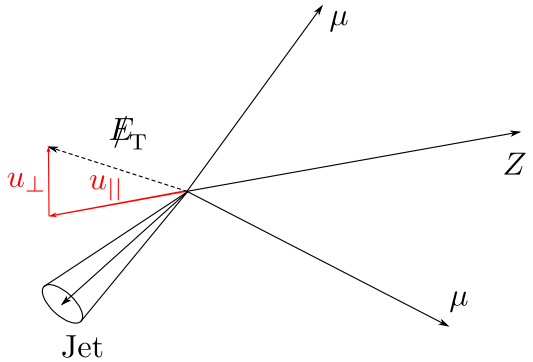

Figure 4.7.: The recoil $\vec{u}_T$ in a $Z \to \mu\mu$ event can be expressed in the basis of the Z-Boson.

$$\vec{u}_T = -(\vec{p}_T^{\,Z} + \vec{E}_{\mathrm{T}}^{\mathrm{miss}}) \tag{4.15}$$

$$u_\perp = \vec{u}_T \cdot \frac{1}{p_T^Z}\begin{pmatrix} p_x^Z \\ p_y^Z \end{pmatrix} \qquad u_{||} = \vec{u}_T \cdot \frac{1}{p_T^Z}\begin{pmatrix} -p_y^Z \\ p_x^Z \end{pmatrix} \tag{4.16}$$

For dimuon events with the selection described in Chapter 5 the recoil is shown in Figure 4.8. The parallel recoil is shifted to negative values, which means that the $E_{\mathrm{T}}^{\mathrm{miss}}$ is mainly generated by mismeasured jets. For positive values around 100 GeV disagreement between data and MC is observed, which shows that this phase space in $E_{\mathrm{T}}^{\mathrm{miss}}$ is not properly covered by the Drell-Yan simulation. In the transverse recoil a disagreement between data and simulation can be observed around 100 GeV as well. A measure for the detector response is the

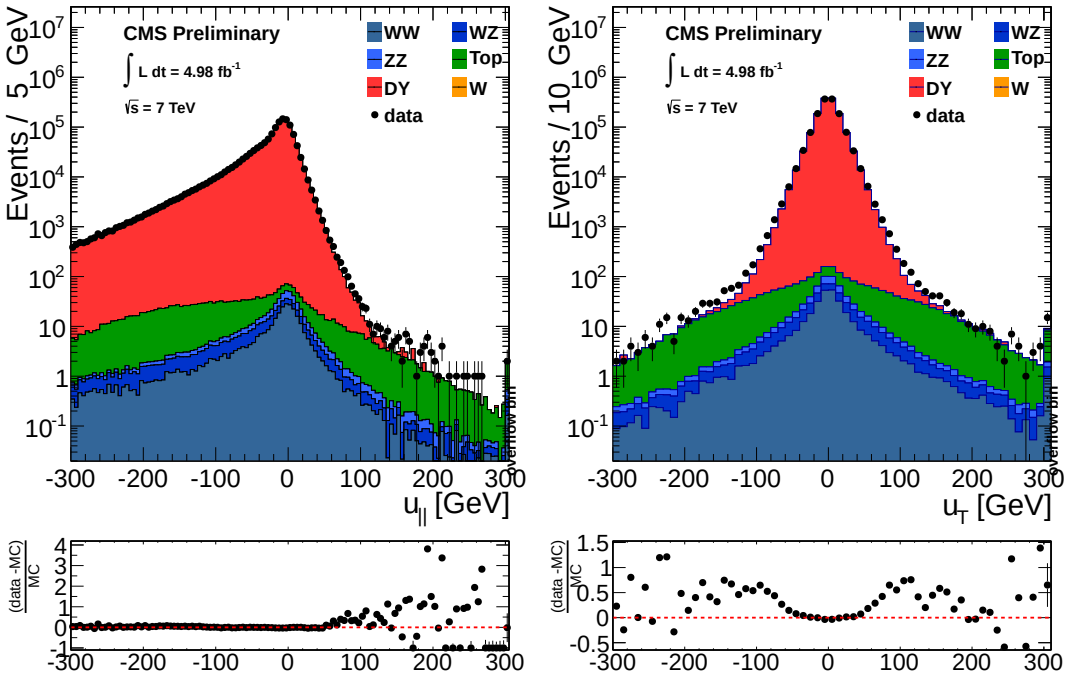

Figure 4.8.: In the left plot $u_{||}$ is shown, in the right plot $u_{\perp}$.

ratio of $u_{\perp}$ to p_T^Z. In an ideal detector this ratio should be one, but for low values of p_T^Z the response is more or less random, because of the multiple influences on such a low $E_{\mathrm{T}}^{\mathrm{miss}}$. The response at low p_T^Z is expected to be random and over all below 1, because a low p_T^Z implies a low p_T hadronic recoil. The detector has an energy threshold in the calorimeters and the tracks, therefore this low energy recoil will not be fully reconstructed and the response will appear to be too low.
The sharpness of this turn on is defined by the ability to reconstruct the low energy activity in the detector. The pf$E_{\mathrm{T}}^{\mathrm{miss}}$ response is shown in Figure 4.9 in comparison to Calo$E_{\mathrm{T}}^{\mathrm{miss}}$. In the comparison one can see that the response for Calo$E_{\mathrm{T}}^{\mathrm{miss}}$ starts at values of 0.6 for low p_T^Z and reaches a plateau at $p_T^Z \approx 50$ GeV, while the pf$E_{\mathrm{T}}^{\mathrm{miss}}$ has a higher start value of 0.8 and reaches a plateau in the same p_T^Z region. The pf$E_{\mathrm{T}}^{\mathrm{miss}}$ fluctuates around a response value of 0.95 and does not reach 1. This means that the jets used for the pf$E_{\mathrm{T}}^{\mathrm{miss}}$ have a potentially underestimated p_T, but the particle flow algorithm can reconstruct objects with a lower p_T better than the calorimeter based algorithm. For the calorimeter based algorithm the response shows some pile up dependency. The type I corrected pf$E_{\mathrm{T}}^{\mathrm{miss}}$ has a response which fluctuates around 1, see Figure 4.10. An Unparticle signal could shift the response curve in the $Z \to \mu\mu$ channel. Since the Type I correction involves a correction in the $Z \to \mu\mu$ channel, this is considered as a potential bias and not used.

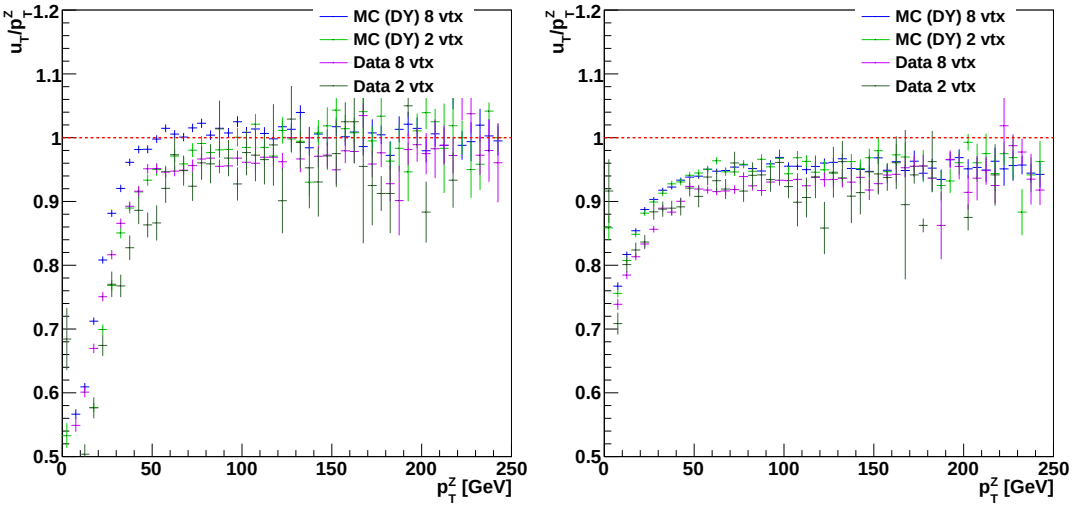

Figure 4.9.: In the left plot one can see the response for Calo$E_{\mathrm{T}}^{\mathrm{miss}}$, while in the right pf$E_{\mathrm{T}}^{\mathrm{miss}}$ is plotted.

The distribution of $E_{\mathrm{T}}^{\mathrm{miss}}$ in ϕ should be flat for an ideal detector. In Figure 4.11 one can

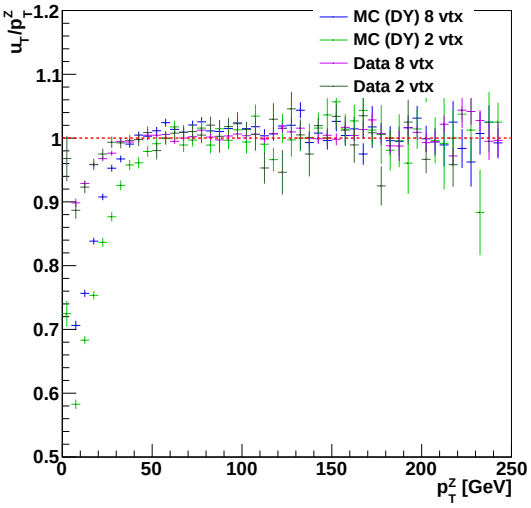

Figure 4.10.: The type I corrected pf$E_{\mathrm{T}}^{\mathrm{miss}}$ response for different vertices is different for data and MC.

see that this is not the case for pf$E_{\mathrm{T}}^{\mathrm{miss}}$. This is due to some dead cells in the HF calorimeter. The difference between simulation and data is due to the fact that these dead cells are not simulated. This difference can be seen in the $E_{\mathrm{x}}^{\mathrm{miss}}$ distribution in Figure 4.11 as a shift from the central value. The activity in the forward region is dependent on the pile up in the event, therefore the shift is dependent on the number of reconstructed vertices in an event. In Figure 4.12 the mean for the $E_{\mathrm{x}}^{\mathrm{miss}}$ and $E_{\mathrm{y}}^{\mathrm{miss}}$ distribution is plotted against the number of vertices. The dependency on the number of vertices is linear and can be fitted with the parameters in table 4.2. It may be noted that even the MC values are not central. With these functions the

	x or y	a [GeV]	b [GeV]
MC	x	-0.05	0.02
	y	-0.45	-0.03
Data	x	0.36	0.23
	y	-0.61	-0.20

Table 4.2.: Parameters from the linear fit ($a + b \cdot vtx$) to the mean in E_x^{miss} and E_y^{miss} distributions depending on the number of vertices (See Figure 4.12).

E_x^{miss} and E_y^{miss} values can be corrected and $\phi_{E_T^{miss}}$ can be recalculated. The result is shown in Figure 4.12. There is still a noticeable difference between the MC description and the recorded data, but one has to keep in mind that no E_T^{miss} cut has been applied and therefore the $\phi_{E_T^{miss}}$ variable is sensible to very small effects in the detector, but the difference could be reduced by a factor of 10.

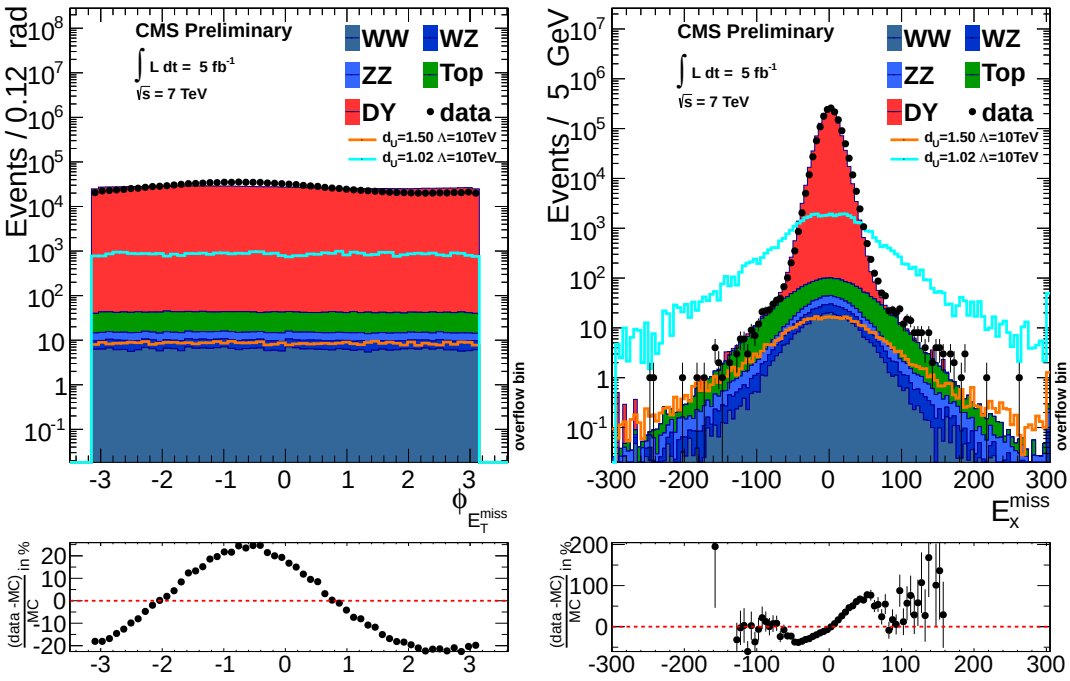

Figure 4.11.: The left plot shows the ϕ distribution of E_T^{miss} and the right distribution shows an offset between data and MC for the x component of E_T^{miss}.

These studies show that the E_T^{miss} is a well understood object in CMS one can correct for various understood effects in the detector.

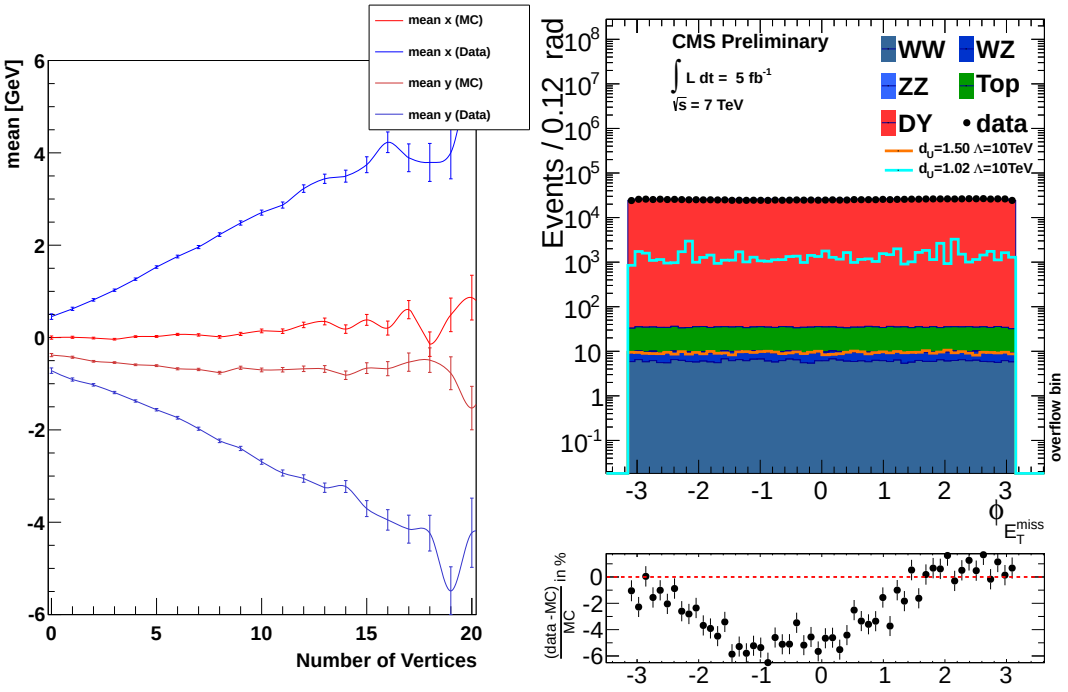

Figure 4.12.: The mean of the x and y component of $E_{\mathrm{T}}^{\mathrm{miss}}$ is plotted in the left against the number of vertices. The corrected $E_{\mathrm{T}}^{\mathrm{miss}}$-$\phi$ in the right shows less disagreement between data and MC.

5. Object Selection

The object and event selection were chosen to minimise the contribution to $E_{\mathrm{T}}^{\mathrm{miss}}$ from mis-measurements in the detector, and consequently have a good signal to background separation for reconstructed objects. Each event must pass general filters such as beam halo filter and HBHE noise filter ([66] for a full list), before it is selected. Events must have at least one good reconstructed vertex. A vertex is considered good, if it has at least four tracks and is less than 24 cm from the beam spot in z direction.

5.1. Muons

The aim of this analysis is to select muons in the mid energy range from Z boson decay. The main discriminant between Z events, and Unparticle plus Z events, will be the missing energy. A tight muon selection is applied on both muons from the Z decay to ensure a proper measurement.

To be above the trigger threshold of 30 GeV, one muon must have a $p_T > 32$ GeV (for details

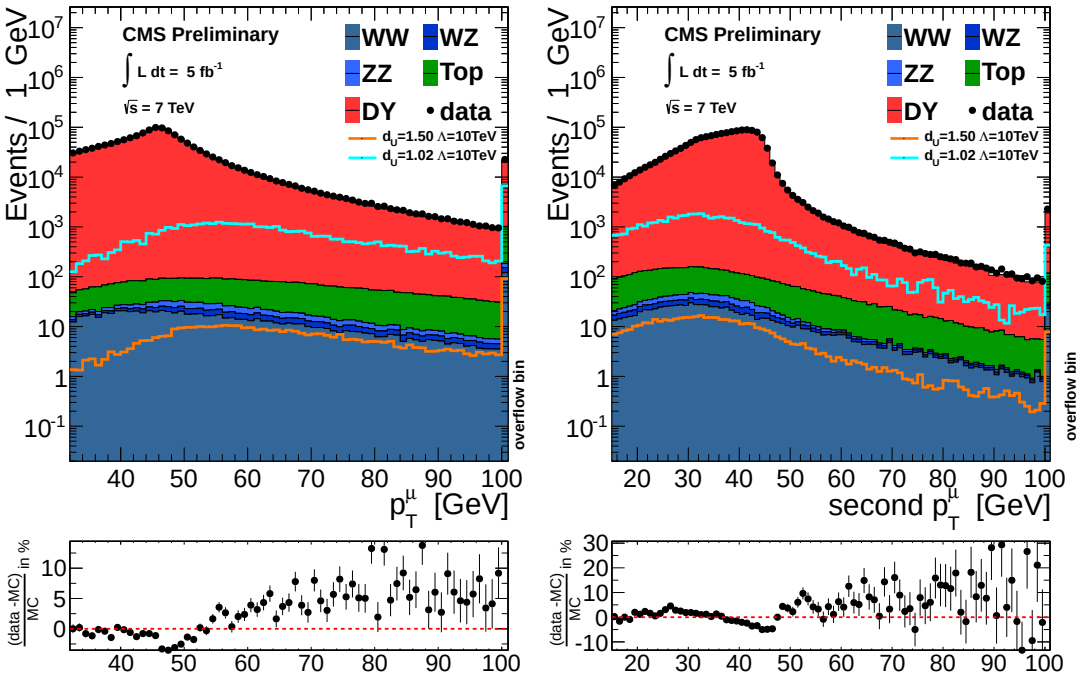

Figure 5.1.: The muon p_T spectrum for the leading muon (left) and the second leading muon (right). Both plots show the different background processes stacked and the data points plotted on top. For these plots only the muon selections are applied. In the plot below the difference in statistical standard deviations σ is plotted.

see Fig 5.1). The second muon must have at least a $p_T > 17\,\text{GeV}$. The muons have to be reconstructed as global- and tracker-muons in an η range of $|\eta| < 2.1$. The global-tracks have to satisfy certain track quality cuts recommended by the tight muon ID [67]:

- There have to be more than **10 hits in the tracker**. This cut ensures that the muon track is sufficiently well measured in the tracker.
- At least **one hit** has to be in the **pixel detector**. This is important for the tracking algorithm and ensures the reduction of cosmic muons or muons from secondary vertices e.g. muons from b-decays . The fist hit in the tracker is the largest influence for the vertex calculation of the track.
- At least **two muon chambers** must be matched to the muon. The muon chambers are the key instruments in the muon identification. Only muons reach the outer part of the detector. The relatively big distance from the interaction point ensures a good p_T resolution.
- The $\chi^2/\mathbf{N_{dof}}$ of the track fit has to be **smaller than 11**. This reduces the number of tracks that are not well fitted.

A relative tracker-isolation of less than 0.1 is required for both muons. Relative tracker-isolation means, that in a ΔR cone of 0.3 the sum of the track p_T, which do not belong to the muon, must have less than 10% of the muon's p_T:

$$(\sum_{\Delta R<0.3} p_T)/p_T^{\mu} < 0.1 \tag{5.1}$$

To reduce events from cosmic muons, the minimal distance of the track in the x-y plane to the primary vertex (d_0), has to be smaller than 0.2 cm. The primary vertex of an event is defined as the vertex with the highest $\sum p_T$ of the associated tracks. The cosine of the solid angle between two muons has to be bigger than 0.02. Since this analysis uses pf$E_{\text{T}}^{\text{miss}}$ and pfJets the muon ID is influenced by the particle flow algorithm. The pf-muons rely on the global-muon reconstruction, therefore the muon momenta used for the $E_{\text{T}}^{\text{miss}}$ calculation are the same as the used muon momenta. The pfJets however are clustered from all reconstructed particles and only afterwards the reconstructed pf-muons and pfElectrons are excluded from the pfJets. In addition to this a minimal jet p_T of 50 GeV and a jet ID is required, which reduces jets dominated by single objects. This can still result in a double counting of muons which do not fulfil the pf-muon ID, hence the muons would be counted as jets and as muons. In order to avoid this one can either clean the muon collection for pfJets, or clean the pfJet collection for muons. At first the second is the more obvious solution, but from the physics point of view, the muons that are near or in a jet are mainly non prompt muons from hadron decays. In Drell-Yan and signal events jets and muons should be spatially separated. To avoid events with the described problems a minimal distance ΔR is required between the muon and the nearest jet of $\Delta R > 0.5$. The $\Delta R(\mu, jet)$ distribution for every muon is shown in Figure 5.2. There are several details one has to note. The pf-muon ID uses a isolation cone of $\Delta R = 0.4$, since the pfJets are cleaned for pf-muons. This means that muons with a ΔR smaller than 0.4 most likely do not pass the pf-muon ID. The main part of the muons have a $\Delta R > 1$ and are well separated from pfJets. Muons from events with no jets are not shown in the plot. The slight disagreement between data and MC in the region around $\Delta R = 0.5$ can be due to the low QCD statistics.

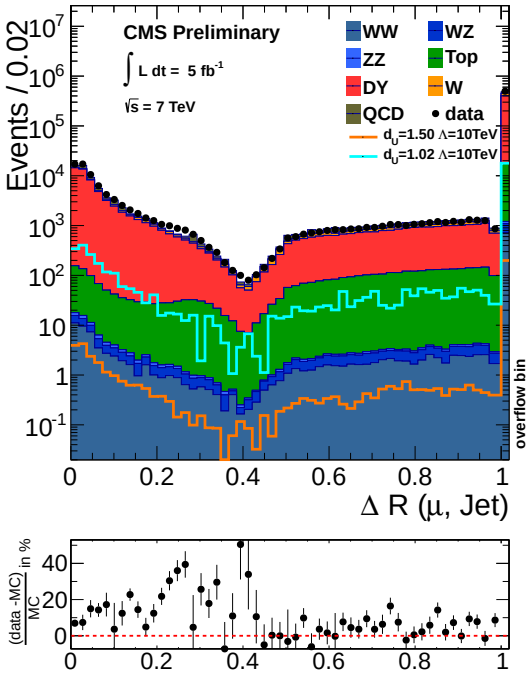

Figure 5.2.: ΔR between pfJets and muons for all muons that pass all cuts except the ΔR cut.

To see the effectiveness of the different cuts the muon selection can be viewed for each cut individually. To have a better comparison the cuts applied in Figure 5.3 are the complete muon ID except the viewed cut. The muon ID should not reduce the number of muons from processes like Drell-Yan, but muons from decays like QCD events. One can clearly see that most of the muons found in the data do not satisfy the minimal p_T criteria. To interpret this one has to keep in mind that all muons in an event are taken into account for this plot. Hence there are low energetic muons in the event that are possibly not from the hard interaction. One can see that the p_T cut filters most of the non DY-backgrounds from the data. Other cuts that show a difference between data and simulation are cuts on the isolation, the ΔR cuts and the track quality cuts. These cuts also reduce the DY-background the, but all these cuts clearly reduce the non DY backgrounds in the data and the efficiency loss is less than 1% for each of these cuts.

5.2. Electrons

Electrons are used to reject background with more than two muons (e.g. WZ) and in the $e/\mu - Method$ see Section 7.2. Electrons reconstructed with gaussian sum filter (gsf-electron) are used and a standard cut based ID is applied with the veto and the loose working point selection [68]. A relative combined particle flow isolation with ρ correction is requiered to be less than 0.15:

$$pfIso_{rel} = (pfIso_{Charged} + (pfIso_{Neutral} + pfIso_{Photon}) - \rho A_{eff})/E_T. \tag{5.2}$$

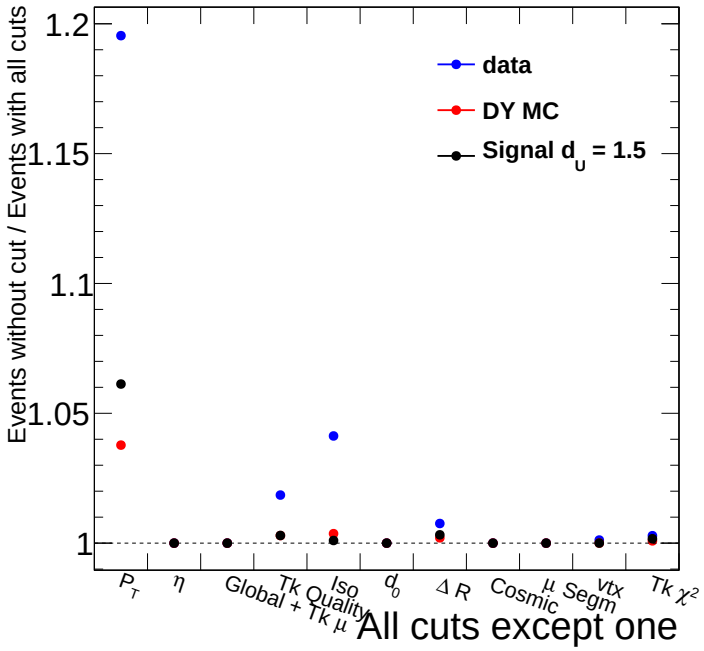

Figure 5.3.: The relative cut effectiveness for the muon ID, for all cuts except the shown. The number is relative to the muons that pass all muon ID criteria.

Electrons must have $E_T > 20\,\text{GeV}$ and at most one missing hit in the first pixel layer. The other cuts are different for electrons in the ECAL barrel ($|\eta| < 1.44$) and in the ECAL endcaps ($1.566 < |\eta| < 2.5$). The region between ECAL barrel and endcaps is not as well instrumented and therefore excluded. The cuts are listed in Table 5.1.

Table 5.1.: *Electron ID cuts in the ECAL barrel and endcaps*

cut value	barrel veto	endcap veto	barrel lose	endcap lose
$\Delta\phi_{i\eta}$	< 0.8	< 0.7	<0.15	< 0.1
$\Delta\eta_{i\eta}$	<0.007	<0.01	<0.007	<0.009
H/E	<0.15	-	<0.12	<0.1
d_0 [cm]	<0.04	<0.04	<0.02	<0.02
$\lvert 1/E - 1/p \rvert$	-	-	<0.05	<0.05
$\sigma_{i\eta i\eta}$	<0.01	<0.03	<0.01	< 0.03
$pfIso_{rel}$	<0.15	<0.15	<0.15	<0.15

5.3. Particle Flow Jets

Although jets are not directly part of the signature, they have an influence on $E_{\text{T}}^{\text{miss}}$ (see Section 4.5 and 7.3). Jets are also used to distinguish between signal and background. Jets are identified as objects clustered by the anti-k_T algorithm with the Particle Flow method

[69]. As requirements for jets we use the loose pfJet ID with:

- $p_T > 30\,\text{GeV}$
- $|\eta| < 3$
- neutral hadron fraction < 0.99
- neutral EM fraction < 0.99
- muon fraction < 0.9
- at least 2 constituents

The jets were cleaned for pf-muons and pfElectrons.

5.4. b-Tag

The contribution of backgrounds from top production is reduced by b-tagging. The track counting high efficiency algorithm (TCHE) is used to tag b-jets. The medium working point is chosen, which is optimised, to have a light-quark (u,d,c) mis-tag efficiency of less than 1%. Because of the p_T dependency pfJets are considered that pass our selection and have a $p_T > 50\,\text{GeV}$ and a discriminator greater than 3.3 as b-tagged (see Fig 7.2).

6. Data and Simulation

This is a search for Unparticles in the Z+$E_{\mathrm{T}}^{\mathrm{miss}}$, the signal and background processes have to be studied in detail. Within CMS the approach of Monte Carlo based simulation has a huge success in describing the involved physics. For example the model unspecific search MUSiC [70] has tested the Standard Model simulation in numerous distributions. In the following the used datasets and simulation will be discussed.

6.1. Data Handling and Reconstruction

To analyse the data from the CMS detector a software framework and a data structure is needed. For this purpose the CMSSW framework was developed. Within the CMSSW framework the generation of MC-events is handled as well as the reconstruction. To store the information necessary to reconstruct the Event Data Model (EDM) is implemented as a `C++` class. This event centred class allows to store the necessary information of an event in different stages of the reconstruction. The reconstruction chain is as follows:

- Only for MC-events:
  - Generation of events (GEN) with an integrated Generator e.g. Pythia 6/8 [71, 72]or from LHE-files
  - Simulation of the detector (SIM) using GEANT4 [73] to simulate the detector response for all particles passing through the detector
  - Digitalisation (DIGI) simulating the response of the electronics in the detector
  - Simulation of the low level trigger (L1)
- For MC- and data-events:
  - converting the detector response in to a computer readable format (DIGI2RAW), including some rudimentary object reconstruction
  - flagging the interesting events with the high level trigger (HLT)
  - Reconstruction of complex physical events (RECO)

Corresponding to the different reconstruction steps different data types are saved. To be able to reconstruct the recorded data with a future software the RAW data is stored. The RECO data format contains all information from the reconstruction step. To reduce the amount of data stored per event a data format AOD has been introduced, which contains mostly high level physics objects needed for the analysis.
In order to reduce the amount of data even further the AOD content is skimmed into flat ROOT [74] n-tuples, that can be stored locally and contain all analysis specific information. To create the flat n-tuple the ACSusyAnalysis [75] program was used. The framework was extended for the purposes of the present analysis. Key elements used in this analysis have been added by the author. The analysis code was also written by the author.

6.2. The 2011 Dataset

As input the data from proton proton collisions is used, with a centre-of-mass energy of 7 TeV recorded between March and October 2011, corresponding to an integrated luminosity of $4.98\,\mathrm{fb}^{-1}$. The used data has been certified by the CMS collaboration. The criteria was that all available detector components were working properly. All data was reconstructed with `CMSSW_4_2_X`.
The used datasets are listed in Table 6.1. For the muon channel the dimuon dataset is used, for the e/μ-method (see section 7.2) the electron muon dataset. As triggers the lowest unprescaled single muon triggers with isolation were used to collect the events. For the e/μ-method the electron muon trigger was used. A detailed list can be seen in Table 6.1.

Dataset	Trigger	Run Range	L(fb^{-1})
/DoubleMu/Run2011A-May10ReReco-v1/AOD	HLT_IsoMu17	160404-163869	0.2
/DoubleMu/Run2011A-PromptReco-v4/AOD	HLT_IsoMu20	165088-167913	0.9
/DoubleMu/Run2011A-05Aug2011-v1/AOD	HLT_IsoMu20	170249-172619	0.4
/DoubleMu/Run2011A-PromptReco-v6/AOD	HLT_IsoMu30	172620-173692	0.7
/DoubleMu/Run2011B-PromptReco-v1/AOD	HLT_IsoMu30	176697-180252	2.5
/MuEG/Run2011A-May10ReReco-v1/AOD	HLT_Mu8_Ele17_CaloIdT_CaloIsoVL || HLT_Mu17_Ele8_CaloIdT_CaloIsoVL	160404-163869	0.2
/MuEG/Run2011A-PromptReco-v4/AOD	HLT_Mu8_Ele17_CaloIdT_CaloIsoVL || HLT_Mu17_Ele8_CaloIdT_CaloIsoVL	165088-167913	0.9
/MuEG/Run2011A-05Aug2011-v1/AOD	HLT_Mu8_Ele17_CaloIdT_CaloIsoVL || HLT_Mu17_Ele8_CaloIdT_CaloIsoVL	170249-172619	0.4
/MuEG/Run2011A-PromptReco-v6/AOD	HLT_Mu8_Ele17_CaloIdT_CaloIsoVL || HLT_Mu17_Ele8_CaloIdT_CaloIsoVL	172620-173692	0.7
/MuEG/Run2011B-PromptReco-v1/AOD	HLT_Mu8_Ele17_CaloIdT_CaloIsoVL || HLT_Mu17_Ele8_CaloIdT_CaloIsoVL	176697-180252	2.5

Table 6.1.: *List of the datasets used in the analysis and the corresponding run ranges.*

6.3. Signal Monte Carlo Samples

To produce the signal samples PYTHIA 8.145 [72] was used, which implements the Unparticle model in LO [76][18]. As described in Section 2.4 the assumed process is $f\bar{f} \to UZ$, with a scalar Unparticle U. With these constraints there are three free model parameters left. The Unparticle dimension d_U, the Unparticle renormalisation scale Λ_U and the coupling strength λ. As mentioned before $|\lambda|^2$ would only scale the cross section, therefore it is set to 1. For the cross section given in equation 2.67 the Λ_U dependence can be reduced to:

$$\frac{d^2\sigma}{dP_U^2 dt} = \frac{|\bar{M}|^2}{16\pi s^2} \frac{A_{d_U}|\lambda|^2}{2\pi\Lambda_U^2} \left(\frac{P_U^2}{\Lambda_U^2}\right)^{d_U-2} \sim \Lambda_U^{2-2d_U}. \tag{6.1}$$

Hence only d_U influences the topology. For the signal generation d_U is varied between 1 and 2 as described in Section 2.4. The points can be seen in Table 6.2. The implemented model has no flavour changing neutral currents that would increase the cross section due to initial states with different flavours.
Comparing the Unparticle signal with the Drell-Yan Process on generator level, as shown in Figure 6.1, several observations can be made. The interference from Z/γ is not implemented

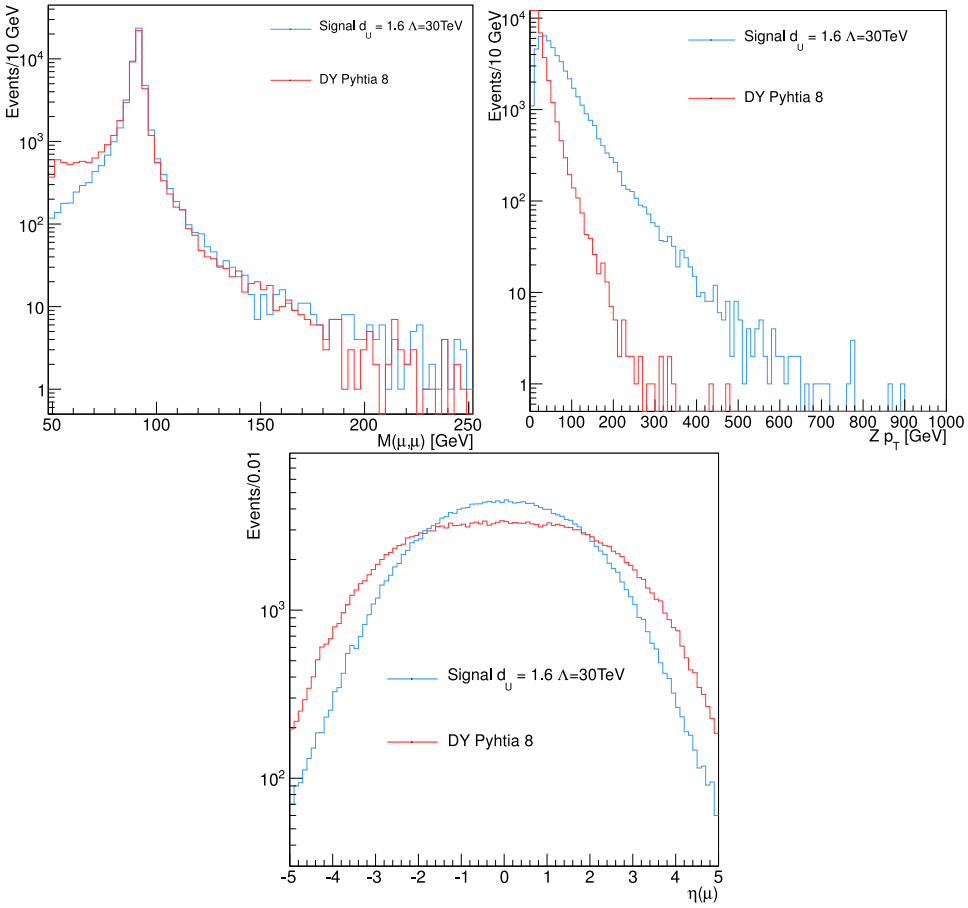

Figure 6.1.: The comparison between Drell-Yan and associated Unparticle production in $M_{\mu\mu}$, Zp_T and η on generator level.

in the signal. In the signal the Z has a higher p_T and respectively the muons from the Z decay have a smaller $|\eta|$ than the muons from the Drell-Yan process.

As stated in equation 6.1 for a given d_U the dependence on Λ_U is a factor $\Lambda_U^{2-2d_U}$, and does not depend on the process kinematics, like the Unparticle momentum P_U, or $\hat{s}$. One has to notice here, that in the limit $d_U \to 1$ the cross section is independent of Λ_U. The cross sections as a function of d_U and Λ_U are shown in Figure 6.2. For small d_U a large Λ_U corresponds to the same cross section as for a higher d_U.

The effect of different parameter points on the $E_{\mathrm{T}}^{\mathrm{miss}}$ on generator level is different for d_U and Λ_U. Generator $E_{\mathrm{T}}^{\mathrm{miss}}$ (Gen-$E_{\mathrm{T}}^{\mathrm{miss}}$) is defined as the missing transverse energy calculated from the generated particles that would be detected in an experiment. One can see a clear difference in the Gen-$E_{\mathrm{T}}^{\mathrm{miss}}$ distribution for different d_U points see Figure 6.3, where smaller values of d_U result in a steeply falling $E_{\mathrm{T}}^{\mathrm{miss}}$ distribution. The effect of different Λ_U values can not be observed in the Gen-$E_{\mathrm{T}}^{\mathrm{miss}}$ distribution, as is expected. The cross section dependency on d_U is plotted in Figure 6.2 with a fixed value for $\Lambda_U = 10TeV$ shows a constantly falling cross section for values above $d_U = 1.1$. The rising cross section in the region from $d_U = 1.0$ to 1.1 is due to the dimensional normalisation A_{d_U}, which is 0 for $d_U = 1$. The limit of $d_U = 1$ would correspond to a massless particle.

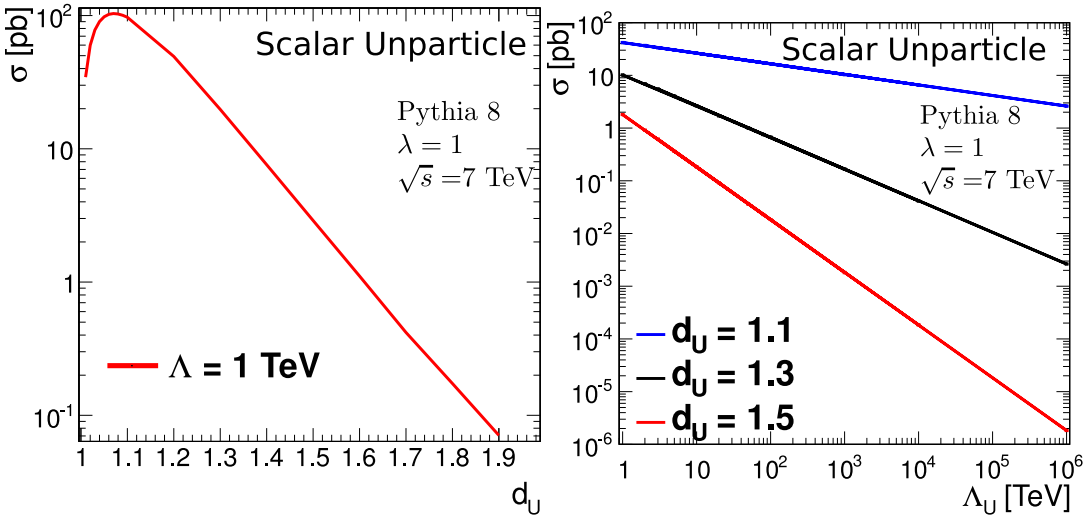

Figure 6.2.: Different model points with their cross section dependency. In the left for the same Λ_U different d_U were assumed, for the right plot different Λ_U values for three values of d_U are plotted.

As is motivated in Chapter 2.4 the Unparticle could have a small mass gap. This gap would have an impact on the $E_{\mathrm{T}}^{\mathrm{miss}}$ distribution in the low Gen-$E_{\mathrm{T}}^{\mathrm{miss}}$ region as seen in Figure 6.4. The high Gen-$E_{\mathrm{T}}^{\mathrm{miss}}$ region, e.g. above 100 GeV, will not be affected by a small gap. To avoid any systematic influence from a mass gap the signal samples are not produced with a mass gap.

6.4. Signal Simulation in CMSSW

The PYTHIA 8 event generator is used with the standard CMS configuration. It can be tuned to describe different collider configurations and energies. The tune used for this simulation was optimised for the LHC and is called Tune 4C [77]. It modifies the standard parameters for multiple interactions, hadronisation and the used PDF set. As PDF set the CMS standard CTEQ6L [78] is used.
The mimimal invariant mass of the Z is set to 20 GeV
All simulated events have been passed through a full detector simulation based on GEANT4 [73].
The used parameter points can be found in Table 6.2.
The variation of d_U changes the shape of the $E_{\mathrm{T}}^{\mathrm{miss}}$ distribution as can be see in Figure 6.3. The signal was produced with a Z decaying to two muons.

6.5. Background Monte Carlo Samples

The main challenge for this analysis is to describe $E_{\mathrm{T}}^{\mathrm{miss}}$ well. There are two types of Standard Model physics processes with this event signature, events with real $E_{\mathrm{T}}^{\mathrm{miss}}$ due to neutrinos that leave the detector, e.g. leptonic $t\bar{t}$ decays or $ZZ \to 2l2\nu$, and processes with no neutrinos, but $E_{\mathrm{T}}^{\mathrm{miss}}$ as a result of detector effects, e.g. Drell-Yan production.
Different MC generators were tested and found that MADGRAPH [79] describes the important values like jet multiplicities or $E_{\mathrm{T}}^{\mathrm{miss}}$ well and a sufficient number of events were

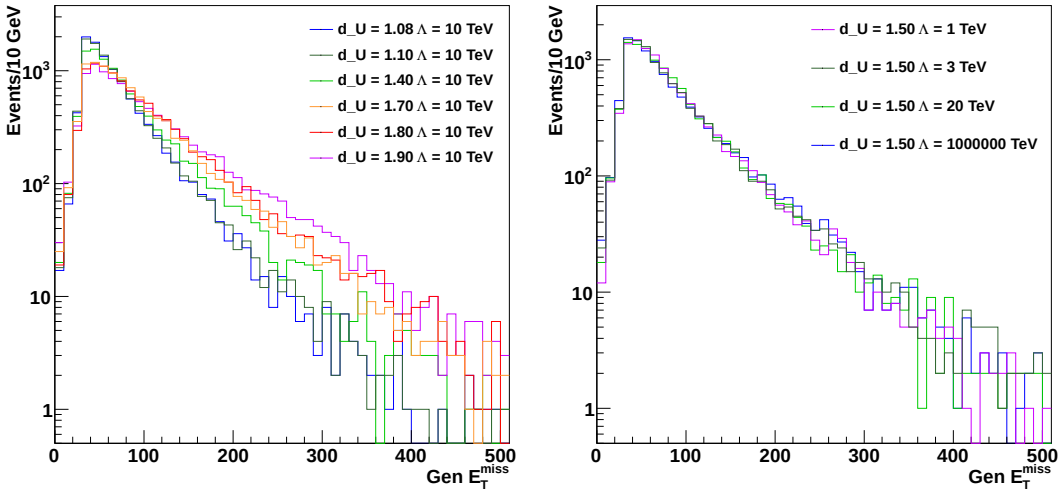

Figure 6.3.: Different model points with their $E_{\mathrm{T}}^{\mathrm{miss}}$ distribution. In the left for the same Λ_U different d_U were assumed, in the right different Λ_U for the same d_U. In the plots are shown the generated number of events without a normalisation factor.

simulated.
The Standard Model background at low $E_{\mathrm{T}}^{\mathrm{miss}}$ is dominated by the Drell-Yan (DY) process. At high $E_{\mathrm{T}}^{\mathrm{miss}}$ diboson events and $t\bar{t}$ are dominant.
For hadronisation PYTHIA 6 [71] was used with the Z2 tune [80] for all samples. The background predictions for diboson and single top were normalised using next-to-leading order calculations (NLO) in QCD [81]. NNLO cross sections were used for Drell-Yan [82], and NNLL for $t\bar{t}$ [83].

6.6. Efficiencies

The majority of searches for physics beyond the Standard Model at particle colliders are based on event rates. These depend on the ability to trigger and reconstruct particles with an understood efficiency. Statistically an efficiency is a ratio of two observables. In the context of particle physics the observable is in most cases the number of events. A good approximation for efficiencies is the interpretation as binomial distributed, even if this ansatz was shown to have some disadvantages.

6.6.1. Tag and Probe

Object efficiencies can be derived from simulation by comparing the number of generated events with the number of events passing a certain cut. This method however is highly dependent on the quality of the simulation. To derive the correct efficiency for particle objects processes like $Z \to \mu\mu$ can be used to measure the efficiency in data. These processes must have muon pairs in the final states. The idea of the "tag and probe" technique is that one of the muons is used as tag, with a high quality requirement, and the second is used as probe, where a certain quality requirement is tested. The result is an efficiency for this specific

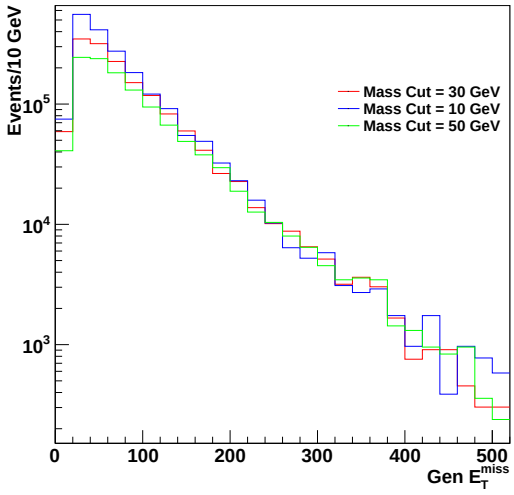

Figure 6.4.: Different minimal masses can have an effect on the shape of the $E_{\mathrm{T}}^{\mathrm{miss}}$ distribution. In the plot is shown the generated number of events without a normalisation factor.

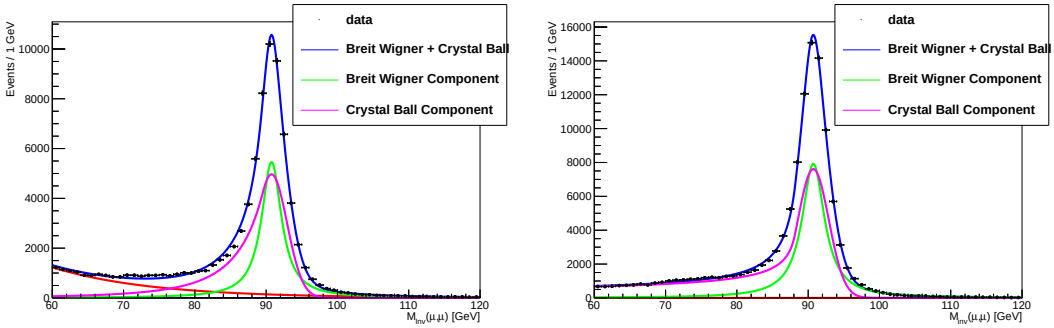

Figure 6.5.: The invariant mass for the trigger tag and probe with a probe p_T range of 25-35 GeV is shown for the failed events in the left, for the passed events in the right.

quality requirement.
The usual approach is to define an efficiency as:

$$\epsilon = \frac{N(\text{objects that satisfy a criteria and a basic selection})}{N(\text{objects that satisfy a basic selection})} \tag{6.2}$$

With the assumption that some efficiencies like trigger and particle identification (ID) are not correlated it is possible to construct an object efficiency by factorising.
The total muon efficiency can be decomposed into five different efficiencies:

$$\epsilon_{total} = \epsilon_{Track} \times \epsilon_{RECO} \times \epsilon_{ID} \times \epsilon_{iso} \times \epsilon_{Trigger} \tag{6.3}$$

Where ϵ_{Track} is the efficiency to seed and fit a track and ϵ_{RECO} corresponds to the reconstruction efficiency of a muon. ϵ_{ID} is the muon identification efficiency, ϵ_{iso} describes the isolation requirement efficiency and $\epsilon_{Trigger}$ the trigger efficiency. To select Z events an invariant mass

d_U	Number of events	σ [pb]
d_U =1.01	50k	13
d_U =1.02	47k	22
d_U =1.04	50k	30
d_U =1.06	50k	32
d_U =1.09	46k	32
d_U =1.10	50k	26
d_U =1.20	49k	9.4
d_U =1.30	50k	2.6
d_U =1.40	50k	0.7
d_U =1.50	44k	0.18
d_U =1.60	50k	0.048
d_U =1.70	50k	0.013
d_U =1.80	50k	$3.4 \cdot 10^{-3}$
d_U =1.90	50k	$0.094 \cdot 10^{-3}$

Table 6.2.: *Samples produced for scalar Unparticles with* $\Lambda_U = 10\,\text{TeV}$.

window for both muon candidates has to be between 60 GeV and 120 GeV. For each object an invariant mass distribution is filled. Depending on the object properties and the probe criteria it can either be in the passed distribution, or in the failed distribution. The benefit of this procedure is the possibility to subtract the background like W events from the distribution. To achieve this, the sum of three functions are fitted to the distribution. A Breit-Wigner-function, which models the Z-peak, a Crystal-Ball function, which is defined discrete with a Gaussian and a power-law as shown in equation 6.4, and models the resolution as well as the radiation components. The third function is an exponential to describe the background.

$$f_{CB}(x, \bar{x}, \sigma, \alpha, n) = N \cdot \begin{cases} \exp(-\frac{(x-\bar{x})^2}{2\sigma^2}), & \text{for } \frac{x-\bar{x}}{\sigma} > -\alpha \\ A \cdot (B - \frac{x-\bar{x}}{\sigma})^{-n}, & \text{for } \frac{x-\bar{x}}{\sigma} \leqslant -\alpha \end{cases} \tag{6.4}$$

with

$$A = \left(\frac{n}{|\alpha|}\right)^n \cdot \exp\left(-\frac{|\alpha|^2}{2}\right)$$

$$B = \frac{n}{|\alpha|} - |\alpha|$$

The integral of the Crystal-Ball and Breit-Wigner-functions is taken to be the background free number of Z events. The importance of the background subtraction can be seen in Figure 6.5. In the context of this analysis the isolation efficiency and the trigger efficiencies have been calculated. The RECO efficiencies, track fitting efficiencies and ID efficiencies were taken from the official CMS muon group. The official results are in Table 6.4.

The criteria for tags have to be very strong in order to guarantee a well measured event and to reduce background. The probe criteria have to be a subset of this tag criteria. In this context the tag has to fulfil all the ID selection cuts, matched to the used trigger and a cut on $p_T > 20\,\text{GeV}$. For the probe the same constraints are applied, except the value under investigation. The obtained result can be plotted as a function of different quantities, such as

Process	kinematic cuts	σ in pb	order of σ	number of events	Generator	PDF set
$Z \to ll$	$M_{ll} > 50\,\text{GeV}$	$3.05 \cdot 10^3$	NNLO	31M	Madgraph	CTEQ6L
$WW \to 2l2\nu$		4.5	NLO	1.2M	Madgraph	CTEQ6L
$ZZ \to 2\mu 2\nu$		0.18	NLO	0.5M	Powheg	CTEQ6L
$WZ \to 3l1\nu$	$M_{ll} > 50\,\text{GeV}$	0.64	NLO	1.2M	Madgraph	CTEQ6L
$t\bar{t} \to 2l2b$		17.3	NNLL	10M	Powheg	CTEQ6M
$W \to l\nu$		$31.3 \cdot 10^3$	NLO	58M	Madgraph	CTEQ6L
QCD mu enriched	$50\,\text{GeV} < \hat{p_T}^a < 80\,\text{GeV}$	$6.4 \cdot 10^6$	LO	10M	Pythia 6	CTEQ6L
QCD mu enriched	$80\,\text{GeV} < \hat{p_T} < 120\,\text{GeV}$	$0.8 \cdot 10^6$	LO	8.2M	Pythia 6	CTEQ6L
QCD mu enriched	$120\,\text{GeV} < \hat{p_T} < 150\,\text{GeV}$	$93 \cdot 10^3$	LO	7.9M	Pythia 6	CTEQ6L
QCD mu enriched	$\hat{p_T} > 150\,\text{GeV}$	$47 \cdot 10^3$	LO	3.8M	Pythia 6	CTEQ6L
$t \to bl\nu$ (s-Channel)		3.19	NLO	0.26M	Powheg	CTEQ6M
$t \to bl\nu$ (t-Channel)		41.92	NLO	3.9M	Powheg	CTEQ6M
$t \to bl\nu$ (tW-Channel)		7.87	NLO	0.7M	Powheg	CTEQ6M
$\bar{t} \to bl\nu$ (s-Channel)		1.44	NLO	0.14M	Powheg	CTEQ6M
$\bar{t} \to bl\nu$ (t-Channel)		22.65	NLO	1.9M	Powheg	CTEQ6M
$\bar{t} \to bl\nu$ (tw-Channel)		7.87	NLO	0.73M	Powheg	CTEQ6M
$gg \to H \to (ZZ \to 2\mu 2\nu$		$5.4 \cdot 10^{-3}$	NNLO	10k	Powheg	CTEQ6M
VBF[b] $\to H \to (ZZ \to 2\mu 2\nu$		$0.43 \cdot 10^{-3}$	NNLO	47k	Powheg	CTEQ6M

Table 6.3.: *List of the used MC processes with the generator cuts and the cross section.*

[a] $\hat{p_T}$ is defined as $\sum_{\textit{all gen. particles}} p_T$ for all particles from the hard process.

[b] vector boson fusion

2011A			
	ϵ_{data}	ϵ_{MC}	$\epsilon_{data}/\epsilon_{MC}$
$\lvert\eta\rvert < 1.2$	96.12±0.04	96.66±0.04	99.44±0.06
$1.2 < \lvert\eta\rvert < 2.4$	95.78±0.06	96.22±0.06	99.54±0.09
2011B			
	ϵ_{data}	ϵ_{MC}	$\epsilon_{data}/\epsilon_{MC}$
$\lvert\eta\rvert < 1.2$	95.65±0.03	96.98±0.04	98.64±0.06
$1.2 < \lvert\eta\rvert < 2.4$	92.10±0.06	95.92±0.09	96.01±0.11

Table 6.4.: *Official Tag and Probe results from the CMS muon group for 2011 for* $\epsilon_{Track} \times \epsilon_{RECO} \times \epsilon_{ID}$ *taken from [84]. The errors are statistical only and all values are in %.*

p_T of the probe muon or the number of vertices. In Figure 6.6 the trigger efficiency vs the p_T

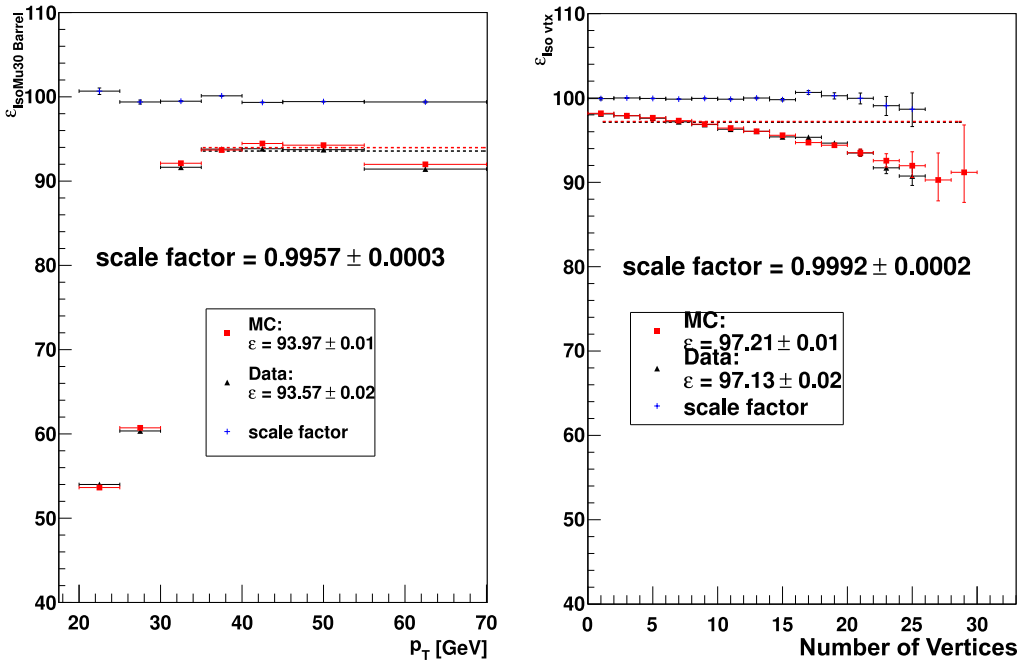

Figure 6.6.: The tag and probe efficiencies for the Trigger (left) and the muon isolation (right).

and the isolation requirement efficiency vs the number of vertices can be seen. For the trigger one can see that the turn on curve is very sharp and simulation and data agree within 0.5%. The isolation obviously is dependent on the number of vertices and therefore on the pile up in the event. Nevertheless is the behaviour of the data very well simulated, meaning that data and MC agree in the shapes of p_T, η or the number of vertices. The average efficiencies obtained from data are:

$$\epsilon_{trigger} = 93.1 \pm 0.02\% \qquad \epsilon_{iso} = 97.0 \pm 0.02\% \tag{6.5}$$

The main difference between data and MC therefore comes from $\epsilon_{Track} \times \epsilon_{RECO} \times \epsilon_{ID}$. The simulation is corrected for this efficiency. The total muon efficiency is 86.4% in data. For two muons to be reconstructed correctly this implies an efficiency of:

$$\epsilon_{2\mu} = (\epsilon_{Track} \times \epsilon_{RECO} \times \epsilon_{ID} \times \epsilon_{iso})^2 (2\epsilon_{trigger} - \epsilon^2_{trigger}) = 85.7\% \tag{6.6}$$

6.7. Pile Up

As described in Section 3.1 before, in the data are multiple interactions per bunch crossing. The interactions aside from the hard interaction are called up interactions. The definition of pile up can be widened to describe two kinds of secondary interaction. The first is the interaction of one or more protons in the same bunch-crossing, which is called in time pile up. The second is called out-of-time pile up and describes the effect of the brunch-crossing before and after the hard interaction on the detector[1]. This pile up description has to be taken into account in the simulation of MC-events. The number of secondary interactions

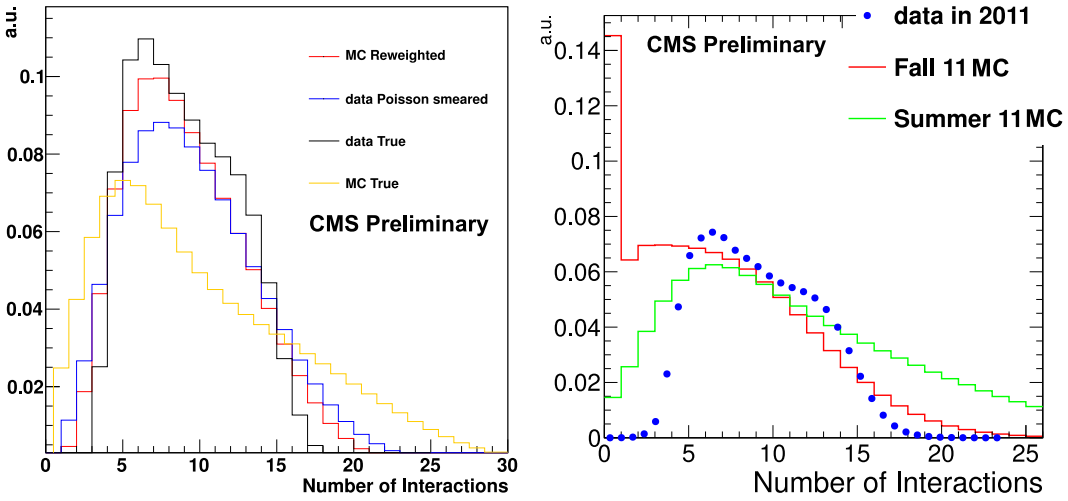

Figure 6.7.: The MC and data distributions for true (not smeared) number of interactions and smeared/reweighted are shown in the left. In the right plot number of in time interactions for data and the two pileup scenarios Summer 11 and Fall 11 are plotted. All histograms have been normalised to unity.

is dependent on the instantaneous luminosity. The main physics process in these additional interactions are soft-QCD events, which means QCD mediated events with a low $\hat{s}$. Because the instantaneous luminosity distribution for the taken data is unknown at the time of the simulation, the generated samples must be adjusted after the data is recorded.
To generate the samples the generation is split into two groups: On the one hand the soft-QCD events are generated in so called Minimum Bias samples. On the other hand the hard processes are produced. These two generator outputs have to be mixed before the reconstruction, to ensure a behaviour of the detector as expected in data. As input for the generation a distribution of the number of interactions is needed. This number of interactions

[1]The out of time pile up effects the event, because of potential overlapping signals in the calorimeters.

is used to get a correlated number of interactions for in and out-of-time pile up. In the Summer 11 production campaign a flat distribution is used with a slowly falling tail, see Figure 6.7. One of the features of this distribution is that by dicing the correlated number of interactions for in- and out-of-time pile up according to a Poisson distribution the number of events with no pile up interaction is increased drastically. By comparing the Summer 11 distribution to the expected number of interaction distribution in data, one can see that due to this feature the main part of the MC does not describe the data. This is improved in the Fall 11 production campaign, where the input distribution (see Figure 6.7) is much closer on the number of interactions as observed in the 2011 data. To adjust the simulated

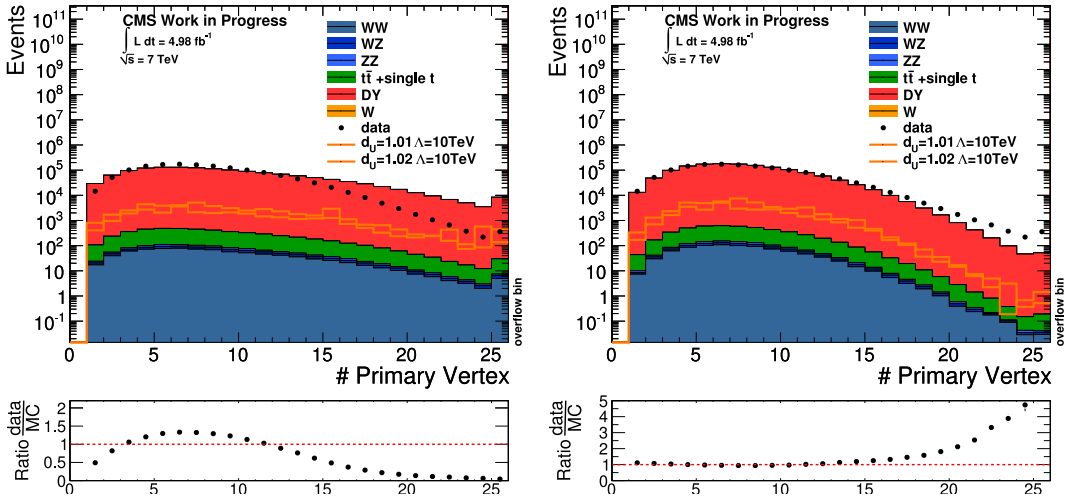

Figure 6.8.: In the plots is shown the vertex distribution before (left) and after (right) the reweighting. The reweighting of the MC can reproduce the data vertex distribution up to 20 vertices.

MC-samples to the recorded data, the simulation is reweighted. To get the correct weight factor, the distribution used to generate the MC-samples is taken, and the number of expected events is calculated for the data (true number of interactions in data), by using the Minimum Bias cross section and the instantaneous luminosity per used run. For each combination of pile up before, during and after the event the possibility is calculated for all bins of the true distribution. These three dimensional weight histograms for data and MC are divided to get a 3D-weight for each in- and out-of-time pile up combination. As can be seen in Figure 6.7 the reweighting reproduces the distribution of the Poisson smeared number of interactions in data.
A measure for the in-time pile up is the number of vertices in an event. The value itself can only be seen as an estimate, because the vertex reconstruction efficiency is different in data and MC. As can be seen in Figure 6.8, the events with a high number of vertices are not reconstructed as efficient in MC as they are reconstructed in data. The majority of the used events has less than 20 vertices and is well described by the pile up reweighting.

7. Analysis

To reduce non-Z backgrounds, a Z boson candidate is selected by requiring two muons that both pass all the selection criteria and have opposite electric charge and have a invariant mass close to the nominal Z mass (see Figure 7.1). The Z candidate and $E_{\mathrm{T}}^{\mathrm{miss}}$ have to be back to back in the transverse plane. To reduce the systematic uncertainties due to mismeasured jets, and enhance the signal, events with less than two jets are selected. The contribution of $t\bar{t}$ is reduced further by rejecting events with a b-tagged jet. The final discriminant between signal and background is $E_{\mathrm{T}}^{\mathrm{miss}}$.

7.1. Event Selection

The invariant mass window is chosen to be $|M_{\mu\mu} - M_Z| < 20\,\mathrm{GeV}$. This reduces the backgrounds without Z resonance, such as $t\bar{t}$, single top, WW and W+jets. The two muons must have the opposite electric charge (OS), and events with a third muon or an additional electron are rejected.

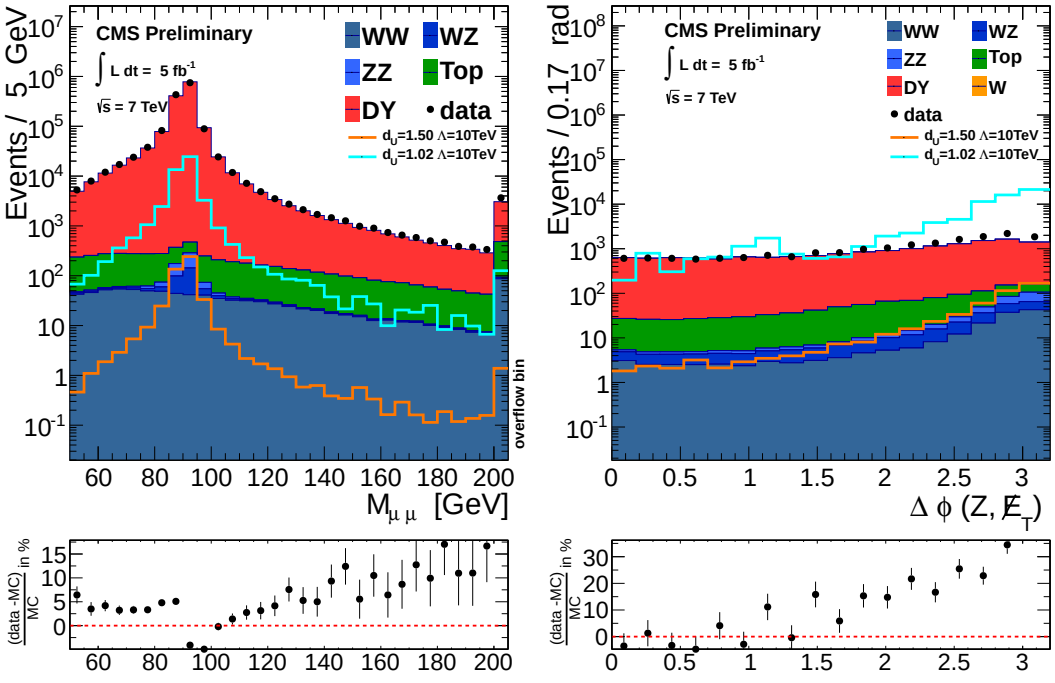

Figure 7.1.: In the left distribution the invariant mass of two selected muons is shown. After the cut on $M_{\mu\mu}$ and $E_{\mathrm{T}}^{\mathrm{miss}} > 40\,\mathrm{GeV}$ the $\Delta\phi(Z, E_{\mathrm{T}}^{\mathrm{miss}})$ distribution can be seen at the right.

In Figure 7.1 (right) one can see that the angle between Unparticles and Z in the transverse

plane has a peak at π. In $t\bar{t}$ the $\Delta\phi(Z, E_{\mathrm{T}}^{\mathrm{miss}})$ distribution is more or less flat . Therefore only events with $\Delta\phi(Z, E_{\mathrm{T}}^{\mathrm{miss}}) \geq 2$ are selected.
In the high $E_{\mathrm{T}}^{\mathrm{miss}}$-region $t\bar{t}$ is the dominating background. In order to reduce the influence even further only events with no b-tagged jet are taken into account (see Figure 7.2). The contribution from single top events is considered too, but estimated to be small. In the shown plots they are merged with the $t\bar{t}$ background.

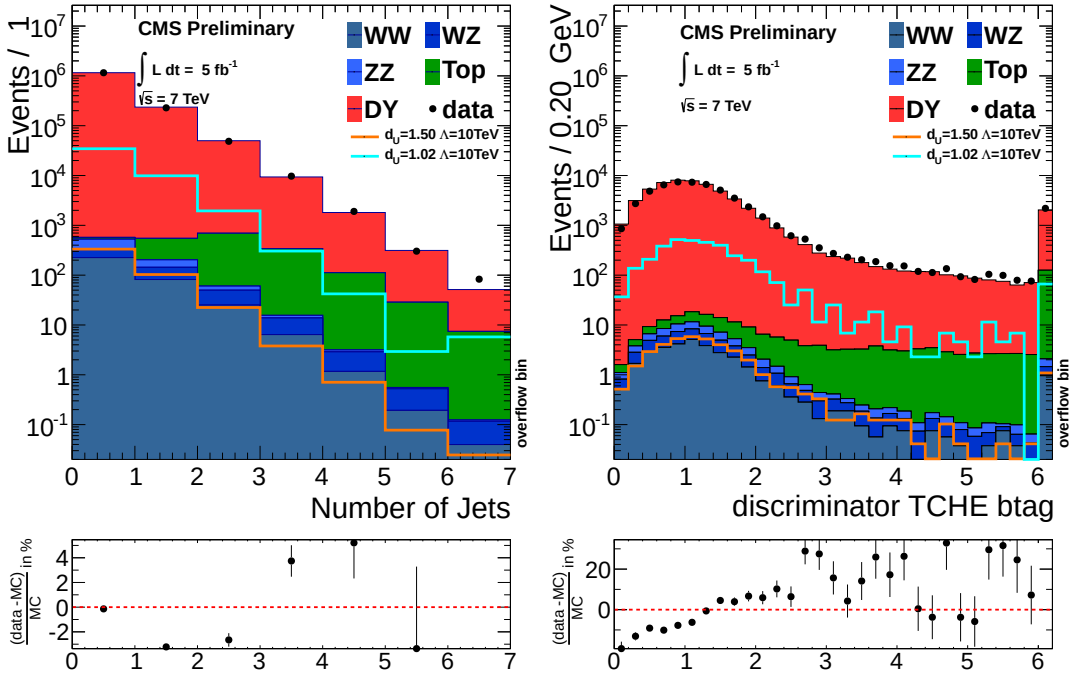

Figure 7.2.: In the left plot it is shown that the signal has a peak at lower jet multiplicities, whereas the $t\bar{t}$ background has more than one jet in most events.

Since the Drell-Yan process has no $E_{\mathrm{T}}^{\mathrm{miss}}$ from the hard interaction, the observed $E_{\mathrm{T}}^{\mathrm{miss}}$ is due to detector effects. This results in a peak at low $E_{\mathrm{T}}^{\mathrm{miss}}$ in the $E_{\mathrm{T}}^{\mathrm{miss}}$ distribution and is different from the other backgrounds. One of the challenges for the Drell-Yan process is the correct modelling of the additional jets in the event, which influence the $E_{\mathrm{T}}^{\mathrm{miss}}$ distribution. To test this the jet multiplicity cut has been inverted (see Figure 7.3). A better data and MC agreement to higher $E_{\mathrm{T}}^{\mathrm{miss}}$ is observed and the signal is suppressed , but the Drell-Yan distribution is wider.
The contribution from Standard Model double boson events can be divided into two parts: non reducible ZZ and reducible WZ and WW. The $ZZ \rightarrow 2l2\nu$ has exactly the event signature of Unparticles except for the shape of the $E_{\mathrm{T}}^{\mathrm{miss}}$ distribution. For a detailed analysis of the $ZZ \rightarrow 2l2\nu$ channel see [85]. The $WW \rightarrow 2l2\nu$ background is reduced by the invariant mass and the $\Delta\phi$ cut and can be estimated by data-driven methods (see section 7.2). The WZ background has only high $E_{\mathrm{T}}^{\mathrm{miss}}$ and two leptons with an invariant mass near the Z mass, if the WZ decays into 3 leptons and one neutrino. With the veto on a third muon or electron in the event this background is reduced.
The $t\bar{t}$ background is dominant at high $E_{\mathrm{T}}^{\mathrm{miss}}$ (see Figure 7.4 and Table 7.1). Because of the different event topology $t\bar{t}$ events can be separated from signal events as is done with the $\Delta\phi(Z, E_{\mathrm{T}}^{\mathrm{miss}})$ and N_{jet} requirements.

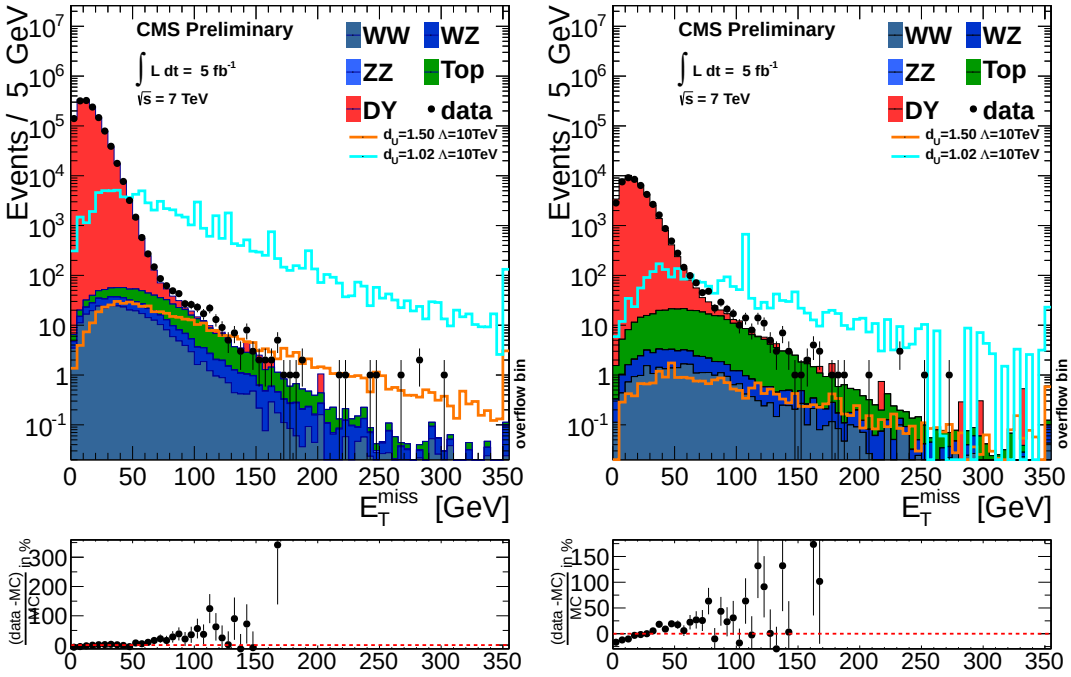

Figure 7.3.: In the left is the $E_{\mathrm{T}}^{\mathrm{miss}}$ distribution with less than 2 jets. In the right distribution at least two jets are required in the events. The comparison shows that the Drell-Yan distribution is broader, $t\bar{t}$ contribution is enhanced and the signal is reduced.

The final $E_{\mathrm{T}}^{\mathrm{miss}} > 100\,\mathrm{GeV}$ cut was optimised on the best expected limit using all the systematic uncertainties from section 7.3.
Since there have been a discovery of a Higgs like particle [86], the possible contribution from such a Higgs via $H \to ZZ \to 2\mu 2\nu$ is investigated. In Figure 7.5 the Higgs contributions from vector boson fusion (VBF) and gluon-gluon fusion are plotted for a Higgs mass of 125 GeV. In the plot only $|M_{\mu\mu} - M_Z| < 20\,\mathrm{GeV}$ is required, and the Higgs has a contribution of less than 0.01 events above 100 GeV. One can conclude that a 125 GeV Higgs has no influence on this search.

7.2. Data-Driven Background and Validation

In the past the simulation of the Standard Model has become a very reliable source for the expected background events. The simulation of the detector seems to be understood in remarkable detail in this short time of data taking at the LHC. There are some processes however, that are not easy to describe with simulation. There are three reasons for this. Firstly processes with high cross section like QCD events would require an enormous number of generated events to give an accurate representation of the data. Secondly some processes like $t\bar{t}$ are sill subject of active research and are not known in the degree of detail as the rest of the Standard Model and finally searches are often performed in the tails of distributions, which are not easy to generate with sufficient statistics. Therefore it is a useful mechanism to validate the simulation with data-driven methods. The aim of these methods is either to

Table 7.1.: Standard Model prediction from simulation for different cuts. Uncertainties are statistical. The numbers of events observed in the data are also given.

	2 OS μ	$\lvert M_{\mu\mu} - M_Z \rvert < 20\,\text{GeV}$	$N_{jet} < 2$	$\Delta\phi(Z, E_\text{T}^\text{miss}) \geq 2$	No b-Jet	$E_\text{T}^\text{miss} > 100\,\text{GeV}$
WW	889 ± 4.7	326 ± 2.8	298 ± 2.7	237 ± 2.4	237 ± 2.4	6.60 ± 0.4
WZ	223 ± 0.9	192 ± 0.8	160 ± 0.7	116 ± 0.6	116 ± 0.6	12.2 ± 0.2
ZZ	280 ± 0.8	260 ± 0.8	250 ± 0.8	214 ± 0.8	214 ± 0.8	29 ± 0.3
Top	$4.90\text{k} \pm 17.5$	$1.76\text{k} \pm 11$	716 ± 10	491 ± 8.7	421 ± 8.6	28.2 ± 0.9
DY	$1.46\text{M} \pm 0.9\text{k}$	$1.40\text{M} \pm 0.9\text{k}$	$1.35\text{M} \pm 0.9\text{k}$	$597\text{k} \pm 580$	$595\text{k} \pm 580$	9.0 ± 2.3
Total bgrd.	$1.47\text{M} \pm 0.9\text{k}$	$1.4\text{M} \pm 0.9\text{k}$	$1.35\text{M} \pm 0.9\text{k}$	$598\text{k} \pm 580$	$596\text{k} \pm 580$	85 ± 2.5
Data	1.47M	1.39M	1.34M	620k	618k	89

Table 7.2.: *Signal efficiency for different cuts with respect to the generated events decaying to 2 μ in %.*

	2 OS μ	$\lvert M_{\mu\mu} - M_Z \rvert < 20\,\text{GeV}$	$N_{jet} < 2$	$\Delta\phi(Z, E_\text{T}^\text{miss}) \geq 2$	No b-Jet	$E_\text{T}^\text{miss} > 100\,\text{GeV}$
d_U =1.01	45 ± 0.2	43 ± 0.2	41 ± 0.2	38 ± 0.2	38 ± 0.2	6.6 ± 0.1
d_U =1.02	45 ± 0.2	43 ± 0.2	41 ± 0.2	38 ± 0.2	38 ± 0.2	6.7 ± 0.1
d_U =1.04	45 ± 0.2	43 ± 0.2	41 ± 0.2	38 ± 0.2	37 ± 0.2	6.7 ± 0.1
d_U =1.06	45 ± 0.2	43 ± 0.2	41 ± 0.2	37 ± 0.2	37 ± 0.2	6.7 ± 0.1
d_U =1.09	45 ± 0.2	43 ± 0.2	41 ± 0.2	38 ± 0.2	38 ± 0.2	6.9 ± 0.1
d_U =1.10	46 ± 0.2	44 ± 0.2	42 ± 0.2	38 ± 0.2	38 ± 0.2	6.7 ± 0.1
d_U =1.20	46 ± 0.2	44 ± 0.2	42 ± 0.2	38 ± 0.2	38 ± 0.2	7.8 ± 0.1
d_U =1.30	41 ± 0.2	39 ± 0.2	37 ± 0.2	34 ± 0.2	34 ± 0.2	7.5 ± 0.1
d_U =1.40	47 ± 0.2	45 ± 0.2	43 ± 0.2	40 ± 0.2	39 ± 0.2	9.0 ± 0.1
d_U =1.50	53 ± 0.2	51 ± 0.2	48 ± 0.2	44 ± 0.2	44 ± 0.2	11.2 ± 0.1
d_U =1.60	49 ± 0.2	47 ± 0.2	44 ± 0.2	41 ± 0.2	41 ± 0.2	11.2 ± 0.1
d_U =1.70	49 ± 0.2	47 ± 0.2	44 ± 0.2	41 ± 0.2	41 ± 0.2	12.8 ± 0.2
d_U =1.80	50 ± 0.2	48 ± 0.2	45 ± 0.2	42 ± 0.2	42 ± 0.2	14.4 ± 0.2
d_U =1.90	51 ± 0.2	49 ± 0.2	45 ± 0.2	42 ± 0.2	42 ± 0.2	15.4 ± 0.2

crosscheck the simulation or to obtain certain backgrounds from the data. The critical point is to obtain a signal free region in the data and then predict the behavior in the signal region from this.

7.2.1. e/μ -Method

Two of the biggest uncertainties are the $t\bar{t}$ cross section and the b-tag efficiency to veto $t\bar{t}$ events. To reduce these uncertainties the e/μ-method is used to estimate the contribution of $t\bar{t}$,$t/\bar{t}$ and WW in the signal region from $e\mu$ events.
The idea behind the method is that the Standard Model W has equal branching ratios into all leptonic final states. Processes such as $WW \to 2l2\nu$, $t\bar{t} \to 2W2b \to 2l2\nu2b$ or $\bar{t}tW \to 2l1b$ behave physically the same for $\mu\mu$ and $e\mu$ and the signal has no $e\mu$ contribution. The E_T^miss distribution is therefore expected to have the same shape in both channels and twice the number of events in the $e\mu$-channel. However, one has to correct for the different electron and muon reconstruction and identification efficiencies, using a correction factor denoted

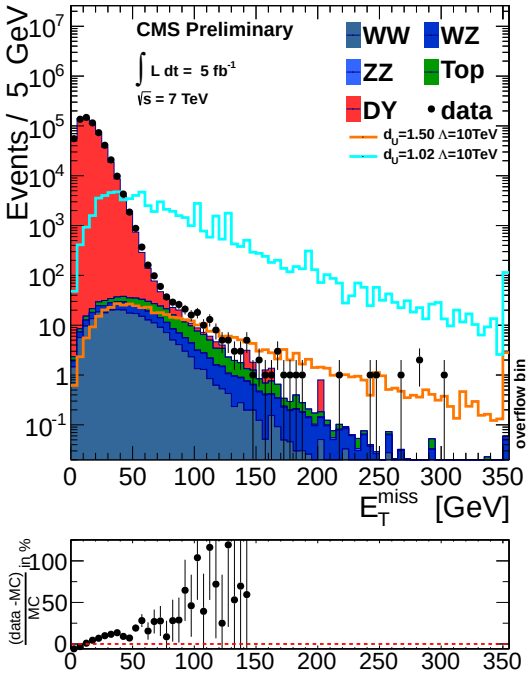

Figure 7.4.: The $E_{\mathrm{T}}^{\mathrm{miss}}$ after all signal selection cuts. One can see in the difference plot below, that the agreement between data and simulation is not perfect in the low $E_{\mathrm{T}}^{\mathrm{miss}}$ region up to 80 GeV, but as discussed in Section 7.4, the $E_{\mathrm{T}}^{\mathrm{miss}}$ has systematic uncertainties that can cover the difference in this region. At higher $E_{\mathrm{T}}^{\mathrm{miss}}$ the agreement between data and simulation is very good.

$R_{\mu\mu} = N_{\mu\mu}/N_{e\mu}$.
To gain a larger sample and because of the lower trigger threshold the p_T cuts for the muon ID is lowered to be above 17 GeV for the higher energetic muon and 15 GeV for the second. For the electron the loose ID is required.
The factor $R_{\mu\mu}$ is taken from a sideband in the invariant mass distributions with little Drell-Yan event contribution (110 GeV $< M_{\mu\mu} <$ 150 GeV). To further enhance number of $t\bar{t}$ events, one jet is required to be b-tagged (see Figure 7.6). This has no systematic influence, because the b-tagging efficiency is independent of the flavour of leptonic top decay.
The result is:

$$R_{\mu\mu} = \frac{390}{801} = 0.49 \pm 0.04(stat.).$$

As statistical error a binomial error is calculated. The invariant mass region was varied in a 5 GeV window for the lower and upper boundary. The standard deviation of the $R_{\mu\mu}$ mean is 0.03 and is considered as a systematic uncertainty. From simulation we expect the top and WW processes to behave similar in the Z mass region and in the sideband region, see Figure 7.7. To extract the top and WW events in the signal region (70 GeV $< M_{\mu\mu} <$ 110 GeV), we apply the signal event selection to all $e\mu$ events, and rescale the obtained distribution with the factor $R_{\mu\mu}$ (see Figure 7.6). There are 78 events in the $e\mu$-channel after the event selection. This number is assumed to be Poisson distributed and therefore an uncertainty of 8.8 events is

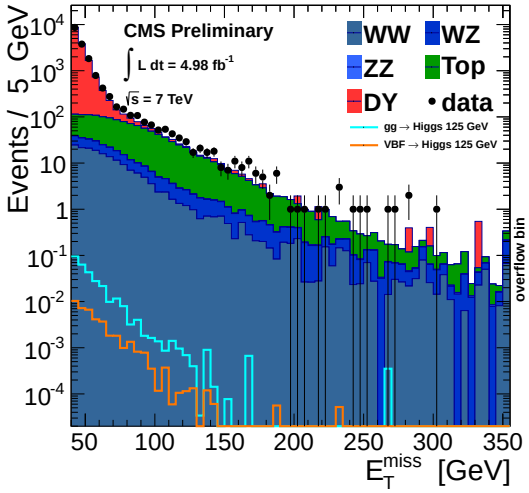

Figure 7.5.: The Higgs contribution from the $H \rightarrow (ZZ \rightarrow 2\mu 2\nu)$ channel has no significant effect on the signal.

used. But there are 0.5 ± 0.05 (stat.) events from WZ processes in the signal region, according to the simulation. This is a systematic deviation and therefore the used $N_{e\mu}$ is corrected for this influence. The contribution has been considered as a systematic error, but even a 100% uncertainty on the simulation prediction has less than 1% effect on the result of this method. The method predicts 37.7 ± 5.7 events from top and WW processes in the signal region. This agrees with expectation from the simulation of 28 ± 1.0 (stat) ± 3 (syst) events. The comparison between data and simulation is plotted in Figure 7.6(right) for the $e\mu$-channel and in Figure 7.7 (left) for the scaled $e\mu$ data with the $\mu\mu$ simulation.

7.2.2. Multijet and W-Boson Contribution

The contribution of QCD events is always a source of uncertainty. This signature is strongly reduced, after selecting two good muons in the selected Z mass region, because muons produced in QCD events are most likely not isolated, and even if they are, they would not have an invariant mass around the Z mass.
No simulated QCD event is observed after applying the muon selection and requiring $M_{\mu\mu} > 50\,\text{GeV}$. The uncertainty of one QCD event is therefore calculated from the scale factors to be about 350. The number of QCD events is increased by using events from data. The offline isolation and ΔR criteria of the muon selection are then inverted on data events. This provides a data sample of 32k non-isolated data events dominated by QCD events (see Figure 7.8). There are about 100 times more events in the data sample than the uncertainty from the simulation on the isolated events. On these data events all signal selection requirements are used and no event is left in the final distribution. This means that the QCD event contribution is negligible in the final selection.
One can calculate the worst case assumption that one non-isolated data event would have passed the signal selection, then the weight of the event can be calculated from the MC uncertainty of the events before the signal selection, which states that there should be a at least 100 times less events with isolated muons as there are non-isolated muon events. This

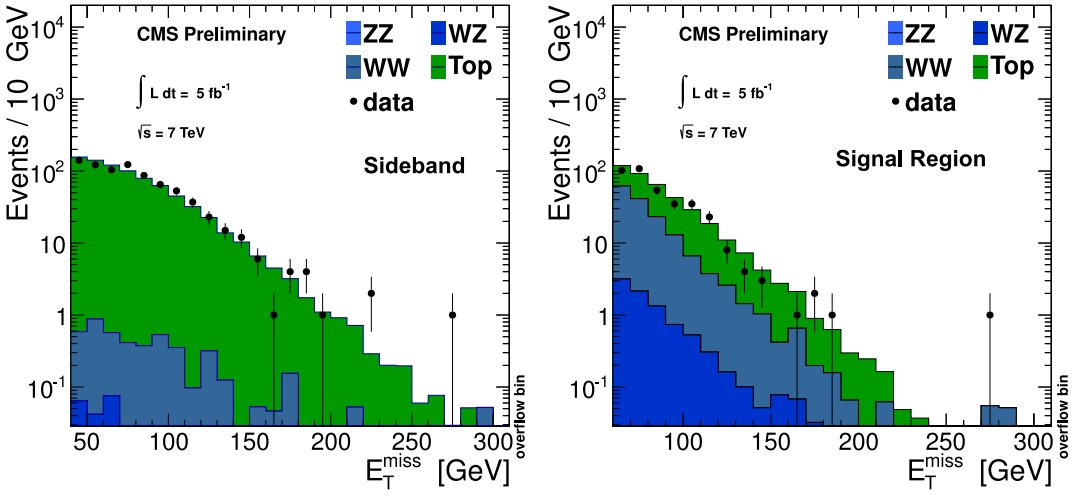

Figure 7.6.: The $e\mu$-channel in the sideband (110 GeV $< M_{\mu\mu} <$ 150 GeV) (left) and in the signal region (70 GeV $< M_{\mu\mu} <$ 110 GeV) (right).

would mean in in the worst case there are 0.01 events from multijet production in the final event selection.
The W+jets background has an event signature similar to the signal, if a lepton in a jet is reconstructed as isolated lepton. To test the W+jets contribution with data events a similar approach as with QCD events is used. On data events one of the selected two muons has to be not isolated. This provides a sample of 47k data events with $M_{\mu\mu} > 50$ GeV. From the simulation of the non isolated events we can conclude that only about half of the events are from W+jets. There are 69 W+jet events expected with two isolated muons from simulation with $M_{\mu\mu} > 50$ GeV. The ratio between isolated events and non isolated events is 1/300. After the signal selection 27 events with one non isolated muon are observed in data. By applying the scale factor for isolated to non isolated events the contribution of W+jet events after the signal selection is estimated to be less than 1% in the final selection. This effect is negligible.

7.2.3. Drell-Yan Contribution

An important background to this analysis is most certainly the DY production. As it has a high cross section, but no undetected particles, the low E_T^{miss} region is dominated by this background. The DY process has the same decay properties as the signal. The only difference is that the signal has more E_T^{miss}. One solution to this might be to fit a function to the DY dominated low E_T^{miss} region, and to evaluate this function in the high E_T^{miss} region. This ansatz for the background description has been chosen by various groups in different kinematic variables, e.g. the W' search [87]. As a possible cross check this has been tested, the result is in Figure 7.9. The function was chosen to be:

$$(x-a)^b \cdot (x-a)^{c\log(x-a)}. \tag{7.1}$$

The function is fitted in a E_T^{miss} region from 15 GeV to 60 GeV to the data, and is in very good agreement with the simulation in this region. For E_T^{miss} higher than 80 GeV the Monte

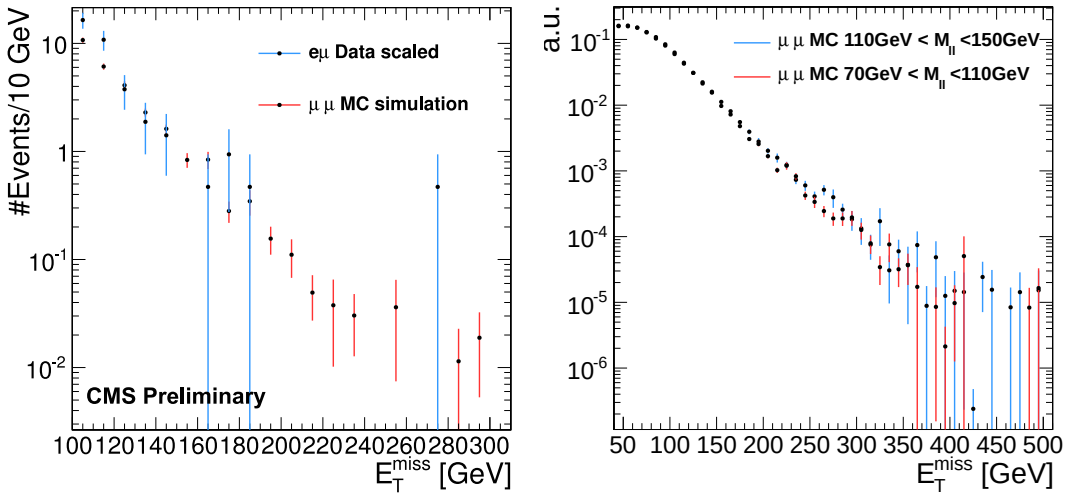

Figure 7.7.: The shape agreement between $\mu\mu$ simulation for top and WW processes and $e\mu$-data is good ($\chi^2/N_{Dof} = 0.66$) (left) and the MC prediction for top and WW for the Z mass and the sideband region (right) shows that the sideband can be used for the calculation of $R_{\mu\mu}$.

Carlo prediction and the fit begin to diverge and the fit is no good description of the DY background. The simulation predicts much more events with high E_T^{miss} than the fit. The DY events with high E_T^{miss} seem not to follow the same functional description as the low E_T^{miss} DY events. Therefore a correct description of the DY-E_T^{miss} distribution could only be achieved by fitting to higher E_T^{miss} values. Unfortunately the contribution from the signal and other backgrounds are too high in this region.
Therefore the Monte Carlo description for the DY background is chosen as this seems to describe the data in the best accessible way.
To get the best possible Monte Carlo description several generators are compared to data. In Figure 7.10 the E_T^{miss} distribution and the jet multiplicity are plotted for the Drell-Yan process. Three different generators were compared: MADGRAPH [79], POWHEG [88], and PYTHIA 8 [72]. In the E_T^{miss} distribution one can clearly see that for low E_T^{miss} MADGRAPH and POWHEG give the same prediction and have a good agreement with the data. For E_T^{miss} above 50 GeV other backgrounds than the Drell-Yan begin to dominate. One can see that for high E_T^{miss} MADGRAPH has the higher statistics. In the jet multiplicity plot 7.10 the best agreement between data and simulation is for the MADGRAPH generator. Therefore MADGRAPH is chosen to be the generator used for the Drell-Yan process.

7.2.4. ZZ Contribution

The contribution from ZZ events is irreducible, since if one Z decays in into two muons and the other Z decays into two neutrinos, the detector signature is not distinguishable from the signal signature. One possibility to access the kinematics, is to use 4 lepton events and subtract one of the Z candidates from the kinematic balance. In order to get an exact representation of the $ZZ \to 2\mu 2\nu$ events, but to increase the statistics the four lepton events were chosen to be either containing 4μ or $2\mu 2e$, where always the first muon pair that has a

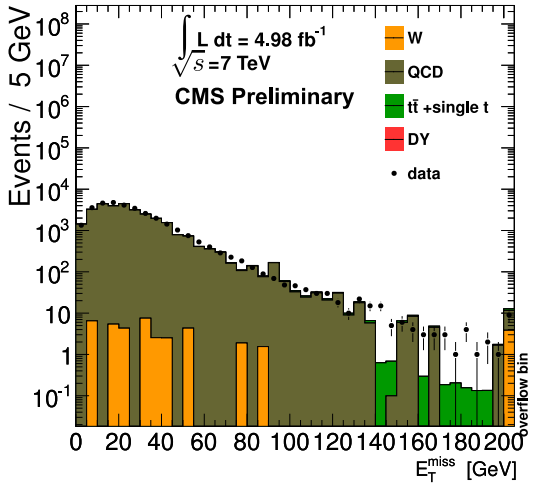

Figure 7.8.: By inverting the isolation of both muons a high statistics sample of QCD events can be obtained from data. From this sample no event is left after the analysis cuts. For this plot only muon selection is applied.

Z candidate in the required mass range was chosen to be the muons remaining in the event, the other two muons or electrons are subtracted from the $E_{\mathrm{T}}^{\mathrm{miss}}$. 20 events were found, that fulfil this requirement. But in order to draw conclusions from this number of events the difference between the three final states has to be considered. First of all the branching ratio from $Z \to \nu\nu$ is 20%, where the branching ratio of a Z decaying to electrons or muons is only 6.7% [89]. In case of the four muon events the final states of the two Z decays are not distinguishable, and therefore the branching ratio of $ZZ \to 2\mu 2e$ is twice the branching ratio of $ZZ \to 4\mu$. And the acceptance times reconstruction efficiency for two muons or electrons has to be taken into account. For two muons to be triggered reconstructed, isolated and in the right invariant mass region the efficiency can be seen in Figure 7.9 (right). The muon efficiency is about 55%. For electrons the efficiency has not been calculated in the context of this analysis, but as a rough estimate of 50% is sufficient enough for the following cross-check. In summary, the factor between $ZZ \to 2\mu 2\nu$ and $ZZ \to 4\mu$ or $2\mu 2e$ is:

$$R = \frac{BR(Z \to \nu\nu)}{BR(Z \to \mu\mu) \cdot \epsilon_{\mu}^{id} \cdot 0.5 + BR(Z \to ee) \cdot \epsilon_{e}^{id}} \approx 8 \tag{7.2}$$

This means events from $ZZ \to 2\mu 2e$ and $ZZ \to 4\mu$ have one-eighth less statistical power than the $ZZ \to 2\mu 2\nu$ process. Consequently this method is not effective to give a good description of $ZZ \to 2\mu 2\nu$ in the signal region. After the invariant mass cut the data estimate predicts 160 ± 36 (stat.) events, where the simulation predicts 260 ± 0.8 events.

7.3. Systematic Uncertainties

The systematic influences in the search can be separated into two groups. Object specific effects like muon reconstruction or resolution and global influences like PDF and cross section uncertainties.

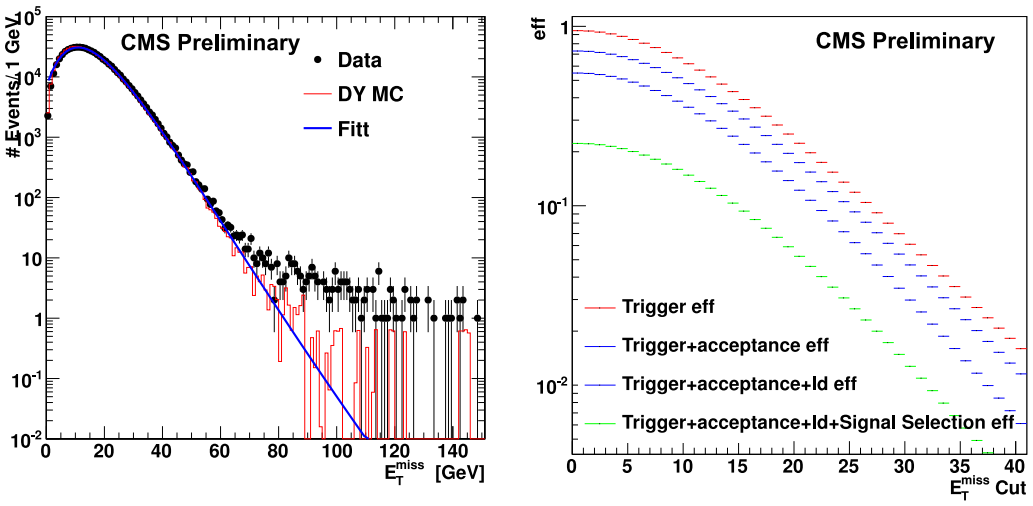

Figure 7.9.: The Drell-Yan $E_{\mathrm{T}}^{\mathrm{miss}}$ distribution can not be reproduced by a fit to data at low energies as shown left. All cuts except $E_{\mathrm{T}}^{\mathrm{miss}}$ are applied. The Drell-Yan MC efficiency for different selections is shown right.

7.3.1. Object Specific Uncertainties

Essentially all objects in the detector have an impact on the final result. This is due to the use of $E_{\mathrm{T}}^{\mathrm{miss}}$. To estimate the influence of $E_{\mathrm{T}}^{\mathrm{miss}}$ on the selection and the search region each object is shifted according to its uncertainties.

Two kinds of different uncertainties can be separated for measured objects. The first uncertainty is due to the energy scale of the object and the second is due to the resolution of an object. To investigate the impact of the scale uncertainty each component of the four-vector is shifted with the relative uncertainty of p_T, here called σ_{scale}:

$$p_{\alpha_{new}} = (1 \pm \sigma_{scale}) \cdot p_{\alpha}$$

where p_α is E, p_x, p_y, p_z. This is propagated to the $E_{\mathrm{T}}^{\mathrm{miss}}$ variable :

$$E_{\mathrm{x}}^{\mathrm{miss}} = E_{\mathrm{x}}^{\mathrm{miss}} \mp \sigma_{scale} \cdot p_x$$
$$E_{\mathrm{y}}^{\mathrm{miss}} = E_{\mathrm{y}}^{\mathrm{miss}} \mp \sigma_{scale} \cdot p_y$$

for each object.

To take additional uncertainties in the resolution into account the four-vector of each object is smeared with a gaussian by its systematic resolution uncertainty.

$$p_{\alpha_{new}} = gauss(p_\alpha, p_\alpha * \sigma_{res})$$

where $gauss(\mu, \sigma)$ is a random gaussian distribution with the mean μ and the standard-deviation σ. The difference is then propagated to $E_{\mathrm{T}}^{\mathrm{miss}}$ as before.

The corrected objects are then used as input for the analysis and the impact on the search region was derived. The following uncertainties are used:

- muon scale: 0.1% [43]

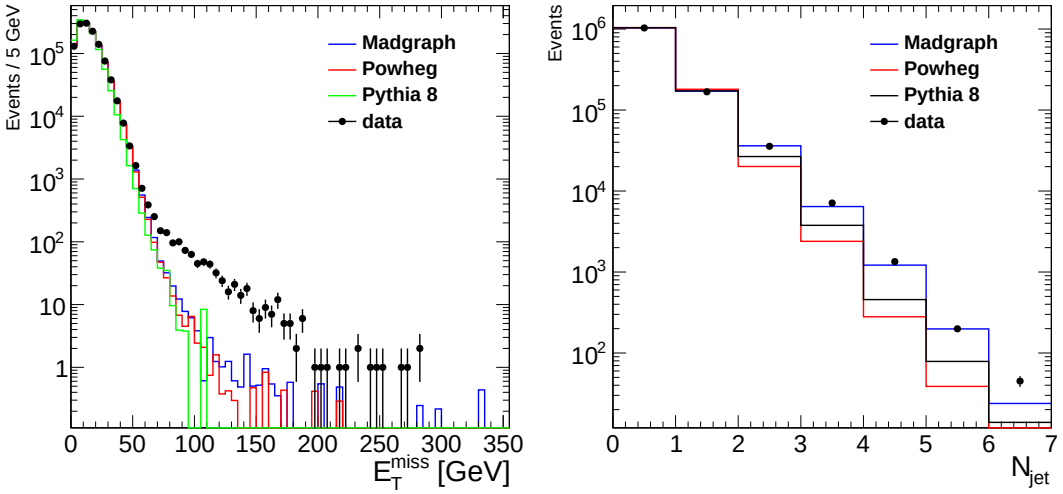

Figure 7.10.: The plots show the comparison between Monte Carlo simulation and data events. The simulated events were scaled to the data. The events have to have two muons with opposite charge and $|M_{\mu\mu} - M_Z| < 20\,\text{GeV}$.

- muon resolution: 0.5% [43]
- electron scale: 1.3% (barrel) 4.1% (endcap) [90]
- jet energy scale: η and p_T dependent uncertainty [55][1]
- jet resolution: η and p_T dependent uncertainty [55][2]

A summary of the systematic uncertainties is shown in Figure 7.11. For high $E_{\text{T}}^{\text{miss}}$ the Drell-Yan processes, which is the main source of the systematic uncertainties, has few simulated events. From these object specific uncertainties only jet related uncertainties seem to influence the number of events in the search region. The effect of muon or electron uncertainties on $E_{\text{T}}^{\text{miss}}$ is negligible. The jet energy resolution has the biggest influence on the search region (see Table 7.3). The jet related uncertainty changes dramatically if the $E_{\text{T}}^{\text{miss}}$ cut for the search region is lowered. The systematic uncertainties from jets rise to 60% for scale and resolution, see Figure 7.11. The sharp rise in the systematic uncertainties for lower $E_{\text{T}}^{\text{miss}}$ is due to the steeply falling $E_{\text{T}}^{\text{miss}}$ distribution, as was seen in Figure 7.4. These uncertainties were used to optimise the search region to the best expected limit. The uncertainty from the use of raw $E_{\text{T}}^{\text{miss}}$ instead of $E_{\text{T}}^{\text{miss}}$ corrected with the jet energy uncertainties is evaluated to have an effect of 8% on the background and 1% on the signal.
The signal has similar behaviour in all parameter points and is little effected by object specific influences.

7.3.2. Unclustered Energy

The unclustered energy is by definition not reconstructed as an object. The main source of unclustered energy in an event is pile up and should be equally distributed in the detector.

[1] A typical value for the jet energy scale is 3% uncertainty for a jet with p_T =30 GeV
[2] A typical value for the jet energy resolution is 5% uncertainty for a jet with p_T =50 GeV

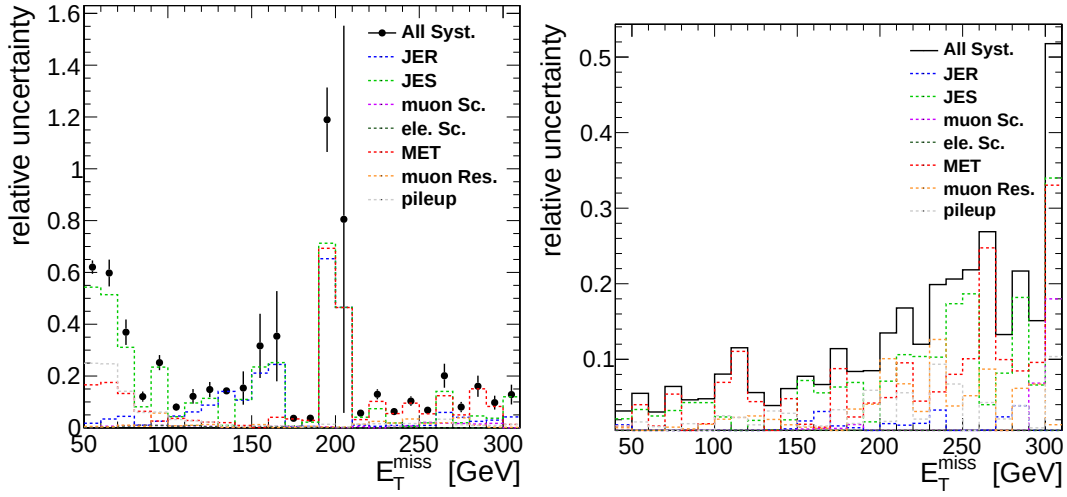

Figure 7.11.: The influences of the various systematic uncertainties depending on the E_T^{miss} distribution for the backgrounds used from simulation is shown in the left plot. The added systematic uncertainties show that for high E_T^{miss} the statistical significance of the simulation is low. This is due to missing Drell Yan statistics, which is the main source of the systematic uncertainties. A detailed discussion can be found in Section 7.4. For the signal with $d_U = 1.1$ the systematic uncertainties are shown in the right plot. The systematic uncertainties increase with higher E_T^{miss} values.

	Jet energy resolution	Jet energy scale	Muon	Electron	RAW E_T^{miss}
Background	4.5%	4.3%	$< 0.1\%$	$< 0.1\%$	8%
Signal	1%	1%	$< 0.1\%$	$< 0.1\%$	1%

Table 7.3.: *Influence of object specific uncertainties on the search region.*

Therefore unclustered energy directly influences the E_T^{miss} resolution and has to be investigated further.
The E_T^{miss} resolution is studied in the Drell-Yan decay. The channel has possible signal contributions, therefore the study is constrained to the low E_T^{miss} region (E_T^{miss} <60 GeV). In this region for each Unparticle event about 2k Drell-Yan are expected.

Because a $Z \to \mu\mu$ event has no real E_T^{miss}, the E_x^{miss} and E_y^{miss} distribution should be gaussian distributed and the standard deviation is a measure for the E_T^{miss} resolution (see Figure 7.12). The resolution of E_T^{miss} is dependent on the activity in an event and a measure for this is the scalar sum of all transverse momenta $\sum p_T$. The data therefore is divided into 10 GeV steps of the $\sum p_T$ and each subset is fitted in the E_x^{miss} and E_y^{miss} distribution (see Figure 7.13). Because of their orthogonality they can be considered as independent measurements and therefore as a cross-check if the detector is ϕ symmetric.
To implement the fit the RooFit package [91] is used with a E_x^{miss} and E_y^{miss} range from -50 GeV to 50 GeV, a mean between -5 GeV and 5 GeV and a standard deviation from 0 GeV to 50 GeV. The results can be seen in Figure 7.13.

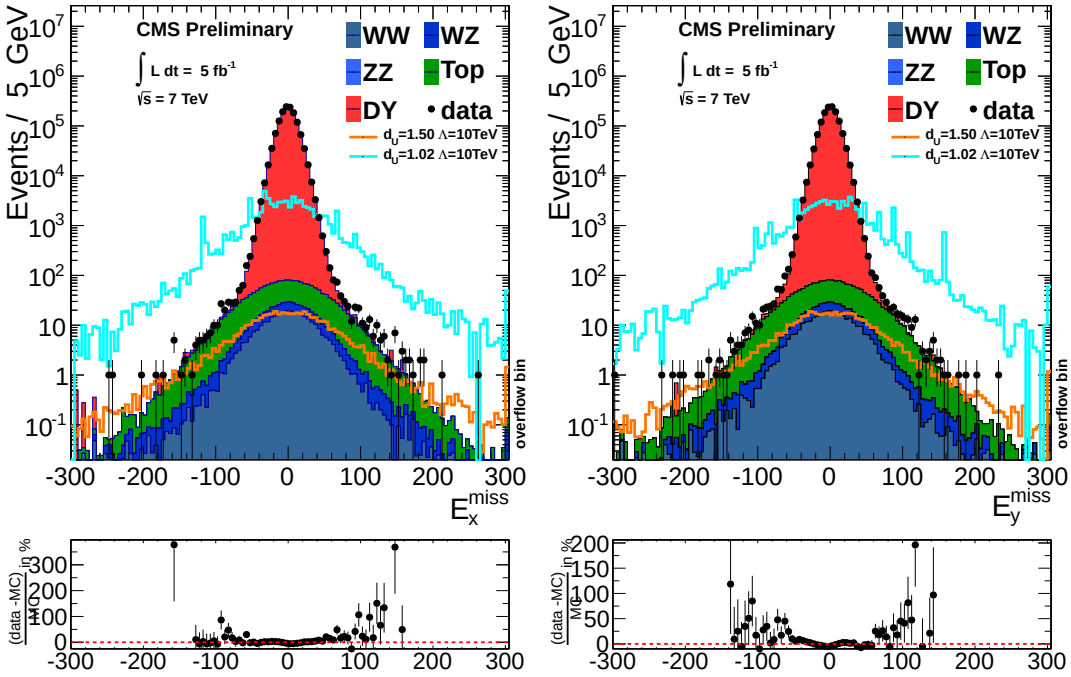

Figure 7.12.: The E_x^{miss} and E_y^{miss} distribution after requiring two muons in the invariant mass region of 20 GeV around the Z mass.

No difference between simulation and data is observed in the resolution of E_T^{miss} (see right Figure 7.13). Hence one can conclude that for each $\sum p_T$ bin the E_T^{miss} resolution is correctly modelled. But a difference in the $\sum p_T$ distribution as shown in Figure 7.14 is observed. Hence the E_T^{miss} resolution in the MC is not the same as in the data, because a too low $\sum p_T$ is assumed in the simulation. If it is assumed this difference is caused by pile up one can estimate the impact of the pile up on E_T^{miss} by quantifying the effect dependent on a pile up sensitive observable. The observable most sensitive to pile up is the number of reconstructed vertices. Therefore the $\sum p_T$ per vertex is plotted. To correct for the hard interaction the muons identified as Z are subtracted from the $\sum p_T$. A shift between simulation and data of 2.52 ± 0.01 GeV per vertex is observed. As the E_T^{miss} resolution depends on the $\sum p_T$ in an event, it is not correctly represented in the simulation. To model this effect the resolution function is fitted dependent on the $\sum p_T$.

$$f(\sum p_T) = A + B\sqrt{\sum p_T} + C\sum p_T$$

This is a expected behaviour of the E_T^{miss} resolution [92], and the parameters can be interpreted as:

- noise term (pile up) $\rightarrow$ A
- stochastic term (energy measurement) $\rightarrow$ B
- constant term (energy scale) $\rightarrow$ C

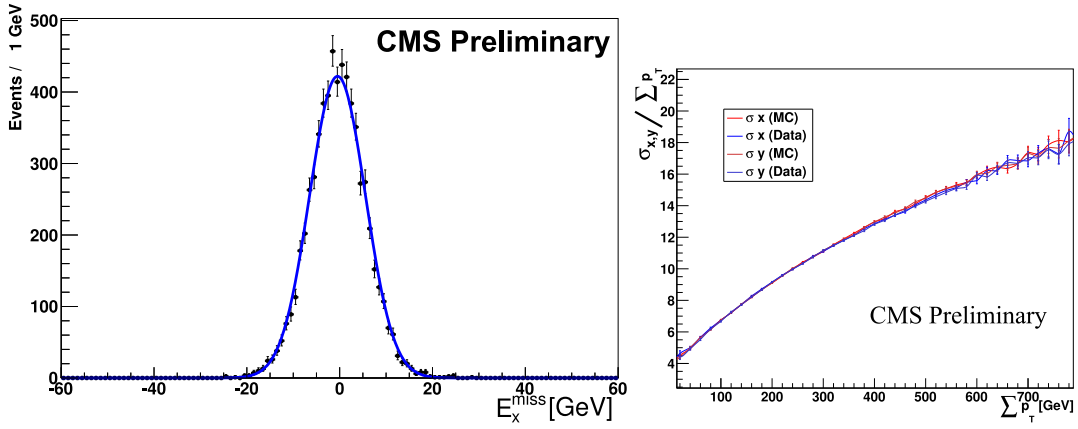

Figure 7.13.: In the left plot an example fit of E_x^{miss} is shown, on the right side the results of all fits for simulation and data. A good agreement is observed.

	A [GeV]	B [$\sqrt{\text{GeV}}$]	C
σ_x MC	2.3 ± 0.08	0.37 ± 0.01	$(8.2 \pm 0.4)10^{-3}$
σ_y MC	2.2 ± 0.08	0.37 ± 0.01	$(7.9 \pm 0.4)10^{-3}$
σ_x Data	1.9 ± 0.12	0.43 ± 0.02	$(5.7 \pm 0.5)10^{-3}$
σ_y Data	1.7 ± 0.12	0.46 ± 0.02	$(4.7 \pm 0.5)10^{-3}$

Table 7.4.: *Fit results of the E_T^{miss} resolution in different $\sum p_T$ regions.*

The results are shown in Table 7.4. Here the analytical function is used to evaluate the $\sum p_T$ dependent E_T^{miss} resolution. The E_T^{miss} resolution in simulation $f(\sum p_T^{MC})$ and the corrected resolution $f(\sum p_T^{MC} + \sum p_T^{unclusterd} \cdot N_{vertex})$ is taken and the E_T^{miss} in the simulation is smeared with the additional resolution:

$$\sigma_{new}^2 = \sigma_{MC}^2 - f(\sum p_T^{MC} + \sum p_T^{unclusterd} \cdot N_{vertex})^2$$

The event difference in the signal region between corrected and uncorrected MC is 5% on the Standard Model background and is taken as systematic uncertainty on the background expectation for the unclustered energy in data.
The effect on the signal by this correction is below 1%.

7.3.3. Pile Up

Additional to the systematic uncertainties from the unclustered energy there is an uncertainty on the number of pile up interactions observed and generated in data and simulation. To estimate this the number of pile up interactions was scaled by ±5% according to the official recommendations [93] for 3D reweighting. This has an influence on the events in the search region of about 3.2% for the background and about 1% influence on the signal.

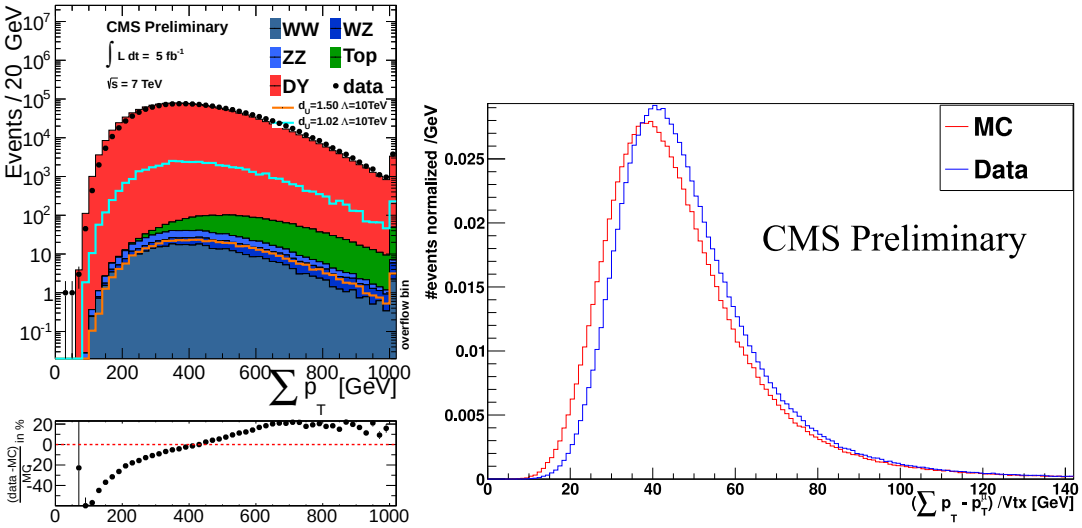

Figure 7.14.: More $\sum p_T$ is observed in data than in simulation (left). The shift can be seen more clearly when the muons are subtracted from $\sum p_T$ and divided by the number of observed vertices (right). The mean shifts 2.52 GeV in MC with respect to data.

7.3.4. PDF

The kinematic distribution of the quarks within the colliding partons is described by the PDFs, as described in Section 3.1. Since there is no theoretical prediction of the parameters, there have been efforts to describe the structure functions, so they represent the experimental data. Different groups have generated so called PDF sets with different theoretical assumptions and experimental data. These where used to generate the Monte Carlo events and calculate the cross sections in the involved physics processes. Each group, for each of their PDF set provides a best fit PDF set and others that contain variations of all parameters. The crucial point is that in some points of the parameter space different groups have best fit results that do not agree with each other.

To address this the PDF4LHC recommendations [94] are followed to estimate the influence of the PDF modelling on MC simulation.
The basic idea is to vary the PDF distributions according to their uncertainties. There are two possible ways to correct the used PDF sets. The first one is to rerun the full simulation which is very computing intensive. The second one is to reweight the events using their initial generated PDF information.
The first method is obviously the exact method, because the PDF is corrected exactly in the hard interaction as well as in the parton-showering. The less computing intensive method is the second one, but it only corrects the hard interaction. The reweighting method is used in this analysis with the LHAPDF package [95]. As observable the number of events in the search region is chosen and within one PDF set the errors are added in square. The PDF sets CTEQ6.6, MSTW2008 and NNPDF 2.1 [78, 96, 97] are used, provided by three independent groups. The additional uncertainty on the value of α_s is investigated with the same method.
To take the systematic error between the PDF groups into account the envelope of the different

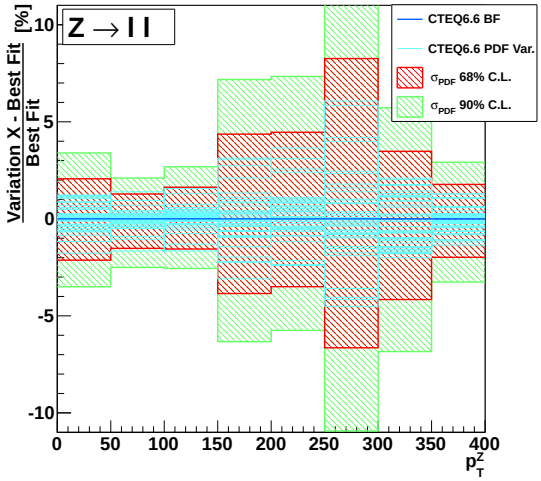

Figure 7.15.: Systematic uncertainty of the PDF uncertainties for the Dell-Yan processes on the number of events with $E_{\mathrm{T}}^{\mathrm{miss}} > 40\,\mathrm{GeV}$ depending on the p_T of the Z.

values with respect to the central value of each set is used (see Figure 7.15). The results can be found in Table 7.5. This leads to an uncertainty of 3.4% on the number of predicted background events from simulation.
Because the $t\bar{t}$ and WW backgrounds are determined with a data-driven method only three backgrounds contain systematic PDF uncertainties.

Process	systematic uncertainty
DY	1.1%
WZ	2.0%
ZZ	2.5%
Signal	3%

Table 7.5.: *Influence of PDF uncertainties on the number of events in the signal Region.*

7.3.5. Luminosity, Cross Section and Reconstruction Uncertainties

There are several uncertainties that change the number of expected backgrounds. For luminosity 2.2% uncertainty is assumed as recommended by the luminosity group.
The number of b-tagged jets is scaled up and down according to their uncertainties. But this shows no effect in the search region for background or signal. The efficiencies were studied in [57].
For detector acceptance uncertainties of 2% are taken, as the tag and probe suggests. Here detector acceptance is understood as the fraction of muons being reconstructed in the kinematic and geometrical boundaries of the CMS detector. In Run B a inefficiency in the endcaps lead to a ratio between MC and data of 95.6% [84]. The simulation is corrected for this inefficiency. The HLT trigger efficiency was estimated in Data and MC using the standard tag and probe method and agrees within 1%. For the isolation requirement no pile up dependency was seen.

For the background contributions taken from the Monte Carlo simulation the uncertainties were determined by varying the renormalization and factorization scales up and down by factors of two and one half with MCFM [81] and FEWZ [82]. The results are in Table 7.6. The systematic uncertainties on the background event expectation is summed up according to their cross section. A systematic uncertainty of 2.0% on the background expectation was calculated.

Process	σin pb	Generator
DY	3048 ± 34	FEWZ
WZ	18.2 ± 0.7	MCFM
ZZ	5.9 ± 0.15	MCFM

Table 7.6.: *Estimated cross sections with errors from MCFM and FEWZ.*

7.3.6. Summary of Systematic Uncertainties and Final Event Yields

To summarize the systematic uncertainties the impact from the different sources on the search region is shown in Table 7.7. From the $e\mu$-method there are 37.7 ± 5.7 events predicted for the

	Background MC	Signal
Jet resolution and scale	6.2%	1.4%
Unclustered energy	5%	$< 1\%$
$E_{\mathrm{T}}^{\mathrm{miss}}$ corrections	8%	1%
pile up	3.2%	1%
PDF	3.4%	1%
Cross sections	2%	-
Efficiencies	3%	
Luminosity	2.2%	

Table 7.7.: *Summary of all systematic uncertainties on the number of events in the signal region.*

$t\bar{t}$ and WW background. The other backgrounds (DY,WZ,ZZ) are estimated by the simulation and sum up to 52.4 ± 7.9 events. This leads to a total Standard Model prediction of 90.2 ± 9.7 events. In the data 89 events are observed.

7.4. Cut Optimisation

The aim of a cut optimisation is to the best expected limit for a Unparticle exclusion. There are five analysis specific cuts used in this analysis. They can be divided into two categories: cuts on continuous variables and cuts on discrete values. The discrete values are the number of jets and the number of b-tagged jets. The other cuts are on the invariant mass, $\Delta\phi(Z, E_{\mathrm{T}}^{\mathrm{miss}})$ and $E_{\mathrm{T}}^{\mathrm{miss}}$. In order to estimate the best cut value several factors have to be taken into consideration. Since the Unparticle signal is a beyond the Standard Model processes with unknown parameters and only known in a leading order effective theory approximation, the

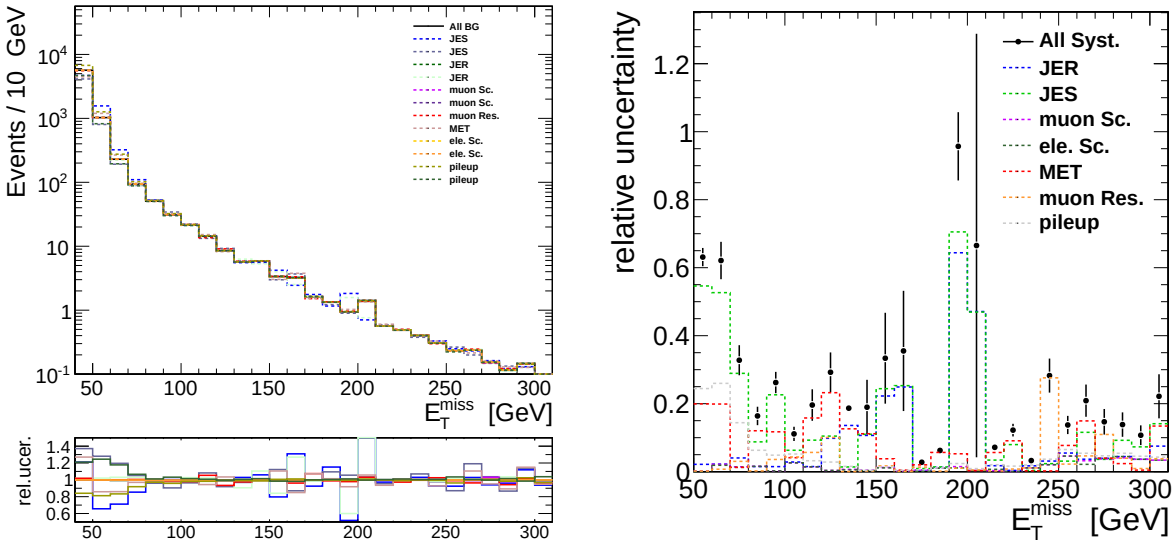

Figure 7.16.: The left plot shows the effect of the various systematic uncertainties for all backgrounds. In the right plot the relative uncertainty is shown, as well as the added systematic uncertainty with its statistical error for different $E_{\mathrm{T}}^{\mathrm{miss}}$ values.

MC description of the signal should not be trusted to cover every aspect of the new physics in full detail. Therefore a conservative approach to the cut values have been chosen.

	All Cuts	$\Delta\phi$	B-Jets	Number of Jets
WW	6.6 ± 0.4	10.4 ± 0.5	6.7 ± 0.4	8.2 ± 0.4
WZ	12.2 ± 0.2	13.9 ± 0.2	12.3 ± 0.2	15.4 ± 0.2
ZZ	29.4 ± 0.3	30.8 ± 0.3	29.7 ± 0.3	31.6 ± 0.3
Top	21.7 ± 0.8	26.9 ± 0.9	37.5 ± 1.0	51.9 ± 1.0
DY	9.0 ± 2.3	9.1 ± 2.3	9.0 ± 2.3	17.6 ± 3.0
all bg	79.0 ± 2.5	91.2 ± 2.5	95.2 ± 2.5	125.0 ± 3.3
data	89	101	114	151
efficiency for $d_U = 1.5$ in %	11.1 ± 0.2	11.4 ± 0.2	11.1 ± 0.2	11.8 ± 0.2

Table 7.8.: *For the signal selection cuts the number of events from all cuts except the labeled are summarized in this table.*

First the cuts on $\Delta\phi$ and the jets is discussed and then the cut on $E_{\mathrm{T}}^{\mathrm{miss}}$ is studied in more detail. The improvement of the expected limit for the remaining cuts is shown with N-1 cuts, where all signal selection cuts are applied except the named one. The MC prediction for the cut stages is shown in Table 7.8. To see the improvement in the expected limit, the MC prediction is used, whereas the final limit uses the data-driven background prediction for the Top and WW events. The systematic uncertainties especially for the object related uncertainties would differ for each cut stage. For simplicity and since the relative uncertainty is not expected to change drastically, the relative total uncertainty for the full signal selection of 11% is assumed for the number of background events. For the signal the d_U value of 1.5 was chosen with a

	All Cuts	$\Delta\phi$	B-Jets	Number of Jets
σ expected limit [fb]	46.7	48.9	50.2	59.3
relative difference to full selection	0	4.7%	7.3%	26.9%

Table 7.9.: *The effect of the signal selection cuts if the labelled cut is not used, shown for an Unparticle with* $d_U = 1.5$.

relative signal uncertainty of 6%. The results are summarized in Table 7.9. As can be seen the $\Delta\phi$ cut brings a 4.7% gain in the signal exclusion limit, by removing background from Top- or WW-events. The b-Jet cut only effects the top events, but reduces them nearly by a factor of 2. Hence it improves the limit by 7.3%. The largest limit improvement is due to the requirement of less than two jets, which improves the limit by 26.9% and this improvement does not take into account that the jet related uncertainties would rise with additional jets in the events. The jet p_T threshold of 30 GeV is relatively low, but this low threshold is needed to be a effective discriminator with respect to the top topology. A jet p_T threshold of 50 GeV would lead to a cross section decrease of 14.6%.

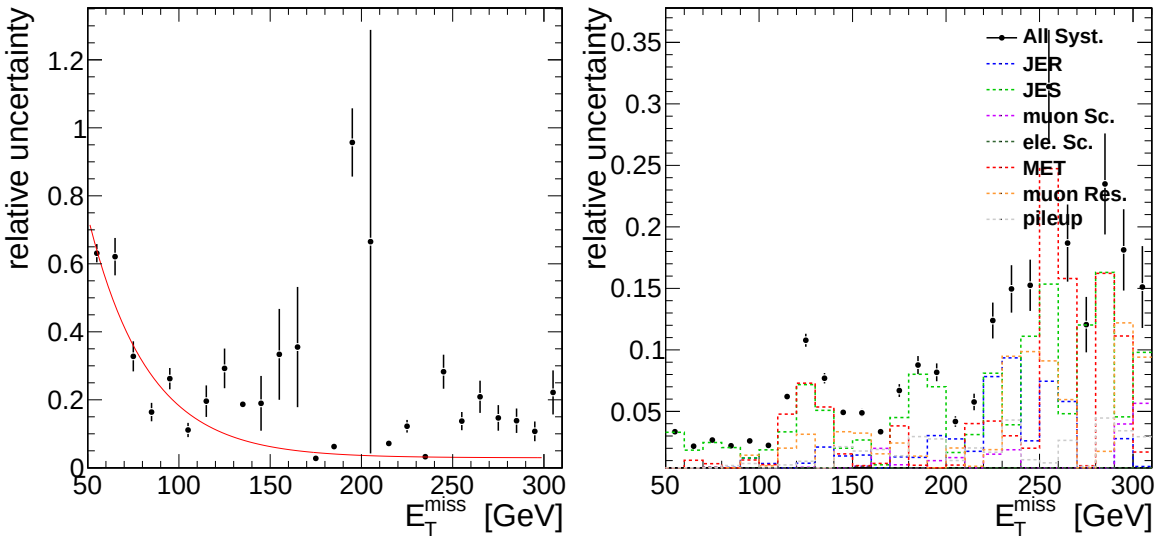

Figure 7.17.: In the left plot one can see the systematic uncertainties with their the statistical uncertainties. The statistical uncertainties of the systematic uncertainties is big. In the low E_T^{miss} region (60-150 GeV) a exponential dependency is observed. In order to calculate the optimal E_T^{miss} cut this region is fitted with a exponential. The fit can describe the low E_T^{miss} region reasonably well for a cut optimisation. In the right plot the object specific systematic uncertainties for the signal with $d_U = 1.5$ is shown.

To optimize the E_T^{miss} cut the dependency of the uncertainties on E_T^{miss} can not be neglected. The effect of the different object related uncertainties depending on E_T^{miss} can be seen in Figure 7.16 (left). For every uncertainty the difference to the undisturbed function can be seen in the ratio plot below. It should be noted that the cut optimisation is done with purely MC based background predictions and not with data driven estimate. Therefore the object

specific uncertainties are evaluated for all considered backgrounds. The relative uncertainties are added in quadrature. For scale uncertainties with a variation up and down the value with the higher deviation is chosen. The result can be seen in Figure 7.16 (right). The plot shows several features. The dominating uncertainties in the whole $E_{\mathrm{T}}^{\mathrm{miss}}$ spectrum are the jet related uncertainties. Over the $E_{\mathrm{T}}^{\mathrm{miss}}$ spectrum a bin to bin fluctuation can be observed. The statistical power of the combined systematic uncertainties varies over the $E_{\mathrm{T}}^{\mathrm{miss}}$ range, as is indicated by the shown statistical errors of the combined systematic uncertainty. Especially the two bins around 200 GeV have few MC events with a large weight, that are shifted by the jet uncertainties along the $E_{\mathrm{T}}^{\mathrm{miss}}$ spectrum. In fact there are two DY events that have a high weight due to the pile up reweighting. To minimize the influence of statistical fluctuations for the optimisation the relative systematic error depending on $E_{\mathrm{T}}^{\mathrm{miss}}$ is fitted with an exponential function, seen in Figure 7.17 (left). The function can smooth the parameter range 60-150 GeV, in which the optimal $E_{\mathrm{T}}^{\mathrm{miss}}$ cut is expected. For the signal efficiency the same approach is applied, except the signal uncertainties seem to rise with higher $E_{\mathrm{T}}^{\mathrm{miss}}$, therefore a linear function is fitted.
The best expected limits for different values of d_U are plotted in Figure 7.18. A clear trend is observable. The samples with a low d_U have a lower optimal cut value than the samples with higher d_U value. But for all samples the optimal cut value has a broad minimum and $E_{\mathrm{T}}^{\mathrm{miss}} > 100$ GeV is close to optimal for all all values of d_U.

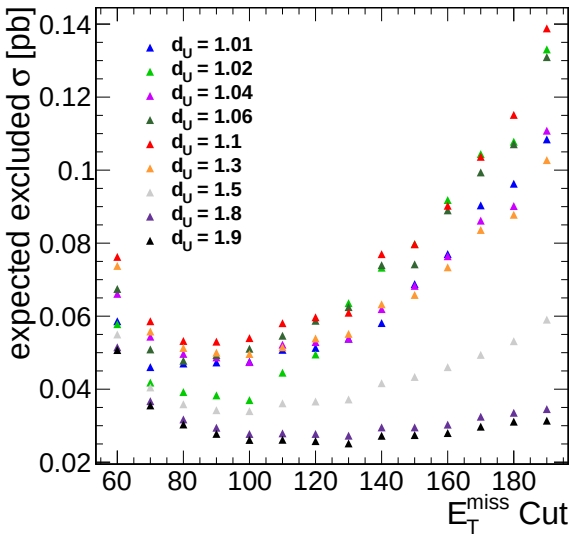

Figure 7.18.: The optimal cut value for $E_{\mathrm{T}}^{\mathrm{miss}}$ for different signals.

7.5. Signal Efficiency

The signal efficiency is one of the important elements of this analysis. It can be factorized into five efficiencies:

- trigger
- acceptance

- reconstruction
- muon ID
- signal selection
- $E_{\mathrm{T}}^{\mathrm{miss}}$ cut

The efficiencies are all relative to the number of generated events. Because the signal has two muons in the detector, the trigger efficiency is very close to 1. Figure 7.19 shows the efficiencies with respect to generated events and it can be seen that the trigger efficiency slightly improves with higher d_U. The acceptance is defined for two muons, that are both within the η range of $|\eta| < 2.1$ and have a p_T higher than 32 GeV for the leading muon and 15 GeV for the other. The muon ID efficiency is defined as two muons that are reconstructed, and fulfil the muon id cuts. They have to have an opposite electric charge and the event is not allowed to have an additional muon or electron. In addition to that the invariant mass of the two muons has to be above 50 GeV due to MC-data comparability. One can see that these standard requirements reduce the signal to about 50% efficiency. In comparison to this the efficiency lost due to the signal selection, where all cuts discussed in detail in Section 7.1 are applied, is relatively small. The efficiency drops from about 50% to about 40%. For the exact numbers see Table 7.2. The main signal efficiency loss is due to the $E_{\mathrm{T}}^{\mathrm{miss}}$ cut. The results are summarized in Table 7.10. This is due to the fact that the Unparticle signal peaks at low $E_{\mathrm{T}}^{\mathrm{miss}}$. The $E_{\mathrm{T}}^{\mathrm{miss}}$ cut is therefore the most important cut in this analysis and has therefore been discussed in section 7.4. The systematic uncertainties for the signal efficiencies are smaller

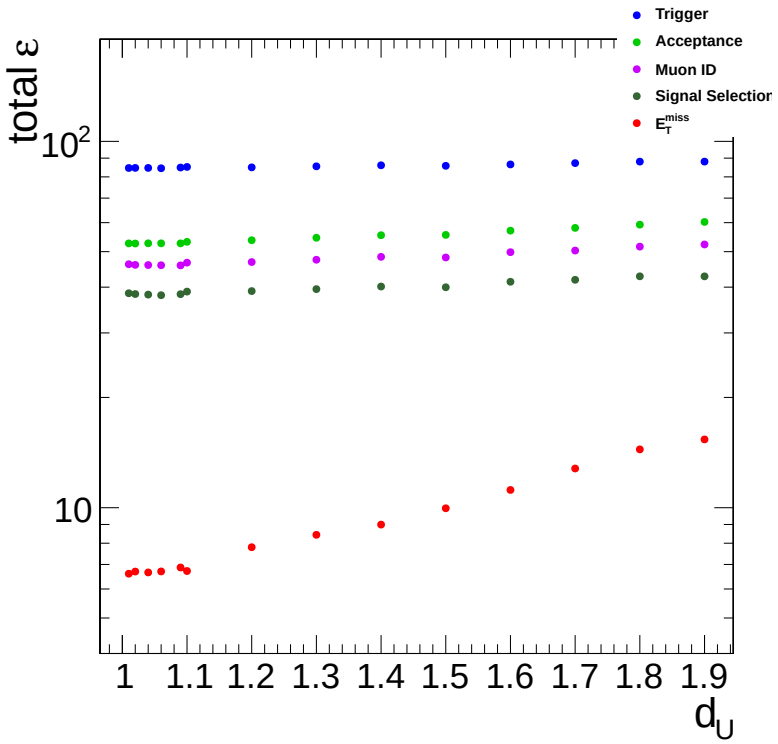

Figure 7.19.: The total signal efficiency for different d_U, applied successively.

than the background uncertainties. This is mainly due to the flatter $E_{\mathrm{T}}^{\mathrm{miss}}$ spectrum of the signal. The object specific uncertainties become larger for higher $E_{\mathrm{T}}^{\mathrm{miss}}$.

d_U	1.01	1.02	1.04	1.06	1.10	1.20	1.30	1.40	1.50	1.60	1.70	1.80	1.90
ε in %	6.6	6.7	6.7	6.7	6.7	7.8	7.5	9.0	11.2	11.2	12.8	14.4	15.4
σ (ε) in % (abs)	0.3	0.3	0.3	0.3	0.3	0.4	0.3	0.4	0.5	0.4	0.6	0.6	0.6

Table 7.10.: *The signal efficiencies with all relative systematic uncertainties.*

8. Results

Most results in modern physics have to be interpreted with a statistical model. In context of searches for new physics one wants to have a measure of the agreement of the measured data with the expected background and derive from that a statement about the model validity. In order to do this one has to define a concept of probability. The two main statistical schools to define probability are the frequentist and the Bayesian approach [89].
The frequentist statistics defines probability as the frequency of the outcome for a repeatable experiment in the limit of infinite repetition. This approach was the most common in the last years. From the frequentist probability one can define confidence intervals as parameter spaces that cover the true value of a parameter with a specified probability. The benefit of the approach is its independence from prior beliefs. Within this statistical model it is not possible to describe model assumptions such as systematic uncertainties, because one would break the purely frequentist ansatz.
The Bayesian statistics describes probability as a degree of belief. Each parameter can be described by a probability density function (p.d.f.), which expresses the knowledge about where the true value lies. This allows a coherent way to integrate additional information such as systematic uncertainties. The Bayesian model forces the experimenter to define the model assumptions in prior p.d.f.'s.
To handle systematic uncertainties in a frequentist model a so called hybrid method is often used, where the evaluation of the confidence interval is done with a frequentist approach with a Bayesian description of the systematic uncertainties. This may not be exactly correct, because of the fundamental differences in the theoretical interpretations, but in the used applications the numerical results of the different methods are similar.
This analysis uses the hybrid ansatz, because it is the agreement within the CMS Collaboration to use the frequentist interpretation.

8.1. Hypothesis Test

In searches for new physics the most common used *statistical test* is the hypothesis test, where the hypothesis of new physics is tested against the hypothesis of no new physics. The most common ansatz is the test of *signal+background* against the *background only* hypothesis. The signal therefore has to be quantifiable in a certain variable, such as the number of events with specific characteristics. One of the simplest hypothesis test is the single bin counting experiment, where the number of *signal+background* events are compared with the number of *background only* events. In case background and signal have different shapes depending on a certain variable, a shape based approach can gain some sensitivity. Following the frequentist interpretation, the event numbers in both cases can be assumed to be Poisson distributed, with the probability to find n events, when μ expected [89]:

$$L(\mu, n) = \frac{\mu^n e^{-\mu}}{n!}. \tag{8.1}$$

For the *signal+background* hypothesis this would mean, that $\mu = s + b$ and $\mu = b$ for the *background only* hypothesis. The likelihood ratio for the two hypothesis is then:

$$Q = \frac{L(\mu_{s+b}, n)}{L(\mu_b, n)}, \tag{8.2}$$

with the measurement n. For more than one bin one can define the likelihood ratio as the product of the likelihood ratios of N individual bins :

$$Q = \prod_i^N Q_i. \tag{8.3}$$

The frequentist test statistics is conventionally defined as $t = -2 \ln Q$ and used to define confidence intervals.

8.1.1. Hybrid Method and Profile Likelihood

The likelihood ratio so far only considered statistical uncertainties, but for the majority of the HEP results the systematic uncertainties are the dominant ones. As explained before the systematic uncertainties are modelled with bayesian priors. The likelihood is therefore multiplied by the adequate number of prior functions:

$$L(\mu, n, \theta) = L(\mu, n) \prod_i \pi_i(\theta_i). \tag{8.4}$$

Each prior function $\pi_i(\theta_i)$ describes a nuisance parameter, which influences the measurement, but is not of immediate interest[1]. Following the bayesian approach the shape of the priors has to be set. It is not a priori clear which shape a prior function should have, but some assumptions can be made. One of the obvious choices would be a gaussian shaped prior, since gaussian distributed uncertainties are the most common and have intriguing mathematical properties. One of the most interesting properties is that the sum of gaussian distributed variables is also a gaussian distributed, which is an important feature to describe most uncertainties correctly. In the case of a prior however the shape should be conserved under the product. One function that satisfies this need is the lognormal function. In the context of statistical evaluations it has therefore become the standard to use lognormal shaped priors.
To gain a more accurate result the expectation values of the nuisance parameters can be obtained by a likelihood maximization. This is called profile likelihood ratio [98]:

$$Q = \frac{L(\mu_{s+b}, n, \hat{\theta})}{L(\mu_b, n, \hat{\hat{\theta}})}. \tag{8.5}$$

The two vectors of nuisance parameters $\hat{\theta}$ and $\hat{\hat{\theta}}$ are fixed by the minimized likelihood under the assumption μ_{s+b} for $\hat{\theta}$ and μ_s for $\hat{\hat{\theta}}$.
To evaluate the test statistics with all systematics uncertainties *pseudo-experiments* have to be performed and the results are filled into a histogram. The pseudo-experiments are performed as follows:

[1] For instance calibration constants influence the measurement, but are obtained from a second (independent) measurement.

- get a random number for n_{exp} according to the Poisson distribution
- get a random value from the prior p.d.f.'s
- evaluate $t = -\ln Q$ for the given values

This sampling is performed multiple times for the background only and the signal + background hypothesis. The resulting histogram is called $\mathcal{P}(t)$ in the following.
The probability of a certain value t_0 is then defined as:

$$p(t_0) = \int_{t_0}^{\infty} \mathcal{P}(t)\mathrm{d}t \tag{8.6}$$

8.2. The CL_s Method

Several confidence intervals for signal exclusion limits have been used in the past. The most common used confidence interval is the CL_s. As noted before confidence levels are interpreted as a region that covers a predefined part of the probability space. The CL_s is constructed from the background only hypothesis CL_b and and the signal plus background hypothesis CL_{s+b} and uses the previously defined ratio:

$$CL_s = \frac{CL_{s+b}}{CL_b}. \tag{8.7}$$

The CL_s confidence level is usually used as a 95% interval for exclusion. This means that in 5% of the pseudo-experiments the value is outside the interval. The most commonly used parameter of interest for new physics searches is the signal cross section. From the definition $CL_s \leq 5\%$ the parameter of interest t_0 can be calculated at the edge of the CL_s. For the signal cross section one can conclude that higher cross sections can be excluded with this method.

8.3. Cross Section Limit

For the statistical analysis a single bin counting experiment is used, with all events above a certain $E_{\mathrm{T}}^{\mathrm{miss}}$ threshold. Different parameter points were tested by variation of d_U. The energy scale Λ_U has no impact on the shape of the signal. The number of observed events after all cuts is consistent with the background only prediction. Therefore no evidence for Unparticles is seen and limits on the model with 95% CL are set. The number of expected events μ with a possible signal contribution is defined as:

$$\mu = B + \varepsilon\sigma\mathcal{L}, \tag{8.8}$$

where B is the number of expected background events and ε is the signal efficiency, σ is the signal cross section and $\mathcal{L}$ is the luminosity. The parameter of interest is the signal cross section σ. The signal efficiencies are summarized in Table 7.10.
For this analysis the RooStats [91] package was used with the `FrequentistCalculator`, the profile likelihood in the implementation of the RooStatsCl95 package [99]. The uncertainties from Section 7.3 were used. The central exclusion limit is shown in Figure 8.1(left) and Table 8.1. One can see two features in the cross section limit with respect to d_U. Firstly the limit improves with higher values of d_U, which mirrors the higher signal efficiency. In line with this the 1 and 2 sigma regions expand. Secondly the limits for d_U smaller than 1.1 are more or less flat.

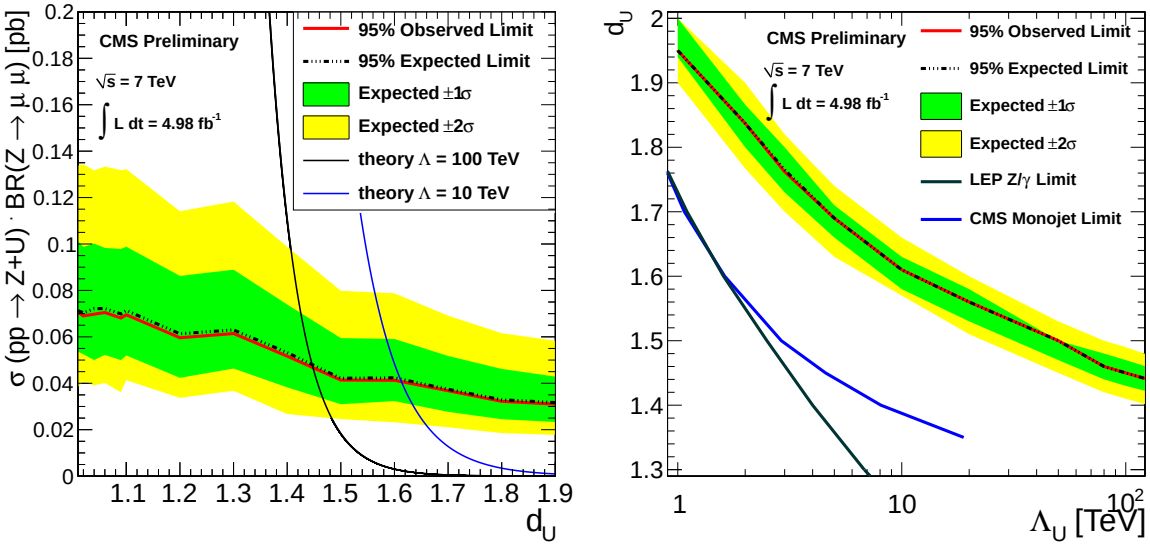

Figure 8.1.: The expected and observed CL_s limits as a function of d_U (left). The CL_s limit translated into the plane of Λ_U and d_U (right). For the parameter values below the limit curve the 95% CL cross section limit is less than the theoretical cross section.

8.3.1. Interpretation in the Unparticle Model

To interpret the results in the Unparticle model the three model parameters d_U, Λ_U and λ are used. The comparison with the theoretical cross section is therefore done either with a fixed λ or a fixed Λ_U. Because the efficiency depends only on d_U the $d_U - \Lambda_U$ and $d_U - \lambda$ planes are chosen to represent the model exclusion limit. The excluded parameter space in the $d_U - \Lambda_U$ plane is shown in Figure 8.1. For low d_U values one can see from equation 6.1 that the theoretical cross section is independent of Λ_U and therefore very high values can be excluded. The excluded Λ_U values as a function of d_U parameters are listed in Table 8.2.
To avoid the cross section divergence the model is interpreted in the $d_U - \lambda$ plane for fixed values of Λ_U [17]. As is shown in Figure 8.2 the limits converge for $d_U \to 1$ for different Λ_U values, but spread for higher values of d_U. In general one can make no theoretical constraint on λ. The exclusion curve is shown in Figure 8.2. The excluded d_U depending on λ parameters are listed in Table 8.3. One can see that for low scaling dimensions coupling parameters λ down to 10^{-3} are excluded. For lower dimensions the excluded coupling constant range is independent of Λ_U. The excluded coupling constant between $d_U = 1.01$ and $d_U = 1.03$ gets smaller, and rises exponentially for larger values of d_U. This feature is due to the cross section dependency on d_U which has a maximum at $d_U = 1.03$ and falls for $d_U \to 1$ to 0.
In consideration of both limits the limits show, that a scalar Unparticle with a low scaling dimension is very unlikely and for higher dimensions either the coupling constant has to be below 1, or the energy scale Λ_U has to be above 1 TeV.
In conclusion the limit shows that a scalar Unparticle would either have a large Λ_U at low dimensions or a scaling dimension above 2. The previous limits from Monojet and $Z/\gamma + E_T^{miss}$ searches are about ten times smaller than the presented limit.

d_U	obs. σ $[fb]$	exp. σ $[fb]$	$+1\sigma$ $[fb]$	-1σ $[fb]$
1.01	70.6	71.3	101.1	53.6
1.02	69.0	70.4	98.7	52.5
1.04	69.8	72.1	100.2	50.0
1.06	70.5	72.2	98.3	52.2
1.09	68.1	69.9	97.9	50.0
1.10	69.5	71.4	98.8	52.0
1.20	59.6	61.3	86.2	42.3
1.30	61.4	63.0	88.9	46.4
1.40	51.7	53.2	73.9	38.2
1.50	41.4	42.2	59.5	31.0
1.60	41.3	42.4	59.1	32.3
1.70	36.8	37.4	51.8	27.7
1.80	32.2	32.9	46.2	24.5
1.90	31.0	31.7	42.9	23.3

Table 8.1.: *The cross section limits from the Z+E_T^{miss} channel for different d_U*

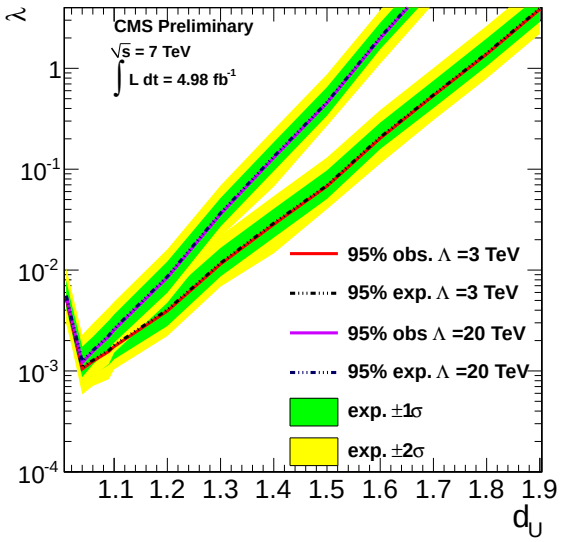

Figure 8.2.: The CL_s limit translated into the plane of λ and d_U . For the parameter values above the curve the 95% CL cross section limit is less than the theoretical cross section.

Λ_U[TeV]	obs. d_U	exp. d_U
1	1.95	1.95
2	1.84	1.84
3	1.77	1.77
5	1.69	1.69
10	1.61	1.61
20	1.56	1.56
50	1.50	1.50
80	1.46	1.46
100	1.45	1.45

Table 8.2.: Expected and observed 95% CL limits on d_U as a function of Λ_U.

d_U	$\Lambda_U = 3$ TeV		$\Lambda_U = 20$ TeV	
	obs. λ	exp. λ	obs. λ	exp. λ
1.01	$5.3{\cdot}10^{-3}$	$5.4{\cdot}10^{-3}$	$5.5{\cdot}10^{-3}$	$5.6{\cdot}10^{-3}$
1.02	$3.0{\cdot}10^{-3}$	$3.1{\cdot}10^{-3}$	$3.3{\cdot}10^{-3}$	$3.3{\cdot}10^{-3}$
1.04	$1.0{\cdot}10^{-3}$	$1.1{\cdot}10^{-3}$	$1.2{\cdot}10^{-3}$	$1.3{\cdot}10^{-3}$
1.06	$1.2{\cdot}10^{-3}$	$1.3{\cdot}10^{-3}$	$1.6{\cdot}10^{-3}$	$1.6{\cdot}10^{-3}$
1.09	$1.6{\cdot}10^{-3}$	$1.6{\cdot}10^{-3}$	$2.2{\cdot}10^{-3}$	$2.3{\cdot}10^{-3}$
1.10	$1.7{\cdot}10^{-3}$	$1.8{\cdot}10^{-3}$	$2.6{\cdot}10^{-3}$	$2.6{\cdot}10^{-3}$
1.20	$3.9{\cdot}10^{-3}$	$4.0{\cdot}10^{-3}$	$8.4{\cdot}10^{-3}$	$8.6{\cdot}10^{-3}$
1.30	$1.1{\cdot}10^{-2}$	$1.2{\cdot}10^{-2}$	$3.6{\cdot}10^{-2}$	$3.7{\cdot}10^{-2}$
1.40	$2.8{\cdot}10^{-2}$	$2.9{\cdot}10^{-2}$	0.13	0.13
1.50	$6.8{\cdot}10^{-2}$	$6.9{\cdot}10^{-2}$	0.45	0.46
1.60	0.20	0.21	2.0	2.0

Table 8.3.: Expected and observed 95% CL limits on λ as a function of d_U.

9. Conclusion and Outlook

9.1. Conclusion

This thesis presents a search for signatures of a scale invariant sector in $Z \rightarrow \mu\mu + E_{\mathrm{T}}^{\mathrm{miss}}$ events in proton proton collisions, collected with the CMS experiment at a center-of-mass energy $\sqrt{s} = 7\,\mathrm{TeV}$. The data were taken in 2011 and correspond to an integrated luminosity of $4.98\,\mathrm{fb}^{-1}$. $E_{\mathrm{T}}^{\mathrm{miss}}$ was used to discriminate between the Standard Model Drell-Yan process and the associated production of a Z-boson with an Unparticle. For the signal expectation MC events were simulated and analysed for the detector response and signatures. The $E_{\mathrm{T}}^{\mathrm{miss}}$ detector response was studied in detail for Z + $E_{\mathrm{T}}^{\mathrm{miss}}$ events. The background expectation from $t\bar{t}$ and WW events to the signal region was determined from the data using $e\mu$ events, and was found to be consistent with the prediction from the simulation.
The observed number of events with $E_{\mathrm{T}}^{\mathrm{miss}} > 100\,\mathrm{GeV}$ was found to be in agreement with the Standard Model prediction. Limits have been set on the Unparticle model, for values of the scaling dimension d_U between 1 and 1.9 at 95% CL. The disfavored values of λ are in the range of $5.3{\cdot}10^{-3}$ for $d_U = 1.01$ up to 0.20 for $d_U = 1.6$ at $\Lambda_U = 3\,\mathrm{TeV}$. For a fixed coupling constant $\lambda = 1$ values of d_U can be excluded from $d_U = 1.45$ with $\Lambda_U = 100\,\mathrm{TeV}$ up to $d_U = 1.95$ with $\Lambda_U = 1\,\mathrm{TeV}$. This is a significant improvement in comparison to previous direct searches and the first search in this channel at the LHC.

9.2. Outlook

In the future searching for Unparticles in additional model interpretations should be considered. For instance fermionic Unparticles have discovery potential in this channel at the LHC. A more detailed understanding of the model can be achieved if the universality of the Unparticle coupling is lifted. Because of the exponential dependency of the theoretical cross section on d_U, future analysis can expand the excluded parameter space in the high d_U region. The analysis statistics can be doubled with the inclusion of the $Z \rightarrow ee$ channel.

A. Appendix

A.1. Conformal Invariance

The conformal transformations are a group of transformations that satisfy the general coordinate transformation:

$$g_{\mu\nu} \to g'_{\mu\nu} = \Omega(x) g_{\mu\nu}, \tag{A.1}$$

which means the metric is invariant up to a scale. In order to evaluate the effect of this transformation the effect on a coordinate x^μ has to be calculated. This leads to a differential equation that defines the possible conformal transformations for x^μ. The following calcucation os based on [11].
As every coordinate transformation it can be divided into infinitesimal transformations:

$$x^\mu \to x'^\mu = x^\mu + \epsilon^\mu(x) \Rightarrow \qquad g'_{\mu\nu} = g_{\mu\nu} - (\partial_\mu \epsilon_\nu + \partial_\nu \epsilon_\mu) \tag{A.2}$$

In order to satisfy A.1, A.2 has to be proportional to $g_{\mu\nu}$, therefore

$$\partial_\mu \epsilon_\nu + \partial_\nu \epsilon_\mu = f(x) g_{\mu\nu} \tag{A.3}$$

taking the trace results in:

$$\begin{aligned} g^{\mu\nu}(\partial_\mu \epsilon_\nu + \partial_\nu \epsilon_\mu) =& f(x) d \\ \Rightarrow 2\partial^\mu \epsilon_\mu =& f(x) d, \end{aligned} \tag{A.4}$$

where d is the dimension of the space. From here on only a flat space is considered with no space dependency $g_{\mu\nu}(x) := \eta_{\mu\nu}$. Taking the derivative ∂_ρ on A.3:

$$\partial_\rho \partial_\mu \epsilon_\nu + \partial_\rho \partial_\nu \epsilon_\mu = \partial_\rho f(x) \eta_{\mu\nu} \tag{A.5}$$

The second derivative $\partial_\mu \partial_\nu \epsilon_\rho$ can be constructed from A.5:

$$\begin{aligned} \eta_{\mu\nu}\partial_\rho f(x) - \eta_{\mu\rho}\partial_\nu f(x) - \eta_{\rho\nu}\partial_\mu f(x) =& \partial_\rho \partial_\mu \epsilon_\nu + \partial_\rho \partial_\nu \epsilon_\mu \\ & - \partial_\nu \partial_\mu \epsilon_\rho - \partial_\nu \partial_\rho \epsilon_\mu \\ & - \partial_\rho \partial_\mu \epsilon_\nu - \partial_\mu \partial_\nu \epsilon_\rho \\ =& -2\partial_\mu \partial_\nu \epsilon_\rho \end{aligned} \tag{A.6}$$

Contracting with $\eta^{\mu\nu}$:

$$\begin{aligned} d\partial_\rho f(x) - \partial_\rho f(x) - \partial_\rho f(x) =& -2\partial^2 \epsilon_\rho \\ \Rightarrow (d-2)\partial_\rho f(x) ==& -2\partial^2 \epsilon_\rho \end{aligned} \tag{A.7}$$

Applying ∂_ν on this expression and ∂^2 on A.3:

$$\begin{aligned}(2-d)\partial_\nu\partial_\rho f(x) &= 2\partial_\nu\partial^2\epsilon_\rho \\ \partial^2\partial_\mu\epsilon_\nu + \partial^2\partial_\nu\epsilon_\mu &= \partial^2 f(x)\eta_{\mu\nu} \\ \Rightarrow (2-d)\partial_\nu\partial_\rho f(x) &= \eta_{\nu\rho}\partial^2 f(x) \end{aligned} \tag{A.8}$$

contracting with $\eta^{\rho\nu}$ and A.5 leads to the defining differential equation:

$$(1-d)\partial^2 f(x) = 0 \tag{A.9}$$

$$\frac{2}{d}(1-d)\partial^2\partial_\rho\epsilon^\rho = 0 \tag{A.10}$$

A.2. Data-MC jet Corrections

The ratio of the dijet events in data and simulation is defined as follows:

$$C_{sym}(|\eta|) = \left\langle \frac{\mathcal{R}_{MC}^{\alpha<0.2}}{\mathcal{R}_{data}^{\alpha<0.2}} \right\rangle_{p_T}, \tag{A.11}$$

where $\mathcal{R}$ is defined in equation A.16 and α is defined as the ratio of the average momentum (see A.3) and the p_T of the third leading jet $\alpha = p_T^{Jet3}/p_T^{ave}$. The radiation correction k_{rad} is defined as

$$k_{rad} = \lim_{\alpha\to 0}\left(\frac{\left\langle \frac{\mathcal{R}_{MC}^{\alpha}}{\mathcal{R}_{data}^{\alpha}} \right\rangle_{p_T}}{\left\langle \frac{\mathcal{R}_{MC}^{\alpha<0.2}}{\mathcal{R}_{data}^{\alpha<0.2}} \right\rangle_{p_T}} \right) \tag{A.12}$$

and the asymmetry of the response in η is defined as:

$$\mathcal{A}_R(|\eta|) = \frac{R(+|\eta|) - R(-|\eta|)}{R(+|\eta|) + R(-|\eta|)}, \tag{A.13}$$

where $R(+|\eta|)$ ($R(-|\eta|)$) is defined as the response of jets measured in the positive (negative) z-direction.

A.3. Dijet p_T-Balancing

The dijet p_T-Balancing is an experimental method to relate the jet response of a barrel jet with $|\eta| < 1.3$ to jets with an arbitrary η. The Balance is defined as:

$$\mathcal{B} = \frac{p_T^{probe} - p_T^{barrel}}{p_T^{ave}} \tag{A.14}$$

and p_T^{ave} is the average p_T of the two leading jets:

$$p_T^{ave} = \frac{p_T^{probe} + p_T^{barrel}}{2} \tag{A.15}$$

The relative response is then defined as:

$$\mathcal{R}_{rel}(\eta^{probe}, p_T^{ave}) = \frac{2+ < \mathcal{B} >}{2- < \mathcal{B} >} \tag{A.16}$$

A.4. Unparticle Candidate Events

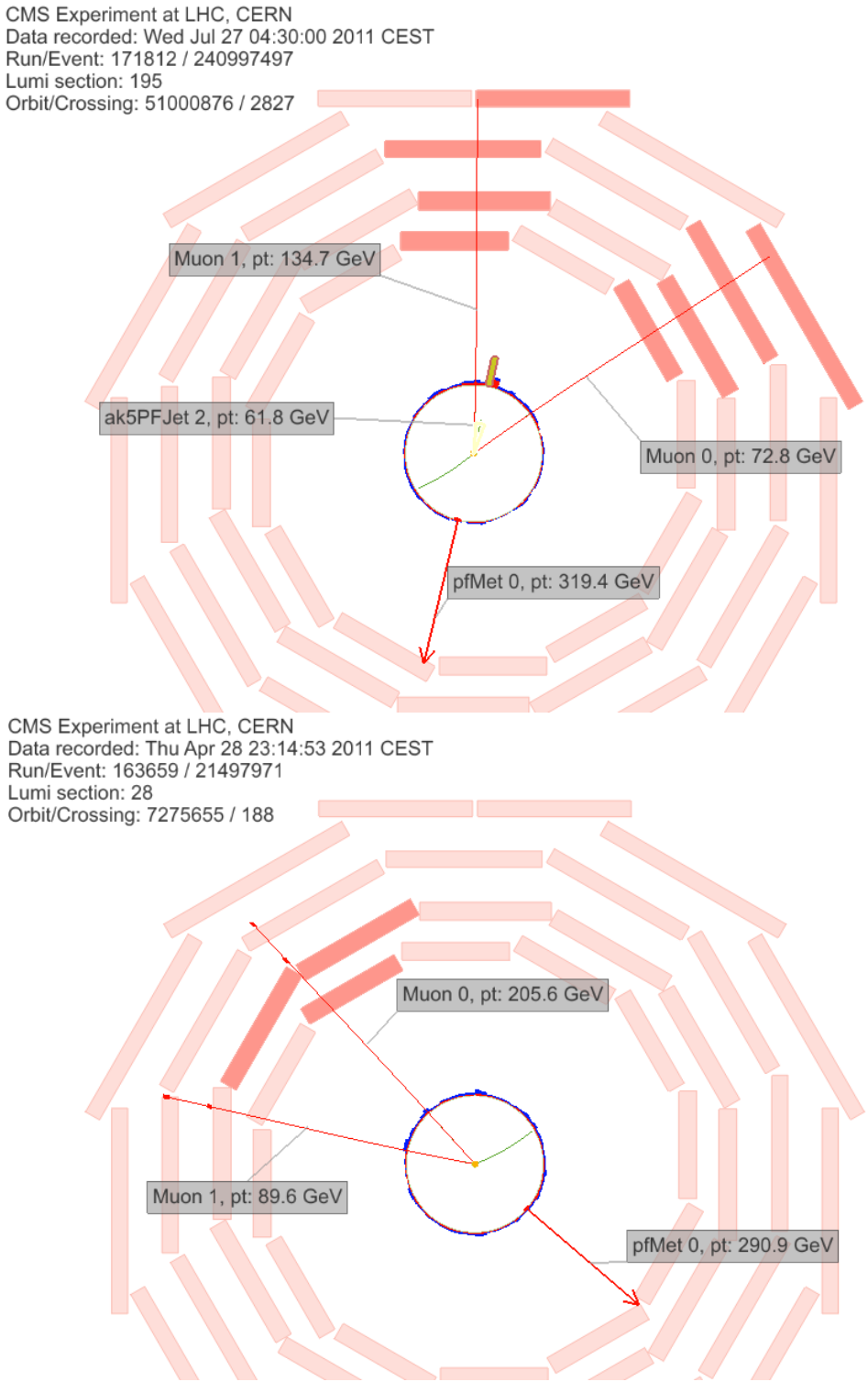

Figure A.1.: The data event with the highest and second highest $E_{\mathrm{T}}^{\mathrm{miss}}$ in the signal selection.

A.5. Units and Conventions

In this thesis all quantities are given in SI or natural units. While in the SI system c and $\hbar$:

$$\hbar = 1.055 \cdot 10^{-34} \frac{\mathrm{m}^2\,\mathrm{kg}}{\mathrm{s}} \quad \text{and} \quad c = 2.998 \cdot 10^{8} \frac{\mathrm{m}}{\mathrm{s}}, \tag{A.17}$$

in natural units both quantities are set to:

$$\hbar = c = 1 \tag{A.18}$$

This implies that the only unit left is energy for length and time are measured in inverse energy. The convention is to use eV as unit.
In particle physics a often used quantity is cross section, which is historically measured in barn [b], which is defined as:

$$1\,\mathrm{b} = 10^{-28}\,\mathrm{m}^2. \tag{A.19}$$

In particle physics the sum convention is used, which means that:

$$a_\mu b^\mu = \sum_\mu a_\mu b^\mu = \sum_\mu a_\mu b_\nu g^{\mu\nu}, \tag{A.20}$$

where $g^{\mu\nu}$ is the metric tensor.
The Standard Model particles written in this thesis use the following conventions:

- the charge of the Bosons Z^0, $W^\pm$ is suppressed
- the names for the fermions (electron or muon) are used for both fermion and anti-fermion

Bibliography

[1] H. Georgi, "Unparticle physics," *Phys.Rev.Lett.* **98** (2007) 221601, arXiv:hep-ph/0703260 [hep-ph].

[2] J. L. Rosner, "The Standard model in 2001," arXiv:hep-ph/0108195 [hep-ph].

[3] A. Pich, "The Standard model of electroweak interactions," arXiv:hep-ph/0502010 [hep-ph].

[4] M. E. Peskin and D. V. Schroeder, *An Introduction to quantum field theory*. Perseus Books, 1995. ISBN-9780201503975.

[5] Landolt-Börnstein, *Group I Elementary Particles, Nuclei and Atoms*. Springer-Verlag, 2008.

[6] A. Collaboration, "Observation of a new particle in the search for the Standard Model Higgs boson with the ATLAS detector at the LHC," arXiv:1207.7214 [hep-ex].

[7] C. Collaboration, "Observation of a new boson at a mass of 125 GeV with the CMS experiment at the LHC," *Phys.Lett.B* (2012) 8, arXiv:1207.7235 [hep-ex].

[8] CMS Collaboration, "Search for the fermiophobic model Higgs boson decaying into two photons in pp collisions at $\sqrt{s}$ = 7 and 8 TeV,". CMS-PAS-HIG-12-022.

[9] J.-F. Fortin, B. Grinstein, and A. Stergiou, "Cyclic unparticle physics," *Phys.Lett.* **B709** (2012) 408–412, arXiv:1110.1634 [hep-th].

[10] O. Aharony, S. S. Gubser, J. M. Maldacena, H. Ooguri, and Y. Oz, "Large N field theories, string theory and gravity," *Phys.Rept.* **323** (2000) 183–386, arXiv:9905111 [hep-th].

[11] P. Di Francesco, P. Mathieu, and D. Senechal, *Conformal field theory*. Springer, New York, USA, 1997.

[12] H. Georgi, "Another odd thing about unparticle physics," *Phys.Lett.* **B650** (2007) 275–278, arXiv:0704.2457 [hep-ph].

[13] H. Georgi and Y. Kats, "An Unparticle Example in 2D," *Phys.Rev.Lett.* **101** (2008) 131603, arXiv:0805.3953 [hep-ph].

[14] H. Georgi and Y. Kats, "Unparticle self-interactions," *JHEP* **1002** (2010) 065, arXiv:0904.1962 [hep-ph].

[15] B. Grinstein, K. A. Intriligator, and I. Z. Rothstein, "Comments on Unparticles," *Phys.Lett.* **B662** (2008) 367–374, arXiv:0801.1140 [hep-ph].

[16] K. Cheung, W.-Y. Keung, and T.-C. Yuan, "Collider Phenomenology of Unparticle Physics," *Physical Review D* **76** no. 5, (June, 2007) 37, arXiv:0706.3155. http://arxiv.org/abs/0706.3155.

[17] M. Strassler, "Private communication," 2012.

[18] S. Ask, I. Akin, L. Benucci, A. De Roeck, M. Goebel, *et al.*, "Real Emission and Virtual Exchange of Gravitons and Unparticles in Pythia8," *Comput.Phys.Commun.* **181** (2010) 1593–1604, arXiv:0912.4233 [hep-ph].

[19] J. Bergstrom and T. Ohlsson, "Unparticle Self-Interactions at the Large Hadron Collider," *Phys.Rev.* **D80** (2009) 115014, arXiv:0909.2213 [hep-ph].

[20] A. Delgado, J. R. Espinosa, J. M. No, and M. Quiros, "A Note on Unparticle Decays," *Phys. Rev.* **D79** (2009) 055011, arXiv:0812.1170 [hep-ph].

[21] C.-D. Lu, W. Wang, and Y.-M. Wang, "Lepton flavor violating processes in unparticle physics," *Phys.Rev.* **D76** (2007) 077701, arXiv:0705.2909 [hep-ph].

[22] J. McDonald, "Cosmological Constraints on Unparticles," *JCAP* **0903** (2009) 019, arXiv:0709.2350 [hep-ph].

[23] H. Wei, "Relaxing the Cosmological Constraints on Unparticle Dark Component," *Eur.Phys.J.* **C62** (2009) 579–586, arXiv:0812.4489 [gr-qc].

[24] D. Stancato and J. Terning, "The Unhiggs," *JHEP* **0911** (2009) 101, arXiv:0807.3961 [hep-ph].

[25] C. Englert, D. Goncalves-Netto, M. Spannowsky, and J. Terning, "Constraining the Unhiggs with LHC data." IPPP-12-23, DCPT-12-46, 2012.

[26] G. Cacciapaglia, G. Marandella, and J. Terning, "Colored Unparticles," *JHEP* **0801** (2008) 070, arXiv:0708.0005 [hep-ph].

[27] Y. Liao, "Some Issues in a Gauge Model of Unparticles," *Eur.Phys.J.* **C60** (2009) 125–134, arXiv:0804.4033 [hep-ph].

[28] T. G. Rizzo, "Unique Signatures of Unparticle Resonances at the LHC," *JHEP* **11** (2008) 039, arXiv:0809.4659 [hep-ph].

[29] J. L. Feng, A. Rajaraman, and H. Tu, "Unparticle self-interactions and their collider implications," *Phys.Rev.* **D77** (2008) 075007, arXiv:0801.1534 [hep-ph].

[30] A. Delgado and M. J. Strassler, "A Simple-Minded Unitarity Constraint and an Application to Unparticles," *Phys. Rev.* **D81** (2010) 056003, arXiv:0912.2348 [hep-ph].

[31] A. Delgado, J. R. Espinosa, and M. Quiros, "Unparticles Higgs Interplay," *JHEP* **0710** (2007) 094, arXiv:0707.4309 [hep-ph].

[32] M. Dahiya, S. Dutta, and R. Islam, "Constraining Unparticles from Top Physics at TeVatron," arXiv:1206.5447 [hep-ph].

[33] A. Moyotl, A. Rosado, and G. Tavares-Velasco, "Lepton electric and magnetic dipole moments via lepton flavor violating spin-1 unparticle interactions," *Phys.Rev.* **D84** (2011) 073010, arXiv:1109.4890 [hep-ph].

[34] L.-G. Bian, "Constraints of Unparticle Physics Parameters from $K^0 - \bar{K}^0$ Mixing," arXiv:1108.1538 [hep-ph].

[35] CMS Collaboration, "Search for New Physics with a Mono-Jet and Missing Transverse Energy in pp Collisions at $\sqrt{s} = 7$ TeV," *Phys.Rev.Lett.* **107** (2011) 201804, arXiv:1106.4775 [hep-ex].

[36] S. Kathrein, S. Knapen, and M. J. Strassler, "Bounds from LEP on unparticle interactions with electroweak bosons," *Phys.Rev.* **D84** (2011) 015010, arXiv:1012.3737 [hep-ph].

[37] R. Thorne, "The Role of uncertainties in parton distribution functions," *PHYSTAT-LHC Workshop on Statistical Issues* (2007) 141–150, arXiv:0711.2986 [hep-ph].

[38] L. Evans and P. B. (editors), "LHC Machine," *Journal of Instrumentation* **3** no. 08, (2008) S08001. http://stacks.iop.org/1748-0221/3/i=08/a=S08001.

[39] M. Ferro-Luzzi, "LHC Operation - as viewed from the Experiments,". http://indico.cern.ch/getFile.py/access?contribId=0&sessionId=0&resId=0&materialId=paper&confId=164089.

[40] CMS Collaboration, "The CMS experiment at the CERN LHC," *JINST* **3** (2008) S08004.

[41] R. Steinhagen, "LHC Status and Future Upgrade Plans." http://indico.cern.ch/contributionDisplay.py?contribId=481&confId=181298. ICHEP 2012 Presentation.

[42] A. Starodumov, "Operation of the cms pixel detector," Tech. Rep. CMS-CR-2011-187. CERN-CMS-CR-2011-187, CERN, Geneva, Sep, 2011.

[43] CMS Collaboration, "Performance of CMS muon reconstruction in pp collision events at sqrt(s) = 7 TeV," arXiv:1206.4071 [physics.ins-det].

[44] CMS Collaboration, *The CMS muon project: Technical Design Report*. Technical Design Report CMS. CERN, Geneva, 1997.

[45] CMS Collaboration, "Performance of the resistive plate chambers in the CMS experiment," *JINST* **7** (2012) C01104.

[46] CMS Collaboration, "Track reconstruction in the cms tracker," Tech. Rep. CMS NOTE-2006-041, CERN, Geneva, Dec, 2006.

[47] CMS Collaboration, "Iterative tracking." https://twiki.cern.ch/twiki/bin/view/CMSPublic/SWGuideIterativeTracking.

[48] R. Fruhwirth, "Application of Kalman filtering to track and vertex fitting," *Nucl.Instrum.Meth.* **A262** (1987) 444–450.

[49] G. Welch and G. Bishop, "An introduction to the kalman filter," Tech. Rep. TR 95-041, UNC-Chapel Hill, 1995. http://www.cs.unc.edu/~welch/kalman/kalmanIntro.html.

[50] CMS Collaboration, "Muon Reconstruction in the CMS Detector," Tech. Rep. CMS AN 2008-097, CERN, Geneva, Jul, 2009.

[51] CMS Collaboration, "Reconstruction of Electrons with the Gaussian-Sum Filter in the CMS Tracker at the LHC," Tech. Rep. CMS NOTE 2005-001, CERN, Geneva, 2005.

[52] CMS Collaboration, "Electron reconstruction within the particle flow algorithm," Tech. Rep. CMS AN -2010/034, CERN, Geneva, Mar, 2010.

[53] CMS Collaboration, *CMS Physics Technical Design Report Volume I: Detector Performance and Software*. Technical Design Report CMS. CERN, Geneva, 2006.

[54] M. Cacciari, G. P. Salam, and G. Soyez, "The Anti-k_T jet clustering algorithm," *JHEP* **0804** (2008) 063, arXiv:0802.1189 [hep-ph].

[55] CMS Collaboration, "Determination of Jet Energy Calibration and Transverse Momentum Resolution in CMS," *JINST* **6** (2011) P11002, arXiv:1107.4277 [physics.ins-det].

[56] CMS Collaboration, "Algorithms for b jet identification in cms," Tech. Rep. CMS AN 2009-085, CERN, Geneva, Aug, 2009.

[57] CMS B-tag Vertex Group, "b-Jet Identification in the CMS Experiment," tech. rep., CERN, Geneva, Feb, 2012. CMS PAS-BTV-11-004.

[58] CMS Collaboration, "Measurement of the identification efficiency for b-quark jets in 2011 data in dijet events with a soft muon," Tech. Rep. CMS AN-11-503, CERN, Geneva, Feb, 2012.

[59] OPAL Collaboration, "Search for anomalous photonic events with missing energy in e^+e^- collisions at $\sqrt{s}$ = 130 GeV, 136 GeV and 183 GeV," *Eur.Phys.J.* **C8** (1999) 23–40, arXiv:9810021 [hep-ex]. CERN-EP-98-143.

[60] DELPHI Collaboration, "Photon events with missing energy at $\sqrt{s}$ = 183 GeV to 189 GeV," *Eur.Phys.J.* **C17** (2000) 53–65, arXiv:0103044 [hep-ex]. CERN-EP-2000-021.

[61] ALEPH Collaboration, "Single photon and multiphoton production in e^+e^- collisions at $\sqrt{s}$ up to 209 GeV," *Eur.Phys.J.* **C28** (2003) 1–13. CERN-EP-2002-033.

[62] L3 Collaboration, "Single photon and multiphoton events with missing energy in e^+e^- collisions at LEP," *Phys.Lett.* **B587** (2004) 16–32, arXiv:0402002 [hep-ex]. CERN-EP-2003-068.

[63] CDF Collaboration, "Search for large extra dimensions in final states containing one photon or jet and large missing transverse energy produced in $p\bar{p}$ collisions at $\sqrt{s}$ = 1.96-TeV," *Phys.Rev.Lett.* **101** (2008) 181602, arXiv:0807.3132 [hep-ex]. FERMILAB-PUB-08-247-E.

[64] CDF Collaboration, "Search for Large Extra Dimensions in the Production of Jets and Missing Transverse Energy in p anti-p Collisions at $\sqrt{s}$ = 1.96 TeV," *Phys.Rev.Lett.* **97** (2006) 171802, arXiv:0605101 [hep-ex]. FERMILAB-PUB-06-079-E.

[65] CMS Jet MET Group, "Derivation of Type-II corrections from $Z \to ee$ events in 7 TeV data for Calo- and Pf MET," tech. rep., CERN, Geneva, Jan, 2011. CMS AN -2010-396.

[66] CMS Collaboration, "CMS MET Filters." `https://twiki.cern.ch/twiki/bin/viewauth/CMS/MissingETOptionalFilters`.

[67] CMS muon group, "The cms muon id." `https://twiki.cern.ch/twiki/bin/view/CMSPublic/SWGuideMuonId`.

[68] CMS eγ group, "The cms cut based electron id." `https://twiki.cern.ch/twiki/bin/view/CMS/EgammaCutBasedIdentification`.

[69] CMS Collaboration, "Particle flow event reconstruction in cms missconstruction and performance for jets, taus, and missing transverse energy," *CMS Physics Analysis Summary CMS PAS PFT-09/001* (2009) 25.

[70] CMS Collaboration, "Model unspecific search for new physics in pp collisions at $\sqrt{s} = 7$ tev," Tech. Rep. CMS PAS EXO-10-021, CERN, Geneva, Jun, 2011.

[71] T. Sjöstrand, S. Mrenna, and P. Z. Skands, "PYTHIA 6.4 Physics and Manual," *JHEP* **0605** (2006) 026, `arXiv:hep-ph/0603175 [hep-ph]`.

[72] T. Sjöstrand, S. Mrenna, and P. Z. Skands, "A Brief Introduction to PYTHIA 8.1," *Comput.Phys.Commun.* **178** (2008) 852–867, `arXiv:0710.3820 [hep-ph]`.

[73] J. Allison, K. Amako, J. Apostolakis, H. Araujo, P. Dubois, *et al.*, "Geant4 developments and applications," *IEEE Trans.Nucl.Sci.* **53** (2006) 270.

[74] I. Antcheva, M. Ballintijn, B. Bellenot, M. Biskup, R. Brun, *et al.*, "ROOT: A C++ framework for petabyte data storage, statistical analysis and visualization," *Comput.Phys.Commun.* **182** (2011) 1384–1385.

[75] C. Maggas *et al.*, "Aachen 3A Susy Analysis." `https://twiki.cern.ch/twiki/bin/viewauth/CMS/Aachen3ASusy`.

[76] S. Ask, "Simulation of Z plus Graviton/Unparticle Production at the LHC," *Eur.Phys.J.* **C60** (2009) 509–516, `arXiv:0809.4750 [hep-ph]`.

[77] R. Corke and T. Sjöstrand, "Interleaved Parton Showers and Tuning Prospects," *JHEP* **03** (2011) 032, `arXiv:1011.1759 [hep-ph]`.

[78] P. M. Nadolsky, H.-L. Lai, Q.-H. Cao, J. Huston, J. Pumplin, *et al.*, "Implications of CTEQ global analysis for collider observables," *Phys.Rev.* **D78** (2008) 013004, `arXiv:0802.0007 [hep-ph]`.

[79] J. Alwall, P. Demin, S. de Visscher, R. Frederix, M. Herquet, *et al.*, "MadGraph/MadEvent v4: The New Web Generation," *JHEP* **0709** (2007) 028, `arXiv:0706.2334 [hep-ph]`.

[80] R. Field, "Early LHC Underlying Event Data - Findings and Surprises," `arXiv:1010.3558 [hep-ph]`.

[81] J. M. Campbell and R. Ellis, "An Update on vector boson pair production at hadron colliders," *Phys.Rev.* **D60** (1999) 113006, arXiv:hep-ph/9905386 [hep-ph].

[82] R. Gavin, Y. Li, F. Petriello, and S. Quackenbush, "FEWZ 2.0: A code for hadronic Z production at next-to-next-to-leading order," *Comput.Phys.Commun.* **182** (2011) 2388–2403, arXiv:1011.3540 [hep-ph].

[83] N. Kidonakis, "Higher-order corrections to top-antitop pair and single top quark production," arXiv:0909.0037 [hep-ph].

[84] CMS Muon POG, "CMS Muon Efficiencies in Run 2011." https://indico.cern.ch/getFile.py/access?contribId=0&resId=0&materialId=slides&confId=175021.

[85] CMS Collaboration, "Measurement of the WW, WZ and ZZ cross sections at CMS," Tech. Rep. CMS-PAS-EWK-11-010, CERN, Geneva, 2011.

[86] CMS Collaboration, "Observation of a new boson with a mass near 125 gev," Tech. Rep. CMS PAS HIG-12-020, CERN, Geneva, 2012.

[87] CMS Collaboration, "Search for leptonic decays of W' bosons in pp collisions at sqrt(s)=7 TeV," arXiv:1204.4764 [hep-ex]. CMS-EXO-11-024, CERN-PH-EP-2012-103, submitted to J. High Energy Phys.

[88] C. Oleari, "The POWHEG-BOX," *Nucl.Phys.Proc.Suppl.* **205-206** (2010) 36–41, arXiv:1007.3893 [hep-ph].

[89] Particle Data Group, "Review of particle physics," *J.Phys.G* **G37** (2010) 075021.

[90] CMS Collaboration, "A search for excited leptons in pp Collisions at sqrt(s) = 7 TeV," *Phys. Lett.* **B704** (2011) 143–162, arXiv:1107.1773 [hep-ex].

[91] L. Moneta, K. Belasco, K. S. Cranmer, S. Kreiss, A. Lazzaro, *et al.*, "The RooStats Project," *PoS* **ACAT2010** (2010) 057, arXiv:1009.1003 [physics.data-an].

[92] CMS Collaboration, "Physics tdr volume i, the cms physics technical design report i," *CERN-LHCC-2006-001* (2006) 411pp.

[93] CMS Jet and MET Group, "Pile up systematic errors." https://twiki.cern.ch/twiki/bin/viewauth/CMS/PileupSystematicErrors.

[94] M. Botje, J. Butterworth, A. Cooper-Sarkar, A. de Roeck, J. Feltesse, *et al.*, "The PDF4LHC Working Group Interim Recommendations," arXiv:1101.0538 [hep-ph].

[95] M. R. Whalley, D. Bourilkov, and R. C. Group, "The Les Houches Accord PDFs (LHAPDF) and Lhaglue," arXiv:hep-ph/0508110.

[96] A. Martin, W. Stirling, R. Thorne, and G. Watt, "Parton distributions for the LHC," *Eur.Phys.J.* **C63** (2009) 189–285, arXiv:0901.0002 [hep-ph].

[97] **NNPDF Collaboration** Collaboration, R. D. Ball *et al.*, "Unbiased global determination of parton distributions and their uncertainties at NNLO and at LO," *Nucl.Phys.* **B855** (2012) 153–221, arXiv:1107.2652 [hep-ph].

[98] A. L. Read, "Presentation of search results: the cls technique," *Journal of Physics G: Nuclear and Particle Physics* **28** no. 10, (2002) 2693. http://stacks.iop.org/0954-3899/28/i=10/a=313.

[99] CMS Collaboration, "CMS User-Friendly Statistics Tools for Physics Analysis." https://twiki.cern.ch/twiki/bin/view/CMS/StatisticsTools.

Danksagung

Ich möchte diese Arbeit schließen mit einem Dank an die Menschen die es ermöglicht haben diese Arbeit zu schreiben und den Weg hierhin zu ebnen. Zu aller erst möchte ich meinen Eltern danken, die es mir ermöglicht haben Physik zu studieren und mir immer mit Rat und Tat zur Seite standen. Dem folgend möchte ich meiner Freundin Regina, die viele physikalische Fachsimpeleien ertragen musste und hoffentlich nicht meinetwegen Sonderpädagogik studierte.
Im direkten Zusammenhang mit dieser Arbeit möchte ich Prof. T. Hebbeker danken, der es mir ermöglicht hat diese Arbeit am III. Physikalischen Institut A zu schreiben und im Verlauf der Arbeit unterstützt hat. Besonderen Dank möchte ich Arnd Meyer aussprechen, der beim Schreiben dieser Arbeit, des Public Analysis Summary und der Analysis Note fortwährend Unterstützung geleistet hat und bis zur Veröffentlichung gegen die Widerstände mit angekämpft hat.
Für die wertvollen Ratschläge, das Korrekturlesen und das Ertragen meiner Rechtschreibung möchte ich noch einmal Arnd Meyer, Regina Jan Schulte, Sebastian Thüer und dem Erfinder des Spell-Checks danken. Ebenfalls verdienen vielen Anregungen aus der EXOTICA Gruppe Erwähnung, die diese Arbeit bereichert haben.
Nicht zuletzt möchte ich Sebastian Thüer, Jan Schulte, Tobias Pook und Fabian Schneider für die heitere und produktive Atmosphäre in unserem Büro danken, die das Arbeiten sehr Bereichert hat, auch wenn wir keine weiteren Schätze unter dem Boden ausmachen konnten.
Der Abschließende Dank gehört meinen Kollegen, die immer mit physikalischen Fragestellung, unterhaltsamen Diskussionen und viel Elan weiter geholfen haben. Namentlich möchte ich hier erwähnen: Michael Brodski, Julien Caudron, Adriana Del Piero, Deborah Duchardt, Matthias Endres, Andreas Güth, Kerstin Höpfner, Thomas Kreß, Simon Knutzen, Carsten Magass, Mark Olschewski, Paul Papacz, Holger Pieta, Stefan Schmitz, Lars Sonnenschein und Daniel Teyssier.

Auch wenn die Natur keine Unparticles gemacht hat die man hiermit finden konnte, möchte ich mit den Worten von Tomte schließen:
“Das ist nicht die Sonne die untergeht, sondern die Erde die sich dreht.”

Selbständigkeiterklärung

Hiermit erkläre ich, dass ich die vorliegende Arbeit eigenständig verfasst habe. Desweiteren habe ich Zitate kenntlich gemacht und keine anderen als die angegebenen Hilfsmittel und Quellen verwendet.